Acoustically Derived Suspended Sediment Concentrations and Flux in the Fraser River, Canada

by

Dan Haught

M.Sc., Simon Fraser University, 2010

B.Sc., Western Washington University, 2007

Thesis Submitted in Partial Fulfillment of the
Requirements for the Degree of
Doctor of Philosophy

in the
Department of Geography
Faculty of Environment

SIMON FRASER UNIVERSITY
FALL 2017

Approval

Name:	**Dan Haught**
Degree:	**Doctor of Philosophy**
Title:	**Acoustically Derived Suspended Sediment Concentrations and Flux in the Fraser River, Canada**

Examining Committee:

Chair: **Dr. Nadine Schuurman**
Professor

Dr. Jeremy Venditti
Senior Supervisor
Professor

Dr. Michael Church
Supervisor
Professor Emeritus

Dr. Scott Wright
Supervisor
Research Hydrologist, USGS

Dr. Jason Leach
Internal Examiner
Assistant Professor

Dr. Ton Hoitink
External Examiner
Professor
Department of Environmental Sciences
Wageningen University

Date Defended/Approved: October 25th, 2017

Abstract

In Canada, there is no existing systematic sediment data collection program for river systems and limited resources are available to mount manual measurement programs. Yet, there is a pressing need to understand and predict sediment fluxes because the quantity and caliber of transported sediment controls river channel stability, influences river ecology and should be considered in river management. In the Lower Fraser River, British Columbia, Canada conventional methods for estimating sediment flux are based on historical data that are no longer reliable due to the river's ongoing adjustment to land use practices, climate change, sea level variation and dredging. This research establishes methods to monitor suspended sediment delivery to the Fraser Delta using hydroacoustic signals as a surrogate of suspended sediment concentration (SSC) and grain size. Both single- and multi-frequency sediment detection approaches are evaluated. Acoustic signals from an array of three horizontally-mounted acoustic Doppler current profilers (ADCPs) are coupled with physical bottle samples within the acoustically ensonified volume. Bottle samples are analyzed for SSC and for grain size distribution. Discharge, channel-average SSC and flux are measured. Twenty-five sampling campaigns were carried-out in the Fraser River at Mission between 2012 and 2014. I develop data processing methods for acoustic signals near the ADCP *noise-floor* and establish threshold concentrations below which attenuation measured in-situ is unreliable. A single-frequency, two-stage acoustic inversion is developed for application in large rivers where the ADCPs cannot penetrate the full channel width. The method involves calibration of ADCPs and a correlation between ADCP SSC and the channel-averaged SSC. Strong calibrations for total SSC, sand SSC and silt/clay SSC are obtained. Good correlations between acoustically derived SSC and channel-average SSC allow for continuous SSC and flux estimates. Annual flux fell within the same order of magnitude as historical flux from the same location, computed with traditional methods, supporting the robustness of the method. Explicit and implicit multi-frequency inversions are explored. Comparisons between the inversion results and sample data show that the implicit method tends to perform best for estimating concentration at all flows. Realistic estimates of particle size are obtained for high flows only using this method.

Keywords: Fraser River; Sediment transport; Acoustics; Discharge; Geomorphology

Dedication

To my family and friends

Acknowledgements

I would like to thank my wife Kathleen Keating, my family, and friends for their patience throughout this endeavor.

I would like to thank my senior supervisor, Dr. Jeremy Venditti for his patience and guidance throughout this process, along with his willingness to engage in discussions that have made me a better scientist. I very much appreciate the time you have spent on this project. I have very much enjoyed and appreciate the long hours in the field, the lab, and working through the writing process.

I would also like to thank my other supervisors on my committee, Dr. Mike Church and Dr. Scott Wright for your patience, constructive critique and ideas that have improved this work greatly.

I would like to thank B-Jae Kelly and John Ng for their help in the field, with the boat, and with all the frequent tasks involved in fieldwork. It is greatly appreciated.

I would like to thank the Water Survey of Canada for their support in the field, particularly Trevor Mitchell and Curt Naumann. I would like to thank Dr. Stephanie Moore for spending some time discussing the complexities of my work with me. I would like to thank Dr. Eva Kwoll, Dr. Peter Nelson, Ryan Bradley for the great discussions, ideas, and times in the field.

I would also like to thank Nicola Rammell, Kate Donkers, Jacqui Brown, Michael Wong, Michelle Linde, and Alex Gitto for their work in the lab and field.

This project was supported by funds from the Fraser River Estuary Management Program (now defunct), Port Metro Vancouver and from the PADI Foundation.

Table of Contents

List of Tables

List of Figures

Preface

The research conducted in this thesis was lead by the author, Daniel Haught, and the work presented in Chapters 2–4 was conducted with contribution from a number of co-authors: Professor Jeremy G. Venditti, Professor Mike Church, and Dr. Scott Wright

Chapter 2 is reprinted from Water Resources Research under the reference:

Haught, D., J. G. Venditti, and S. A. Wright (2017), Calculation of in situ acoustic sediment attenuation using off-the-shelf horizontal ADCPs in low concentration settings, Water Resour. Res., 53, doi:10.1002/2016WR019695.

Chapter 3 is to be submitted to Water Resources Research under the title *Acoustically derived annual sediment fluxes in a large alluvial river* with the following author list: D. Haught, J.G. Venditti, and M. Church.

Chapter 4 is to be submitted to Water Resources Research as a manuscript titled *Application of multi-frequency acoustic inversions using "off the shelf" ADCPs* with the following author list: D. Haught, J.G. Venditti, and S.A.. Wright.

Chapter 1. Introduction

The Fraser River has always been essential to the health and wealth of British Columbia and Vancouver. Like sand-bedded rivers around the world that drain large basins seaward, it has shaped and enabled intense urban development on its floodplain and delta. Riverine (i.e. floods) to basin and regional scale (i.e. climatic) change can impact the socioeconomic and ecologic health, which are interconnected by floodplains and deltas. To monitor and manage morphological changes associated with large rivers, prediction of sediment transport along with the processes associated with the phenomena is critical.

In Canada, there is no existing systematic sediment data collection program for river systems, and limited resources are available to mount manual measurement programs. Yet the demand for such data is strong. In the Fraser River, BC, sediment data and budgets are necessary for both navigable water maintenance and for the ecological management of the river, estuary and delta. Research on the morphology of the Fraser River and delta also relies on sediment flux data.

Historically, managers and scientists relied on sediment rating curves for approximating the suspended sediment flux. However, sediment rating curves may no longer be accurate due to rating curve drift and instability [*Church*, 2007]. This uncertainty, along with morphological research needs, has generated a recent demand for re-establishing suspended sediment measurements on the Fraser [*NHC*, 1999, 2002; *Church* 2007, 2010]. This demand has motivated investigation of suspended sediment surrogates to reduce the resources needed for sediment sampling campaigns while still producing high spatiotemporal suspended sediment data [*Church and Venditti*, 2008]. Surrogate sediment measurement technologies have been developed, the most encouraging of which has been hydroacoustics. This work is an investigation into the practicality of an acoustically-derived sediment surrogate, which can be deployed nationally to meet the need for sediment data. Nevertheless, the method remains experimental and needs to be evaluated in a wide variety of river systems and through long time periods (years) before it is universally adopted as a suitable sediment surrogate.

Over the past two decades, hydroacoustic instruments (Acoustic Doppler Current Profilers, hereafter 'ADCP') have been developed for continuous monitoring of velocity in rivers and index-based discharge monitoring [*Levesque and Oberg*, 2012]. The widespread deployment of horizontally-oriented ADCPs opens the possibility to use these 'off the shelf' acoustic instruments to measure suspended sediment concentrations (as they project sound across the channel) using properties of the acoustic intensity backscattered from particulate matter in the water column. However, critical evaluations of the ADCP technology and tests of acoustic theory for long-term continuous monitoring of suspended sediment fluxes have just recently begun to emerge [c.f. *Moore et al*., 2013, *Topping and Wright*, 2016; *Venditti et al*., 2016]. Therefore, the evaluation of the theory and the capabilities of 'off the shelf' ADCPs are timely.

1.1. Introduction to acoustic inversion theory

Application of hydroacoustics to sediment monitoring relies on the fact that sound emitted through the water column 'bounces' back from suspended particles producing a response termed "backscatterence". Commercial and research acoustic instruments provide non-intrusive profiling that can provide backscatter data at distances that range from millimeters to hundreds of meters collected at timescales as low as fractions of a second, providing spatiotemporal field data that is unprecedented in sediment transport research.

Previous work has developed many methods for inverting acoustic backscatter to concentration or particle size, along with models that describe sound wave interaction with sediment. The term "acoustic inversion" is used to describe back-calculation of sediment properties (suspended sediment concentration (SSC) or particle size) from acoustic signals using the sonar equation, described generally by *Urick* [1975]. These models assume sediment characteristics are known *a priori*. When sound travels through a fluid medium and interacts with suspended sediment, two principal responses occur; attenuation and backscattering of active sound. *Flammer* [1962] has shown that attenuation of sound from sediment can be attributed to three loss mechanisms: scattering by the particles (ζ_{scatt}), energy loss due to viscous shear (ζ_{visc}), and heat loss due to conduction (Figure 1.1). Heat loss is significantly less in magnitude than scattering and viscous loss and is generally neglected. The sediment scattering loss is

due to the re-radiation of the sound wave by the particle [*Flammer* 1962] causing the pattern and intensity of the returning wave to diminish. The scattering of a sound wave is a function of the ratio of the acoustic wavelength, λ (λ=c/F), to $2\pi a_{50}$, where c is the speed of sound in water, F is the acoustic frequency and a_{50} is the median particle radius. When $\lambda >> 2\pi a_{50}$ the scattering intensity is directed back towards the origin and is denoted as the backscattering-loss or Rayleigh region (Figure 1.1). When $\lambda << 2\pi a_{50}$, known as the diffraction loss region, half of the scattered wave is directed in the forward direction while the other half is scattered in all directions, causing sound energy loss by interference or non-return. When $\lambda \sim 2\pi a_{50}$, sound energy loss becomes more complicated due to the sensitivity to acoustic frequency [*Flammer*, 1962]; this region is denoted as the transition region (Figure 1.1).

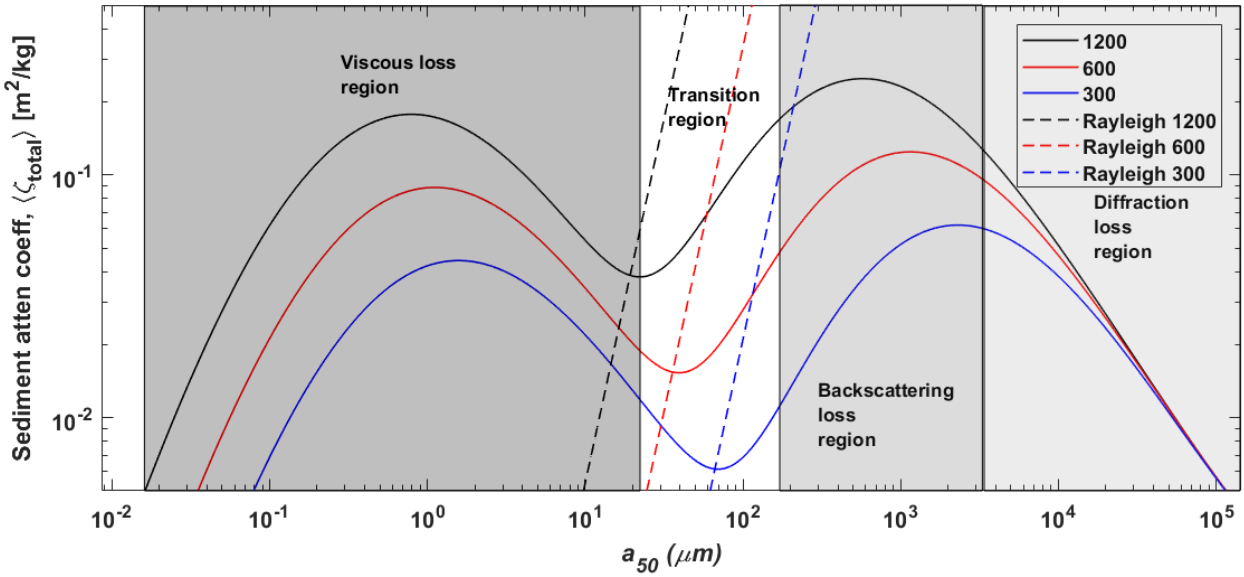

Figure 1.1 Attenuation loss ($\zeta_{total} = \zeta_{scatt} + \zeta_{visc}$) regions for three acoustic frequencies plotted as a function of the median particle radius (a_{50}). The sediment attenuation coefficient is averaged over a lognormal grain size distribution with a normalized standard deviation of 1 [c.f. *Moore et. al.*, 2013].

The attenuation of sound due to viscosity is caused by the shear associated with lag between the displacement of the particle and the sound wave [*Flammer*, 1962] and is denoted the viscous region (Figure 1.1). The magnitude of loss is dependent on the magnitude of the lag and the surface area of the particle. As the particle size increases so does the lag between the fluid and the particle, caused by the inertia of the particle. Additionally, as the particle size increases for any given volume of particles at constant

concentration, the total surface area decreases, creating a complex viscous loss due to opposing relationships with surface area and lag [*Flammer*, 1962].

Acoustic signal interaction with silt/clay sediment responds differently than sand, leading the former to attenuate more while the latter shows greater backscatterence. Theory has been developed to approximate the interaction of backscattering form function characteristics of the sediments [*Hay*, 1991; *Crawford and Hay*, 1993; *Thorne and Meral*, 2008]. Backscattering form function models can also be described by Rayleigh and geometric scattering models, yet lab measurements have shown that sediment characteristics—with respect to rigid spheres-- influence how well models can describe acoustic signal-sediment interactions [*Thorne and Hanes*, 2002]. With that said, backscattering and attenuation models of acoustic response have allowed for the application of acoustic inversions in fluvial environments when sediment characteristics are well resolved.

The most common acoustic inversion methods are empirical [*Gartner*, 2004; *Hoitink and Hoekstra*, 2005; *Venditti et al.*, 2016], semi-empirical [*Topping and Wright*, 2016], and multifrequency [*Hay*, 1991; *Thorne and Hanes*, 2002; *Thorne and Hurther*, 2016]. The empirical method correlates backscatter to measured SSC samples collocated spatiotemporally, while the semi-empirical does the same, but takes into account theoretical responses to sand and silt/clay fractions. The multifrequency method relies on the concept that if more than one acoustic frequency ensonifies the same volume, then the variance between multiple acoustic responses can be minimized to determine concentration and grain size distribution (GSD) characteristics, with the number of resolvable sediment characteristics depending on the number of frequencies applied.

1.2. Acoustic theory

The linear version of the sonar equation has the following form:

$$P_{rms} = \overbrace{P_o r_o \beta \left\{\frac{3\tau c}{16}\right\}^{1/2} \frac{0.96}{k a_t}}^{k_t} \overbrace{\left[\frac{\langle f \rangle}{\sqrt{\langle a \rangle \rho_s}}\right]}^{k_s} \left[\frac{M^{1/2}}{r\psi}\right] e^{2r(\alpha_n)} \tag{1.1}$$

where P_{rms} is the root-mean-square pressure and is derived from acoustic intensity received by the transducer (see Appendix 4.1 of Chapter 4), P_o is the reference pressure at range r_o, r is distance from transducer, a is particle radius, a_t is transducer radius, πc is pulse length (c is speed of sound and τ is the acoustic transmit time), ρ_s is particle density, k is wave number, M is mass concentration, f is the backscatter form function that describes the scattering properties of the GSD (see Appendix 4.2 of Chapter 4 for further information), $\beta=T_vR$ where T_v is the voltage transfer function of the transducer and R is the transducer receive sensitivity, ψ accounts for departure from spherical spreading in the near-field, and α_n is attenuation [*Thorne and Hanes,* 2002] and is due to the fluid and sediment within the ensonified volume (the sediment attenuation coefficient is defined in Appendix 4.3 of Chapter 4). The n subscript denotes attenuation in nepers/m, while the angle brackets represent an average over the GSD. To simplify Equation 1.1, k_s is defined as a combination of the backscattering parameter and characteristics of the GSD (see definition in Appendix 4.2 of Chapter 4). The variable k_t is combined into instrument constants or variables that vary solely with the celerity of sound (further defined in Appendix 4.4 of Chapter 4).

1.3. Single and multifrequency inversions

When using ADCPs, single frequency inversions [*Hointink and Hoekstra,* 2005; *Sassi et al.,* 2012*; Venditti et al.,* 2016; *Topping and Wright,* 2016] commonly use the sonar equation rewritten in logarithmic form as:

$$RL = SL - (SP + AT) + 10log_{10}(M) + \overbrace{10log_{10}\left\{\frac{\langle f\rangle^2}{\langle a\rangle}\frac{3\tau c}{16}\left[\frac{0.96}{ka_t}\right]^2\right\}}^{TS} \tag{1.2}$$

where RL is reverberation level, SL is source level, SP is the spreading loss, AT is the attenuation loss and the last term TS is the target strength. In logarithmic form the units are decibels. Combining SL and TS into a system variable K_t, which varies with particle size and celerity of sound, the sonar equation is:

$$log_{10}(M) = 0.1(RL + 2TL) - 0.1K_t \tag{1.3}$$

where 2*TL* is the two-way transmission loss (*SP* + *AT*) [*Wright et al.,* 2010]. The theoretical value of 0.1 derives from the definition of the decibel. The term (*RL* + 2*TL*) is the measured backscatter corrected for transmission losses along the beam path by fluid and sediment attenuation. Equation 1.3 can be used to invert backscatter to compute concentration, but only if particle size is specified. Since particle size is often not known, and variable, Equation 1.3 has been typically applied empirically through regressions between log10(*M*) and (RL+2*TL*); using this approach, the slope and intercept provide the necessary parameters for the inversion (slope is typically allowed to vary from its theoretical value of 0.1). The primary limitation of this approach is that it implicitly assumes that particle size is constant along the range over which the regression is calculated, which limits its accuracy [*Topping and Wright*, 2016].

An alternative to the single frequency semi-empirical approach is to use multi-frequency methods (defined as two or more frequencies) to estimate mass concentration, mean particle size, [*Hay,* 1983, 1991; *Thorne et al.,* 1991; *Thorne at al.,* 1993; *Thorne and Hanes,* 2002; *Thosteson and Hanes,* 1998] and, using at least three frequencies, the standard deviation of the GSD. In multifrequency approaches, mass concentration, *M*, is calculated by inverting Equation 1.1 for an individual frequency [*Hay*, 1991], by:

$$M = \frac{P_{rms}^2 r^2 \psi^2}{k_t^2 k_s^2} e^{4r(\alpha_f + \alpha_s)} \tag{1.4}$$

where α_f and α_s are attenuation of sound from fluid and particulates in suspension, respectively. Sediment attenuation is defined as:

$$\alpha_s = \langle \zeta_{total} \rangle M = M\langle \zeta_{visc} \rangle + M\langle \zeta_{scatt} \rangle \tag{1.5}$$

where ζ_{scatt} and ζ_{visc} are the sediment scattering and viscous attenuation coefficients.

Equation 1.4 is an implicit equation because *M* is on both sides of the equation and cannot be separated from the computation of sediment attenuation (Eq. 1.4 and 1.5). In multifrequency implicit inversions, concentration is determined by minimizing the variation among all frequencies. This method requires large computation times due to iterations needing to occur at each time-step for each location along the acoustic beam.

In addition to the large computational time, the implicit inversion has limitations in its applicability as it tends to propagate error from uncertainties in inversion parameters cumulatively by integration over the acoustic beam range. The uncertainties tend to occur in conditions when M> 1kg/m^3, frequencies are >2MHz, and when a>100μm [*Hurther et al.,* 2011].

To work around the intense computational time of the implicit method, *Lee and Hanes* [1995] modified Equation 1.4 into an explicit form. The explicit method utilizes the natural logarithm of Equation 1.4:

$$\ln(M) = 2\ln(P_{rms}T_v R\psi) + 4\alpha_f r - 2\ln(k_s k_t) + 2\ln(r) + 4\int_0^r \langle\zeta_{total}\rangle M dr. \quad (1.6)$$

This equation can be applied to acoustic systems that do not apply a time-varied gain, and therefore if k_t does not change with range, its derivative with respect to range is zero. Differentiation of Equation 1.6 leads to a Bernoulli-type, nonlinear, differential equation, which allows -- through substitution and integration -- the removal of concentration from the right-hand-side of Equation 1.6 [*Lee and Hanes,* 1995; *Thorne and Hanes,* 2002]. The explicit method has the advantage of substantially quicker computation time when compared to the implicit inversion, but has the same limitation as the implicit inversion in that error propagates with distance from the transducer [*Thorne et al.,* 2011]. To determine particle size, the explicit method can be used in both the coupled and decoupled fashion, similar to the implicit method. *Thosteson and Hanes* [1998] describe a multi-frequency approach that uses the coupled explicit method to minimize M amongst frequencies in Equation 1.6 to determine both particle size and concentration (simultaneously) as a function of distance from the transducer.

1.4. Particle size determination

There are two different methods to determine mean particle radius in suspension, which I term ‘coupled’ and ‘decoupled’. The coupled method uses iterations that determine concentration and particle size simultaneously [*Thorne et al.,* 2007; *Thorne and Hurther,* 2014], while the decoupled method first determines particle size, then computes concentration using the given particle size [*Hay and Sheng,* 1992; *Crawford and Hay,* 1993].

The decoupled implicit method was originally developed by *Hay* and Sheng [1992] and *Crawford and Hay* [1993] and solves Equation 1.4 for a range of particle-sizes for each acoustic frequency. The most common acoustic method to determine particle size using the decoupled implicit method is to minimize the acoustic response (essentially concentration) to the backscattering form function either as the difference [*Crawford and Hay*, 1993] or ratio [*Hay and Sheng*, 1992] between different frequencies, then minimizing amongst all frequencies. For example, the decoupled difference method presented by *Crawford and Hay* [1993] attempts to minimize the following parameter:

$$\epsilon_{i,j} = \left(\frac{P_{rms,i}\psi_i}{k_{t,i}\langle f_i\rangle}\right)^2 - \left(\frac{P_{rms,j}\psi_j}{k_{t,j}\langle f_j\rangle}\right)^2 \tag{1.7}$$

where *i* and *j* represent two different frequencies and $\langle f\rangle^2 = k_s^2\langle a\rangle$. The particle size that minimizes $\epsilon_{i,j}$ is chosen and used to compute concentration. At frequencies common to ADCPs (300-2000 kHz) there are limitations to the effectiveness of methods that use the form function only ($\langle f\rangle$ in Eq. 1.7). In conditions when $ka \ll 1$ (i.e. silt/clay) the minimization does not converge as there is no variation among multiple frequencies, leaving the method suitable only for sand sizes particles [*Thorne and Hanes,* 2002].

The coupled implicit method was described by *Thorne et al*. [2007] and solves Equation 1.4 by minimizing concentration between multiple frequencies to find both concentration and particle size simultaneously. This is done by computing *M* for each frequency for a range of predetermined particle sizes and computing α_s and k_s theoretically. *Thorne et al.* [2011] and *Wilson and Hay* [2015] have applied the coupled implicit method to acoustic inversions. However, their application does not include viscous attenuation, the addition of which would make it appropriate for all conditions as it includes all factors that cause attenuation loss and scattering for all grain sizes. In conditions where the GSD is dominated by clay and silt, an acoustic response is outside the scattering loss region [*Flammer*, 1962] and is more sensitive to viscous loses, which limits Equation 1.7 because it only relies on the form function. To address this limitation*, Moore et al.* [2013] present a decoupled method, adapted from *Crawford and Hay* [1993], that utilized sediment attenuation instead of the form function. This adaptation works in conditions dominated by clay and silt material, which is sensitive to viscous attenuation particularly, and circumvents the limitation of coarse material when using

Equation 1.7. *Moore et al.* [2013] find the particle size by minimizing, $\varepsilon_{i,j}$, amongst frequencies:

$$\varepsilon_{i,j} = \frac{\alpha_{s,in-situ,i}}{\langle \zeta_{total,i} \rangle} - \frac{\alpha_{s,in-situ,j}}{\langle \zeta_{total,j} \rangle} \tag{1.8}$$

The fundamental difference between this minimization and the *Crawford and Hay* [1993] minimization (Eq. 1.7) is that here, attenuation is used in the calculation instead of the form function (which relates to backscatter). To compute concentration, *Moore et al.* [2013] rely on the relation between attenuation (Np/m) and mass concentration (kg/m^3) in Equation 1.5, which can be rewritten as:

$$M = \frac{\alpha_{s,in-situ}}{\langle \zeta_{total} \rangle} \tag{1.9}$$

Moore et al. [2013] use in-situ attenuation in Equation 1.5. In-situ attenuation is computed by the linear regression between acoustic backscatter that accounts for all parameters except sediment attenuation and distance from the transducer [*Topping et al.,* 2007; *Moate and Thorne,* 2009; *Wright et al.,* 2010]. The slope of the regression is assumed equal to total attenuation. The *Moore et al.* [2013] method relies on the assumption that concentration and particle size do not change significantly with distance from the transducer. When in-situ attenuation can be accurately determined, the ratio of in-situ attenuation and the sediment attenuation coefficient can be used to compute a time-series of SSC. *Moore et al.* [2013] make the assumption that the attenuation coefficient $\langle \zeta_{total} \rangle$ does not change with time, which holds when applying their method to events that occurred over a span of weeks. If the attenuation coefficient cannot be computed, it may be reliably estimated with knowledge of the in-situ GSD. Unfortunately, when applying the *Moore et al.,* [2013] method beyond the event scale, in environments where the GSD changes, their assumption likely does not hold.

Topping and Wright [2016] present a dual frequency approach for computing silt and clay concentration, sand concentration, and sand median grain size, and apply the method to several rivers in the southwest United States. Two fundamental assumptions are invoked: 1) silt and clay dominates attenuation and 2) sand dominates backscatter. Similar to *Moore et al.* [2013], their method uses linear regression to estimate the in-situ attenuation coefficient, which is in turn calibrated to silt and clay concentration. For sand

concentration and median particle size, a “base” calibration is developed for each frequency for a narrow range of particle sizes (e.g. the median particle size as measured at a given site). To compute sand concentration and particle size for a given measured backscatter, the theoretical target strength for a given size and base calibrations are used iteratively to determine the particle size that minimizes the difference in sand concentration between the two frequencies. In addition, methods are presented for making corrections for conditions when silt and clay contribute to backscatter, which can have a significant effect on the results. The method is particularly suited to sand-bedded rivers where silt and clay transport (washload) is somewhat decoupled from sand transport. Additionally, their method requires a reliable estimate of in-situ attenuation, which again, limits the application to high concentration conditions (10^2-10^4 mg/L).

1.5. Influence of GSD on acoustic inversions

Acoustic inversions using Equation 1.1 have been widely used in investigations of sediment transport in nearshore environments where a GSD is assumed to have a constant standard deviation (σ_g), but the mean particle diameter is varied. This is a useful simplification in the near-shore environment where GSDs are unimodal, log-linear and locally sourced [*Hay and Sheng,* 1992; *Thorne et al.,* 2007]. This approach has also been widely used in small scale (meters) laboratory experiments designed to examine the acoustic response to varying particle size (*Sheng and Hay,* 1988; *Thorne and Campbell,* 1992; *Thosteson and Hanes*, 1998; *Moate and Thorne,* 2009]. In environments where the GSD changes in breadth, acoustic inversions are subject to increased error. For example, *Moate and Thorne* [2009] showed that varying the GSD shape and breadth can result in error in both the estimated mean grain size and/or the mass concentration.

Acoustic inversion techniques have been used in estuarine environments [*Thorne et al.,* 1994; *Thorne and Hardcastle,* 1997] where GSDs may be more dynamic due to differing sources of washload, rapid settling and resuspension, or flocculation. This has led to laboratory studies of the acoustic response to suspensions with different particle shapes [*Thorne et al.,* 1995a; *Richards et al.,* 2003; *Thorne and Buckingham*, 2004], mixed mineralogy [*Schaafsma and Hay*, 1997; *Moate and Thorne*, 2011, 2013], broad GSDs (*Moate and Thorne,* 2009), and flocculated aggregates [*MacDonald et al.,* 2013; *Thorne et al.,* 2014]. These studies have shown that acoustic signals, either

through backscattering or attenuation, are significantly influenced by the median size of the particle, concentration or number of particles in suspension, shape of the particles in suspension, and the width and mineralogy of the GSD.

In fluvial environments, the suspended particle size ranges from fine clays and silts to sand. Distributions are normal to lognormal and can be unimodal and multimodal. The large variance in size and distribution needs to be accounted for in the acoustic theory because of the strong influence that GSD characteristics have on acoustic backscatterence and attenuation. Furthermore, the effect that GSD variability has on acoustic inversions-- whether single- or multi-frequency-- needs to be examined.

1.6. Thesis scope and objectives

The successful application of acoustic inversion methods in nearshore and estuarine environments with custom built transducers has led to interest in using similar methods with ADCPs in riverine environments. This application is somewhat more difficult because ADCPs, in contrast to custom-built transducers, have a greater spatial range, larger sampling volumes and require the estimation of various instrument constants for the acoustic inversion. Custom built transducers do not suffer from the latter problem, because instrument constants can be easily measured in laboratory settings or are known from instrument design. When utilizing ADCP profiles that have a range scale of 10’s to 100’s of meters, the ensonified volume can be on the order of cubic meters.

In this respect, there are two important scale considerations when using ADCPs to monitor sediments in rivers. The first is how well acoustic inversion methods expand to larger, more practical scales used in riverine applications. Larger ensonified volumes inherently have more sedimentological variability due to the nature of suspended sediment in turbulent fluid. Given the generally conical shape of the ensonified volume, with increased distance from the transducer the ensonified volume will go from being relatively small and further from the surface or bed, to being larger and encompassing more of the water column. This change will create variability in the GSD’s within the respective cells as a function of distance from the transducer. The second scale consideration is how acoustic calibrations change over time (intra- and inter-annual scales) -- that is the temporal scale of variability in the river. At our field site in the

Fraser River, British Columbia, sediment sources vary through the year and the timing of delivery of that sediment supply conditions acoustic response to sediment in the river. This intra- or inter-annual variability is reflected in the acoustic response to concentrations, GSD and sediment composition (mineralogy). When acoustic inversions do not account for variability in the GSD or minerology, it is necessary to critically examine how calibrations respond to sedimentological change. In contrast, when inversion methods do account for GSD characteristics, it is also necessary to evaluate how well they accomplish this.

To date, limited research has examined the use of hydroacoustics in a riverine environment, particularly at low concentrations (< 500 mg/L). Though literature has suggested that acoustic surrogates should work in a wide range of conditions [*Topping et al.*, 2007], few investigations have examined how various inversion methods work at low concentration. There may exist thresholds where different methods work better than others. The importance of these thresholds lies within the context of sediment monitoring programs, where a wide range of conditions may occur, and semi-autonomous methods that accurately handle SSC variability are necessary. To further develop and evaluate the use of acoustic inversions in sediment transport monitoring and research, an extensive evaluation of the influence that GSD variability has on acoustic inversions is necessary. Furthermore, there has been limited investigation into the application of multi-frequency approaches to monitoring both suspended sediment concentration and particle size distribution at the spatial scales required for large rivers, using “off-the-shelf” ADCP instruments. Lastly, inherent in the multifrequency method is the use of known variables and instrument constants critical to inversion methods. Though most of these values are available for “off-the-shelf” ADCPs, some are not and practical methods are needed to estimate unknown constants.

Therefore, to broaden the application of “off-the-shelf” ADCPs for use in SSC monitoring programs, I undertook a three-year sediment monitoring program in the Fraser River, British Columbia, Canada, where I deployed three collocated horizontal looking ADCPs with different frequencies (300 kHz, 600 kHz and 1200 kHz). I also undertook 25 bottle sampling campaigns over that period where I measured concentration in the acoustic beam and suspended sediment flux in the channel, which was much wider than the range of the ADCPs. The overall objectives of the work were to:

1. Develop a method for calculation of in-situ sediment attenuation, using “off-the-shelf” ADCPs with different frequencies, that is applicable to a low concentration setting where signals fall below the acoustic noise floor.

2. Test semi-empirical methods for calculating sediment concentration using a two-stage method that involves calibration of ADCPs to size fractionated sediment and development of an ADCP sediment-index correlation to the channel averaged sediment flux. This expands and further develops the purely empirical methods proposed by *Venditti et al.* [2016].

3. Apply the multifrequency inversion theory, developed for use with custom-built acoustic sensors, to estimate sediment concentration and GSD characteristics using “off-the-shelf” ADCPs.

There are two overarching goals of the work. The first is to explore how grain size variability affects the calculation of in situ attenuation, semi-empirical single frequency inversions and multi-frequency inversions. The second goal is to evaluate the suitability of these methods for application to a long-term sediment monitoring program.

Chapter 2. Calculation of in-situ acoustic sediment attenuation using off-the-shelf horizontal ADCPs in low concentration settings

Abstract

The use of ‘off-the-shelf’ acoustic Doppler velocity profilers (ADCPs) to estimate suspended sediment concentration and grain size in rivers requires robust methods to estimate sound attenuation by suspended sediment. Theoretical estimates of sediment attenuation require *a priori* knowledge of the concentration and grain size distribution (GSD), making the method impractical to apply in routine monitoring programs. In-situ methods use acoustic backscatter profile slope to estimate sediment attenuation, and are a more attractive option. However, the performance of in-situ sediment attenuation methods has not been extensively compared to theoretical methods. I used three collocated horizontally mounted ADCPs in the Fraser River at Mission, British Columbia and 298 observations of concentration and GSD along the acoustic beams to calculate theoretical and in-situ sediment attenuation. Conversion of acoustic intensity from counts to decibels is influenced by the instrument noise floor, which affects the backscatter profile shape and therefore in-situ attenuation. I develop a method that converts counts to decibels to maximize profile length, which is useful in rivers where cross-channel acoustic profile penetration is a fraction of total channel width. Nevertheless, the agreement between theoretical and in-situ attenuation is poor at low concentrations because cross-stream gradients in concentration, sediment size or GSD can develop, which affect the backscatter profiles. I establish threshold concentrations below which in-situ attenuation is unreliable in Fraser River. Our results call for careful examination of cross-stream changes in suspended sediment characteristics and acoustic profiles across a range of flows before in-situ attenuation methods are applied in river monitoring programs.

2.1. Introduction

Traditionally, sediment flux in rivers has been estimated and computed annually through sediment-discharge rating curves that allow calculation of a sedigraph based on a hydrograph. The sediment rating curve relation has been shown to incur significant error due to poor relations between concentration and discharge [*Walling*, 1977]. Over the last three decades the use of hydroacoustics to measure sediment concentration, and more recently particle size, has increased. In rivers, the use of hydroacoustics has been facilitated by the availability of off-the-shelf acoustic Doppler current profilers, which provide high spatial and temporal resolution data, are resistant to biofouling, and provide estimates of flow velocity. The coupling of velocity with concentration allows for an estimate of sediment flux.

Use of hydroacoustics to calculate sediment concentration and particle size is based on the sonar equation, which models the response of a unique acoustic frequency to suspended particulates in an ensonified volume in the water column [*Urick*, 1975; *Hay*, 1991]. This is accomplished by finding the relation between acoustic signal metrics (e.g. fluid attenuation corrected backscatter, sediment attenuation corrected backscatter, sediment attenuation) and metrics of the suspended sediment concentration and grain size distribution (GSD), typically the median or fraction in a particular grain size range [*Gartner*, 2004; *Hoitink and Hoekstra*, 2005; *Wright et. al.*, 2010; *Venditti*, *et. al.* 2016; *Topping and Wright*, 2016]. Acoustic backscatter is the sound energy reflected back towards an acoustic transducer in an ensonified volume. Fluid 'corrected' backscatter [*FCB*] means that an acoustic backscatter profile has been adjusted to account for fluid attenuation and sediment 'corrected' backscatter [*SCB*] means that a *FCB* profile has been adjusted to account for sediment attenuation.

Use of hydroacoustic instruments to measure suspended sediment is based on a theoretical relation between suspended sediment concentration, particle size, and measured acoustic backscatter. The sonar equation, simplified by *Urick* [1975], is:

$$RL + NL = SL - 2TL + TS \tag{2.1}$$

where *RL+NL* is the sum of the reverberation level (*RL*) and the noise level (*NL)* read by the instrument which is analogous to acoustic intensity, 2*TL* is the two-way transmission

loss caused by acoustic spreading and fluid, viscous, and scattering attenuation, *SL* is the source level, and *TS* is the target strength. Target strength is a function of the ratio of acoustic wavelength to particle diameter, GSD shape within the ensonified volume, and concentration. Included in TS are temperature and pressure dependent variables that affect celerity of sound in water and therefore vary a little over the year. Electronic noise contributes to NL (c.f. *Urick*, 1975; *Clay and Medwin*, 1977), however there is also ambient environmental noise contributing to NL that is related to what is in suspension [*Libicki et al.*, 1989]. The equation is expressed in decibels with the reference pressure (1 μPa) set at a range of 1 m from the transducers.

More typically, the linear form of the sonar equation is inverted to calculate mass concentration and grain size either explicitly [*Lee and Hanes*, 1995; *Thosteson and Hanes*, 1998; *Thorne and Hanes*, 2002; Hanes, 2012] or implicitly [c.f. *Hay*, 1991; *Hay and Sheng*, 1992; *Crawford and Hay*, 1993; *Thorne et. al.*, 1993; *Thorne and Hardcastle*, 1997; *Thorne and Hanes*, 2002; *Thorne and Buckingham*, 2004; *Moate and Thorne*, 2009, 2013; *Thorne and Hurther*, 2014]. In the explicit solution, the mass concentration is separated as a variable and solved for directly. In the implicit solution, the mass concentration is also a product of attenuation and is solved for iteratively. Empirical or semi-empirical methods [c.f. *Woods and Teasdale*, 2013; *Venditti et al.*, 2016], can be shown to be equivalent to the acoustic inversion when relating the sonar equation to measurements in a homogenous ensonified volume [*Thorne and Buckingham*, 2004].

Both methods require reliable estimates of sediment attenuation to account for losses that occur when the sound moves to and from the transducer. Although at low concentrations, (tens of mg/L) where sediment attenuation << fluid attenuation, accounting for sediment attenuation is necessary only for certain combinations of grain size and acoustic frequency [*Thorne et al.*, 1991]. As concentrations increase, attenuation generally increases and it is necessary to correct acoustic backscatter to account for sediment attenuation, especially when relating the attenuation corrected backscatter to sand concentrations [e.g. *Topping and Wright*, 2016].

Accounting for attenuation is done in the calculation of transmission losses as:

$$2TL = 20log_{10}(r) + 2\alpha_f r + 2\alpha_s r \quad (2.2)$$

where *r* is the range from the ADCP for each beam for each frequency and α_f and α_s are the fluid and sediment attenuation, respectively. The first term on the right-hand side of Equation 2.2 is due to spherical spreading in the far-field [*Teledyne RDI Instruments*, 2011], the second term accounts for fluid attenuation and the third term accounts for sediment attenuation (viscous and scattering). Attenuation due to water is a function of temperature and frequency (assuming salinity and pressure are negligible in shallow rivers). Here I use the *Francois and Garrison* [1982] water attenuation model because it is well defined for a broad frequency range (100 Hz to 1 MHz).

The standard way to measure acoustic attenuation is to place a source and a receiver at a known distance and measure attenuation through a medium [*Hay*, 1991]. This can be done with sediment suspended in water. In a sediment monitoring program, this method would require additional instrumentation (i.e. a hydrophone) and a more intricate instrument setup at an ideal field site. Fortunately, there are two other ways to estimate attenuation by sediment for ADCPs: theoretically and in-situ. Sediment attenuation is the sum of the viscous and scattering components of attenuation losses integrated over the GSD. Therefore, the theoretical method requires knowing the sediment concentration, composition and GSD *a priori*, which allows for estimation of attenuation from semi-empirical models [*Hay*, 1991; *Thorne and Hanes*, 2002; *Thorne and Meral*, 2008; *Thorne and Hurther*, 2014]. In routine suspended sediment flux monitoring programs in rivers, application of the theoretical method is challenging because GSDs and, often, sediment composition change through hydrographs at time scales ranging from synoptic scale floods to annual flow cycles affected by sediment supply. Furthermore, the relation between flow, concentration and GSD is known to be hysteretic in many rivers [e.g. *McLean et. al.*, 1999; *Landers and Sturm, 2013; Attard et. al.*, 2014; *Venditti et. al.*, 2016]. The information requirements for the theoretical attenuation method requires direct and continuous measurement of GSDs, which largely negates the benefits of using hydroacoustics as a suspended sediment surrogate [*Venditti et. al.*, 2016]. This does not prohibit the application of the theoretical method, but assumptions must be made about how GSDs respond to flood flows to successfully apply it.

The in-situ method of estimating sediment attenuation uses the slope of the linear relation between logarithm of backscatter (after correcting for losses due to the fluid and spreading) and distance (range) from the ADCP. The attenuation can then be

attributed to the particulates suspended in the ensonified volume [*Thorne and Buckingham*, 2004; *Topping et. al.*, 2007, 2015; *Wright et. al.*, 2010]. In-situ sediment attenuation has been shown to relate strongly to clay and silt suspended sediment [*Wright et. al.*, 2010; *Moore et. al.*, 2013; *Topping and Wright*, 2016], whereas coarser, sand-sized suspended sediment tends to relate to acoustic backscatter since attenuation from coarser material is substantially less than backscatter from coarser material [*Hanes*, 2012]. This concept allows for two independent relations that can estimate fine and coarse load [*Wright*, *et. al.* 2010, *Topping and Wright*, 2016]. However, *Hanes* [2012] places an important constraint on this separation; when the ratio of clay/silt (fines) and coarse concentrations is in unity or fine concentrations are greater than sand concentrations, backscatterence from sand will not dominate the signal and the separation may not be possible.

In-situ estimates of attenuation should be more reliable than theoretical methods because the calculation is responsive to all types of particulates and artifacts in the ensonified volume (sediment, organics, bubbles, etc.). When acoustic signals respond differently to concentrations within different grain size ranges, as is the case when backscatter relates to sand concentrations and attenuation relates to fine concentrations, it should be possible to recognize size dependent hysteretic behavior. For example, *Moore et. al.* [2013] used a hybrid semi-empirical and explicit inversion method to estimate in-situ attenuation, concentration, and particle size, which can be used to produce a time-series of the approximated GSD.

Unfortunately, application of the in-situ method is complicated by the presence of the ADCP noise level or what is commonly called the ‘noise floor’ in reference to ADCPs. When the noise floor is reached, methods to truncate [*Woods and Teasdale*, 2013; *Topping and Wright*, 2016] or extend [*Gostiaux and van Haren*, 2010; *Moore et. al.*, 2012] acoustic profiles have been used, yet difficulties arise when evaluating the effect of these methods. At lower concentrations, fluid corrected backscatter profiles tend to be non-linear [*Gostiaux and van Haren*, 2010] and truncation at shorter range can lead to increased slopes and higher than expected in-situ attenuation. This artifact occurs as the signal approaches a signal to noise ratio of one. Additionally, the noise floor can vary during annual hydrographs due to changes in concentration and GSD, complicating the use of a constant truncation point. Further complicating these methods of dealing with

the noise floor is that there are typically no observations of cross channel changes in sediment properties to explain acoustic profile variability.

In this paper, I compare theoretical and in-situ methods for estimating acoustic attenuation. In-situ attenuation is derived from an array of three side-looking (horizontal) acoustic Doppler current profilers deployed in the Fraser River, British Columbia. Theoretical attenuation is derived from bottle samples obtained within the sampling volume of the ADCPs. I use several large-volume suspended sediment samples in which the GSD is well constrained to independently evaluate the in-situ method, then compare the theoretical attenuation from bottle samples to the in-situ method. Our specific research questions are: 1) What is the best practice for obtaining reliable logarithm of acoustic backscatter profiles where the backscatter is near the acoustic noise floor? 2) How does in-situ attenuation compare with theoretical attenuation calculated from bottle samples? 3) How well does the in-situ attenuation method perform in a system with low concentrations?

2.2. Theory

2.2.1. Acoustic backscatter for off the shelf ADCPs

Commercially available ADCPs report a measure of backscatter as the echo intensity (*EI*), in counts (per bin, per beam), which is converted to backscatter in decibels using one of two approaches depending on how close the profile is to the noise floor (NL). When the acoustic profile is beyond 10 times the noise floor [*Gostiaux and van Haren*, 2010], the equation to convert from counts to decibels is:

$$I_{db} = k_c(EI - NL) \tag{2.4A}$$

When the acoustic profile approaches the noise floor (signal/noise < 10), *Gostiaux and van Haren* [2010] utilize:

$$I_{db} = 10log_{10}(10^{\frac{k_c EI}{10}} - 10^{\frac{k_c NL}{10}}) \tag{2.4B}$$

where *NL* is the noise level in counts. The variable k_c is a temperature dependent instrument constant that serves as a scale factor between echo intensity measured in relative units (counts) to acoustic intensity in decibels. It is not possible to compare *EI*

values between different types of ADCPs or other acoustic instruments, even after application of Equation 2.4, because of transducer specific constants embedded in *EI*. Hence the need to calibrate the ADCPs for sediment monitoring and acoustic attenuation calculations. The constant k_c can be calculated as:

$$k_c = \frac{127.3}{T_e + 273} \tag{2.5}$$

where T_e is the temperature in Celsius and is approximated by the temperature given by the instrument per ping [*Teledyne RDI Instruments*, 2008]. In most acoustic inversions k_c is set constant, ranging from 0.43-0.55 [*Dienes*, 1999]. Equation 4B essentially subtracts the noise level in linear space and transforms it back to log space.

According to *Gostiaux and van Haren* [2010] Equation 2.4B facilitates the use of acoustic profiles near the noise floor by forcing profiles to asymptotically approach the noise level instead of falling below it. The challenge with this approach is that *NL* must be known accurately. If the *NL* value is lower than the actual noise floor, I_{db} will be below the noise floor, which is not physically possible, so selecting the correct *NL* value is important. The noise level has been previously defined as the lowest backscatter values in a profile [*Moore et. al.*, 2012; *Dienes*, 1999] or over the entire record [*Topping et. al.*, 2015; *Gostiaux and van Haren*, 2010]. Defining NL as the end of an attenuated profile assumes that the profile always reached the noise floor. It cannot be very effective in situations where the signal is not entirely attenuated by the end of the profile. Additionally, the *NL* can be found by using passive acoustics. This method measures the ambient sound when the instrument is not pinging.

When utilizing commercially available acoustic instruments to invert acoustic backscatter to sediment concentration, Equation 2.1 is first corrected for transmission losses due to spreading and fluid attenuation by calculating fluid corrected backscatter (*FCB*) in decibels as:

$$FCB = I_{dB} + \psi 20 \log_{10}(r) + 2r\alpha_f \tag{2.6}$$

where ψ is the near-field correction [*Downing et. al.*, 1995]. For this work, I ignore the near-field correction because it makes the profiles nonlinear, steepening the slope of FCB with range for the first couple of bins for the 1200 and 600 kHz ADCPs. *Topping*

and Wright [2016] found the same result for 'off-the-shelf' ADCPs of this type and recommended ignoring the correction. In our analysis, I only use range bins outside of the near-field for the analysis (r > 2.5 m), so this has no effect on our results. To account for two-way transmission losses associated with the viscous and scattering effects of sediment suspended in the ensonified volume, sediment corrected backscatter (*SCB*) is computed as:

$$SCB = FCB + 2r\alpha_s \tag{2.7}$$

where α_s is in dB/m.

2.2.2. Calculation of in-situ attenuation

The in-situ sediment attenuation, $\alpha_{s,\,\text{in-situ}}$, can be calculated from the *FCB* profile, which is the backscatter accounting for all components of the sonar equation except the sediment attenuation. So, the slope of *FCB* with respect to range gives an estimate of attenuation due to sediment. If the concentration, grain-size or GSD shape changes across the range over which attenuation is calculated, then it is impossible to know how much of the change is due to attenuation and how much is due to changes in the sediment properties.

When concentration and the GSD are relatively constant with respect to range, sediment attenuation can be calculated from the difference in *FCB* between any two points in the profile and dividing by the distance between those two points. However, more robust estimates of in-situ attenuation use the longest portion of the *FCB* profile. *Topping and Wright*, [2016] showed that incrementally decreasing the number of range bins used in calculations of in situ attenuation from horizontally-oriented ADCPs (with acoustic beams directed across a river channel) induced greater variability in the attenuation estimate.

Using extended portions of the *FCB* profile assumes that the sediment in suspension is relatively homogeneous through that ensonified volume. It is hard to satisfy this assumption using vertically-oriented ADCPs where the acoustic beams are directed down or up through a river flow due to concentration and grain size gradients. It

is easier to satisfy this requirement using horizontally-oriented ADCPs because the ensonified volume is at a constant level above the bed. This assumption is apt to be satisfied in rivers with regular cross-channel geometry, downstream of relatively straight reaches with well-mixed sediment suspensions [*Topping and Wright*, 2016]. The assumption is unlikely to be satisfied where local flow is strongly conditioned by upstream flow effects (e.g. downstream of river confluences where there is lateral stratification or river bends where there are strong secondary circulation cells driving suspended sediment flux). Fortunately, off-the-shelf, horizontal ADCPs are most commonly deployed in rivers for index-velocity discharge methods [*Ruhl and Simpson*, 2002; *Levesque and Oberg*, 2012], where the conditions apt to satisfy the assumption of homogeneous suspensions are likely to be met.

Under the assumption of a relatively homogenous ensonified volume, the slope of the *FCB* profile is solely a result of attenuation due to sediment, such that the sediment attenuation can be computed as:

$$\alpha_{s,in-situ} = -0.5 S_{FCB,r} \tag{2.8}$$

where $S_{FCB,r}$ =slope of the least-squares linear regression between *FCB* and range. I assess the effects of a cross-channel gradient in grain size and concentration below (Section 2.4.5).

2.2.3. Calculation of theoretical attenuation

Flammer [1962] shows that attenuation of sound from sediment can be attributed to three loss mechanisms: the scattering of sound by a particle as a function of the ratio of acoustic wavelength to particle circumference, $\alpha_{s,scatt}$, energy loss due to viscous shear which is a function of particle density and surface area, $\alpha_{s,visc}$, and heat loss due to conduction. Heat loss is significantly less in magnitude than scattering and viscous loss and is generally neglected [*Flammer*, 1962]. Here theoretical sediment attenuation is given by:

$$\alpha_{s,theo} = \alpha_{s,visc} + \alpha_{s,scatt} = M\overline{\zeta_{visc}} + M\overline{\zeta_{scatt}} = M\overline{\zeta_{total}} \tag{2.9}$$

where M is mass concentration (kg/m^3), $\alpha_{s,visc}$ is the attenuation of sound due to viscous losses and $\alpha_{s,scatt}$ is the attenuation of sound due to scattering losses. The overbar represents an ensemble averaged (i.e. averaged over a set number of pings) viscous and scattering attenuation coefficients ζ_{visc} and ζ_{scatt} (units of m^2/kg) are summed over the GSD. The scattering attenuation coefficient is described by *Thorne and Merel* [2008] as:

$$\overline{\zeta_{scatt}} = \frac{3\int_0^\infty a^2 \chi n(a) da}{4\rho_s \int_0^\infty a^3 n(a) da} \tag{2.10}$$

where ρ_s is sediment density, a is the particle radius in meters, and $n(a)$ is the particle number radius probability density function (essentially GSD by number). The variable χ is the intrinsic normalized total scattering cross section and is defined for natural sediment as [*Thorne and Meral*, 2008]:

$$\chi = \frac{0.29x^4}{0.95 + 1.28x^2 + 0.25x^4} \tag{2.11}$$

where $x = ka$, and k is the wavenumber for any given acoustic frequency.

The viscous attenuation coefficient has been described by *Urick* [1948] as:

$$\zeta_{visc} = \frac{k(G-1)^2}{2\rho_s}\left[\frac{s}{s^2 + (\rho_s/\rho + \delta)^2}\right] \tag{2.12}$$

for a given particle radius, a, where

$$s = \frac{9}{4ba}\left[1 + \frac{1}{ba}\right], \tag{2.13}$$

$$\delta = \frac{1}{2}\left[1 + \frac{9}{2ba}\right], \tag{2.14}$$

and

$$b = \sqrt{\frac{\omega}{2v}} \tag{2.15}$$

The fluid density is ρ, v is kinematic viscosity of water, $G = \rho_s/\rho$ and ω is the angular acoustic frequency. The forgoing assumes that the particles are spherical, which simplifies Equations 2.12 to 2.15. The viscous attenuation coefficient can be computed by integrating the viscous attenuation coefficient over the GSD by volume, *v(a)*, which is equivalent to:

$$\overline{\zeta_{visc}} = \frac{\int_0^\infty \zeta_{visc}(a) n(a) a^3 da}{\int_0^\infty n(a) a^3 da} \tag{2.16}$$

after *v(a)* is converted to *n(a)* [*Moore et. al.*, 2013]. To compute the theoretical sediment attenuation, mass concentration, *M*, and the grain size distribution, *n(a)*, must be known. Figure 2.1 shows theoretical values for the sum of the viscous and scattering attenuation coefficients (Eq. 2.10 + Eq. 2.16) using a log normal distribution and a relative standard deviation of 1.05 (the average of the samples collected as part of this work; see Section 2.3.3) for three common frequencies of 'off-the-shelf' acoustic Doppler profilers. The gray shaded regions represent the GSD range given by the particle size analysis and will be discussed more below.

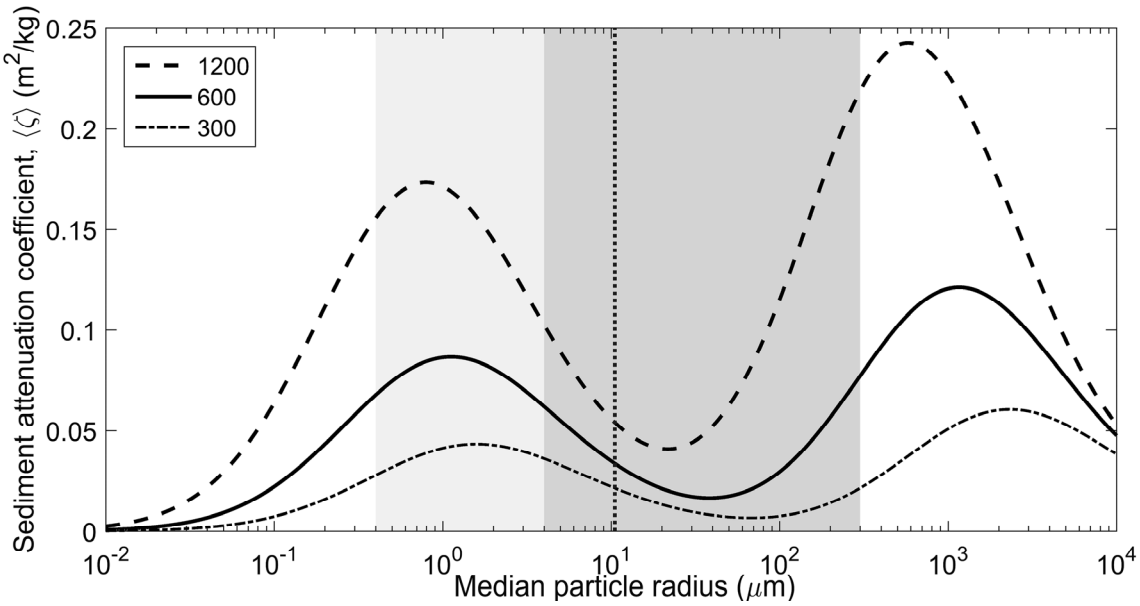

Figure 2.1. Theoretical attenuation coefficient ($\zeta_{visc}+\zeta_{scatt}$) as a function of median particle radius for a log normal distribution with a standard deviation of 1.05. Models used to derive attenuation coefficients assume that particles are spherical and the GSD is log normal. The theoretical attenuation coefficient represents the summation of Equation 2.10 and 2.16 integrated over the GSD. The light gray shaded region is the GSD range that the LISST either does not resolve or has difficulties resolving (0.4-4μm) and the darker gray shaded region is the additional GSD range resolved by both the LISST and the LS (4-300 μm). The vertical dotted line represents the mean particle radius (~10.5 μm) for all collected samples in our study.

2.3. Methods

2.3.1. Field Site

Field observations were from the Fraser River at Mission, British Columbia, 240 m upstream of a Water Survey of Canada (WSC) gauging station (no. 08MH024). Mission is ~85 km from the river mouth at the Strait of Georgia and 15 km downstream of the gravel-sand transition [*Venditti and Church*, 2014]. Here, the Fraser is confined to a single ~550 m wide channel carrying runoff from the 228,000 km^2 basin. This constraint provides an ideal location to measure the input of flow and sediment to the Fraser Delta and Estuary [c.f. *McLean et al.*, 1999; *Attard et. al.*, 2014]. The runoff pattern is dominated annually by the spring snowmelt, initiating a freshet beginning in April and ending in August/September. Peak flows typically occur in June. The mean

annual river flow at Mission from 1983 to 2013 was 3183 m^3/s and the mean annual flood from 1983 to 2013 was 9534 m^3/s. Flow at Mission is influenced by a tidal signal: during low flow periods significant stage variation occurs as tidal forces create a backwater effect, but the saline wedge only penetrates ~30 km upstream of the ocean at low flows and a few kilometers at high flows [see recent review in *Dashtgard*, 2012]. At high flow, stage variations are minor but velocity variations remain significant.

2.3.2. Acoustic Doppler setup

Three horizontally oriented acoustic Doppler current profilers (ChannelMaster™ H-ADCPs, Teledyne RDI, USA) were mounted on the Mission Harbour Authority dock just upstream of the Mission railway bridge. The river channel has a regular cross-section (Figure 2.2) and the river is straight for 3 km upstream of the site and there are no tributaries or back channel connections for 10 km. The three ADCPs were mounted in a horizontal array, separated by ~77 cm. The instruments have acoustic frequencies of 307, 614 and 1218 kHz, nominally 300, 600 and 1200 kHz. Each ADCP has two beams with a 20° angle from center. One-way beam spreading is 1.5° for the 600 and 1200 kHz and 2.2° for the 300 kHz. Care was taken during installation to reduce the pitch and tilt of the instruments to within ±0.1 degrees from zero. ADCPs were set to collect data over one minute with a one-minute rest before the next ADCP started collection, creating a 6-minute interval for all ADCPs. Ensemble averaging was done over 100 pings per minute. Instruments were set in low-bandwidth mode to allow for high resolution and the minimal noise at a cost of maximum range. The ADCPs collect data in 128 bins across the channel. The spacing of the bins and the distance across the channel over which measurements are obtained depends on the instrument. The 300 kHz instrument has 2 m bins and a 2 m blanking distance, so it nominally measures 258 m across the channel. The 600 kHz instrument has 0.5 m bins and a blanking distance of 2 m, so it measures 66 m across the channel. The 1200 kHz instrument has 0.25 m bins and a blanking distance of 2 m, so it measures 34 m across the channel. The practical ranges of the instruments, over which reliable backscatter can be calculated, are somewhat different and depend on the noise floor for the 1200 and 600 kHz ADCPs and where the 300 kHz ADCP signal hits either the riverbed or river surface during low flows (~60 m). The areas of the channel cross-section ensonified by the ADCPs are

shown in Figure 2.2. Acoustic backscatter data were recorded from 2012 to 2014, with several periods when data were not collected due power loss or instrument cleaning.

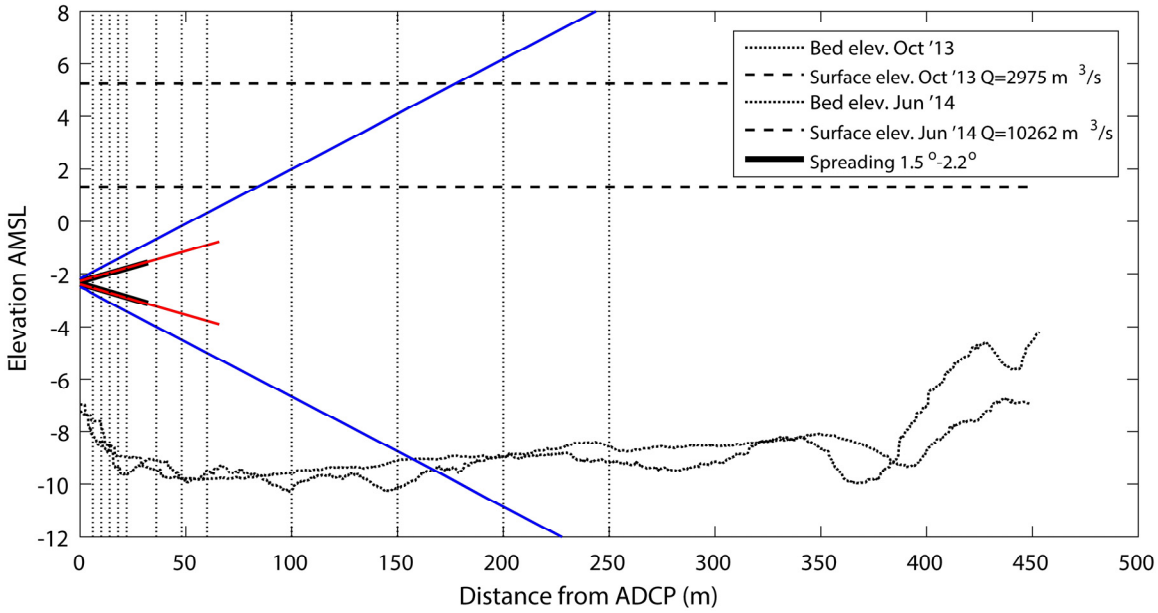

Figure 2.2. Ensonified areas of the 300 kHz (blue), 600 kHz (red) and 1200 kHz (black) ADCPs. Vertical black dotted lines represent in-beam sample locations respective to distance from the ADCPs.

2.3.3. Measured suspended sediment samples

The suspended sediment sampling consisted of 8 campaigns during the 2012 freshet, 8 campaigns during the 2013 freshet, and 11 campaigns during the 2014 freshet. Campaigns were designed to capture a wide variety of flows through the annual Fraser River freshet. A 90 kg brass USGS P-63 sampler was deployed using an electric USGS E-reel to collect point-integrated, isokinetic suspended sediment samples. A series of 'in-beam' samples were taken at calculated distances across the channel to align with the ADCP beams. Samples were obtained at 6, 10, 14, 18, 22, 36, 48, 60, 100, 150, 200 and 250 m from the ADCPs (Figure 2.2). The locations were chosen such that there were 5 roughly equally-spaced samples in each of the three acoustic beams (Figure 2.2). Samples were collected at the elevation of the ADCP based on a known distance below the water surface for a given water level measured at WSC gauging station 08MH024, 240 meters downstream of the ADCP array.

Each of the suspended sediment samples was processed in the SFU River Dynamics Lab using a LISST-100 (Sequoia Scientific, USA) instrument that uses laser

diffraction to calculate the grain size distribution and volumetric sediment concentration. The LISST-100 is mounted horizontally on a benchtop. Sediment and water samples go through the sampling volume using a flow-through cell provided by the manufacturer. This configuration allows for the analysis of a large number of samples (12-15/day) at relatively dilute concentrations. Sediment concentration was also obtained using the traditional filter method after the sample passed through the LISST-100. The effective grain-size range of the LISST-100 is 2-356 microns using the random shape configuration [*Agrawal and Pottsmith*, 2000]. LISST-100 GSDs are by volume (µL/L) and are therefore dimensionless.

To obtain a larger sediment mass (~5g) for GSD analysis, four samples were collected at the level of the acoustic beams (in-beam). These sediment samples were collected so that I could assess the accuracy of the much smaller P-63 samples and the LISST GSD. The larger sample provided enough sediment for use of a Beckman Coulter Laser Diffraction Particle Size Analyzer (LS-PSA; model LS 13 320) which has a larger range than the LISST-100 (0.4-2000 microns), and utilizes similar diffraction theory to obtain the grain size distribution. The larger samples were collected at distances of 18 and 48 m from the ADCP array using a modified P-61 on June 19, 2014 at a discharge of 10,000 m^3/s and July 22, 2014 at a discharge of 5,000 m^3/s. The modified P-61 pumps a sample to the surface through a tube connected to the inside nozzle at flow rates that match the velocity at the nozzle. The velocity at the depth of the nozzle was measured using a down-facing 600 kHz ADCP. This P-61 modification allowed for large sediment samples to be collected isokinetically. Samples were then decanted, split and run through both the LISST-100 the LS-PSA. Both instruments give a GSD by volume that is further converted to as GSD by number for the computation of theoretical attenuation [see *Moore et al.*, 2013].

2.3.4. Data quality assessment

In addition to ambient noise that occurs during low sediment concentrations, data spikes may occur when the ADCP internal clock drifts during deployment, which creates overlapping pings with different instruments at the same time. Temporal clock drift occurred over periods of days to weeks when the ADCPs are deployed in ‘stand-alone’

mode which relies on an internal clock. Since the ADCPs are different frequencies interference should not occur, but I do see signal interference that occurs when pings overlap and therefore take a precautionary step in deleting the data. This highlights the importance of using a data logger or computer to control the ping of each instrument, especially during a multiple instrument setup. For these data, I deleted any pings that overlapped. During cold conditions in the Fraser River, when temperatures dropped below 3 degrees Celsius, either ice development on the face of the transducer or in the water column caused poor signals. ADCP observations made below 3° Celsius were removed from the dataset.

2.4. Results

2.4.1. Grain size distributions for sediment samples

Large Samples collected with the modified P-61

The primary purpose of the large samples was to obtain enough sediment to assess the accuracy of the LISST GSD, which I used for analysis of the vast majority of our samples, against the GSD obtained from an instrument with a wider grain-size. The LS-PSA GSD has a range from 0.4 microns (the lower range of the LS-PSA) to 300 microns (Figure 2.3a and b). The distributions from the LS-PSA are log normal with a median particle diameter D_{50} ranges between 11 and 13 microns (Table 2.1). Geometric standard deviation was ~3.7 and 4.3 microns on June 19, 2014 and July 22, 2014 respectively. Distributions from the LISST are also log normal, but the finest 2-3 bins give the distributions an open-ended bimodal appearance (Figure 2.3a and b; Figure 2.4). The integral of the LISST distribution <4 microns is 75-91% of the LS-PSA distribution <4 microns. This suggests that in this case the LISST lumped all sizes < 2 microns into the finest LISST grain-size bins. The true distributions are not bimodal. In this case, presentation of a median grain-size is acceptable and the D_{50} of the LISST is nearly identical to the LS-PSA data (Table 2.1).

Table 2.1 Median particle diameter measured with the LISST 100 and LS-PSA.

Instrument	LS-PSA P-61 split sample				LISST-100 P-61 split sample				LISST-100 P-63 IB sample			
Date	**19-Jun-14**		**22-Jul-14**		**19-Jun-14**		**22-Jul-14**		**19-Jun-14**		**22-Jul-14**	
Distance from the ADCPs (m)	**18**	**48**	**18**	**48**	**18**	**48**	**18**	**48**	**18**	**48**	**18**	**48**
Grain-size (microns)	**12.7**	**13.0**	**11.2**	**12.4**	**12.6**	**10.6**	**11.2**	**13.1**	**16.7**	**20.4**	**18.0**	**16.9**

In order to calculate theoretical attenuation using Equation 2.10, I must convert GSD by volume to GSD by number, which I do using the method outlined in *Moore et al.* [2013]. The lower open-endedness of the LISST-100 GSD introduces a bias in the theoretical attenuation (Eq. 2.10 + Eq. 2.16) calculated from the LISST-100 GSDs because the fine silt and clay in suspension is unaccounted for. Attenuation calculated from the LS-PSA GSD is 1.96 times the LISST attenuation (Figure 2.3c). It is probable that this bias is directly related to the bias in the finest grain sizes of the LISST-100. This bias could be applied to the results, but it would assume that the fine silt and clay portion of the GSD during the freshet does not change through the year, which is unreasonable. Nevertheless, the bias is consistent over 2x range of sediment concentration.

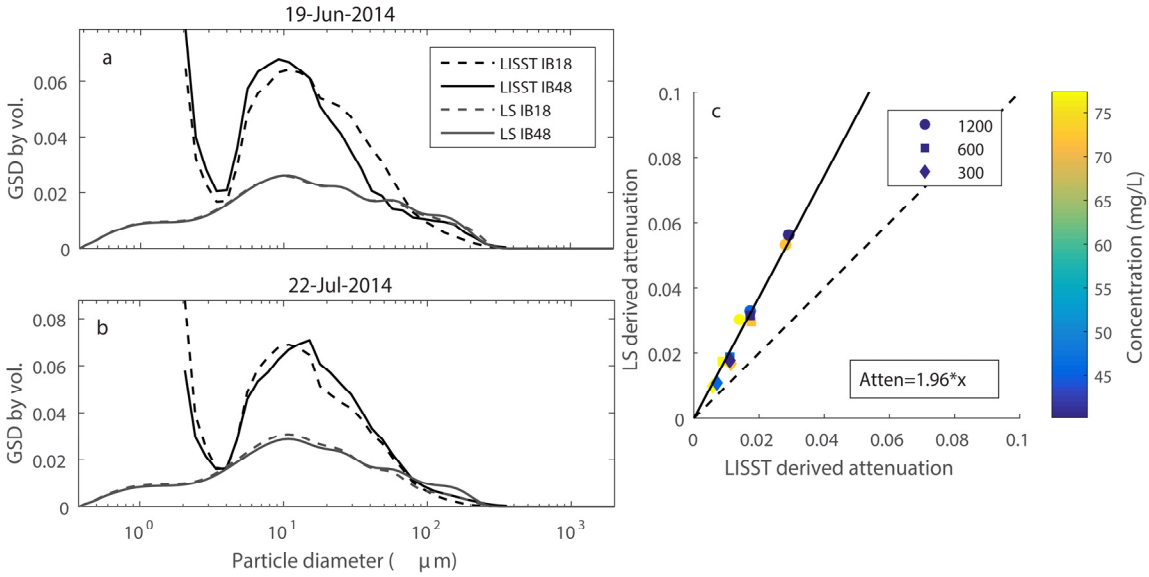

Figure 2.3. LISST-100 and LS-PSA GSDs by volume extracted from the large volume samples collected in beam at 18 m (IB18) and 48 m (IB48) from the ADCPs on (a) June 19, 2014 and (b) July 22, 2014. (c) Comparison of theoretical attenuation calculated using LS-PSA and the LISST-100 GSDs for the 1200, 600 and 300 kHz ADCPs.

Bottle samples collected with P-63

The LISST GSDs from the P-63 sampler are somewhat different than the larger samples used in the comparison of particle sizer instruments described above. Bottle sample GSDs are generally log normal and do not have the open-ended fine mode, which I suspect to be inaccurate. Figure 2.4a shows a randomly selected subset of GSDs as a function of discharge from samples collected between 2012 and 2014. The GSDs (Figure 2.4a) show that particles in suspension span the entire range of sizes measured by the LISST-100. Figure 2.4a shows a weak secondary mode in the GSD at ~75 microns, in the late rising limb to the peak of the hydrograph, reflecting resuspension of locally sourced finer bed material. The GSDs tend to broaden during the freshet. Interestingly, Figure 2.4a also shows that the GSDs tend to become coarser during the lower flows, likely because there is little fine material supplied from the watershed and only local bed material is being moved. The absence of the open-ended fine tail suggests that the bias may only occur at high flows. These observations reinforce our decision not to apply a bias correction for the difference between the LS-PSA and LISST-100 GSDs observed in Figure 2.3.

Bottle samples collected over the three-year sample period show that mean concentration was ~90 mg/L (St. dev. = 57 mg/L) (Figure 2.4b). The concentration generally increased beyond 60 m range; consequently, the range of ADCP profile included in this analysis was limited to 60 m so that assumptions made in Equation 8, of a constant sediment concentration and GSD within the ADCP beams, would hold. The mean particle diameter for samples taken in the beam of the ADCPs was ~ 21 microns (Figure 2.4c) with a mean geometric standard deviation of 2.6.

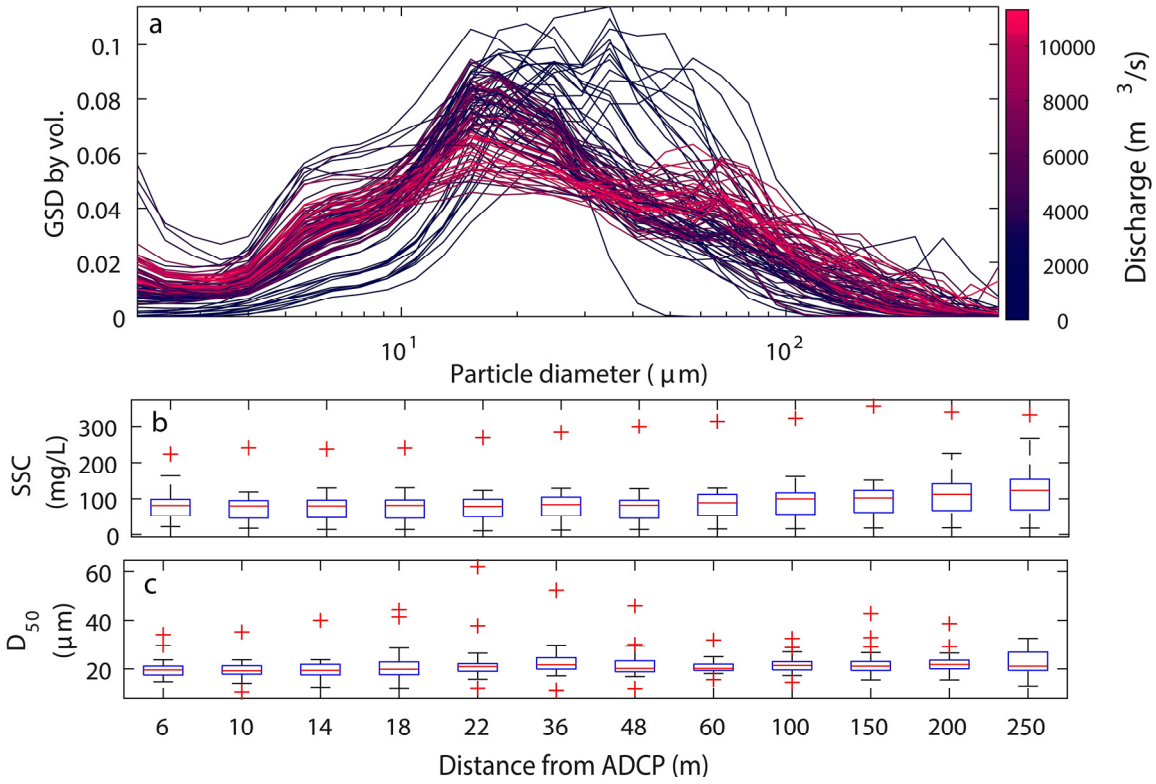

Figure 2.4. P-63 bottle samples collected from 2012-2014. (a) Suspended sediment concentrations obtained by filtering and (b) median diameter (D_{50}) of samples obtained from the LISST-100, as a function of distance from the ADCPs. (c) Grain size distributions for a subset samples collected from 2012-2014 as a function of discharge. For each box in (a) and (b), the central mark is the median, the edges of the box are the 25th and 75th percentiles, while the whiskers extend to 99.3 coverage of a normal distribution (2.7σ). The most extreme data points are considered outliers (red +).

2.4.2. Characteristics of acoustic profiles

Figure 2.5 shows the general characteristics of the ADCP profiles at various flows selected throughout the three years of sampling. The 300 kHz ADCP profile hits the river bed or water surface prior to reaching the noise floor at ~60 m, which can be seen in Figure 5a by the bump in the *EI* curves. Detection of the river bed and surface are discussed in more depth in *Wright et al.* [2010] and *Moore et al.* [2012], respectively. For the 300 kHz signal, the noise floor is never reached between the ADCPs and the 60 m truncation. The *EI* profile out to 60 m tends to be linear at high concentrations and noisy at low concentrations. At low flows, 300 kHz *EI* profiles have a decreasing slope with range (concave) out to 30 m and are noisy beyond 30 meters, where either the surface or bed obstructs the signal. At high flows the surface tends not to obstruct the signal and profiles are less noisy due to the higher concentrations, which generally produces a more linear profile.

The 600 kHz *EI* profile has a slight decrease in slope with range making it concave. The whole profile shifts vertically depending on concentration or grain size in Figure 2.5b. At high concentrations, profiles have higher *EI* at the beginning of the profile and lower *EI* at the end of the profile. At high flows, the 600 kHz *EI* signal visually appears to reach the noise floor, but not at low flows. The 1200 kHz *EI* profile is strongly concave and consistently appears to reach the noise floor (Figure 2.5c). The distance from the instrument at which it reaches the noise floor varies with the number of scatterers in the ensonified volume and therefore sediment concentration and discharge.

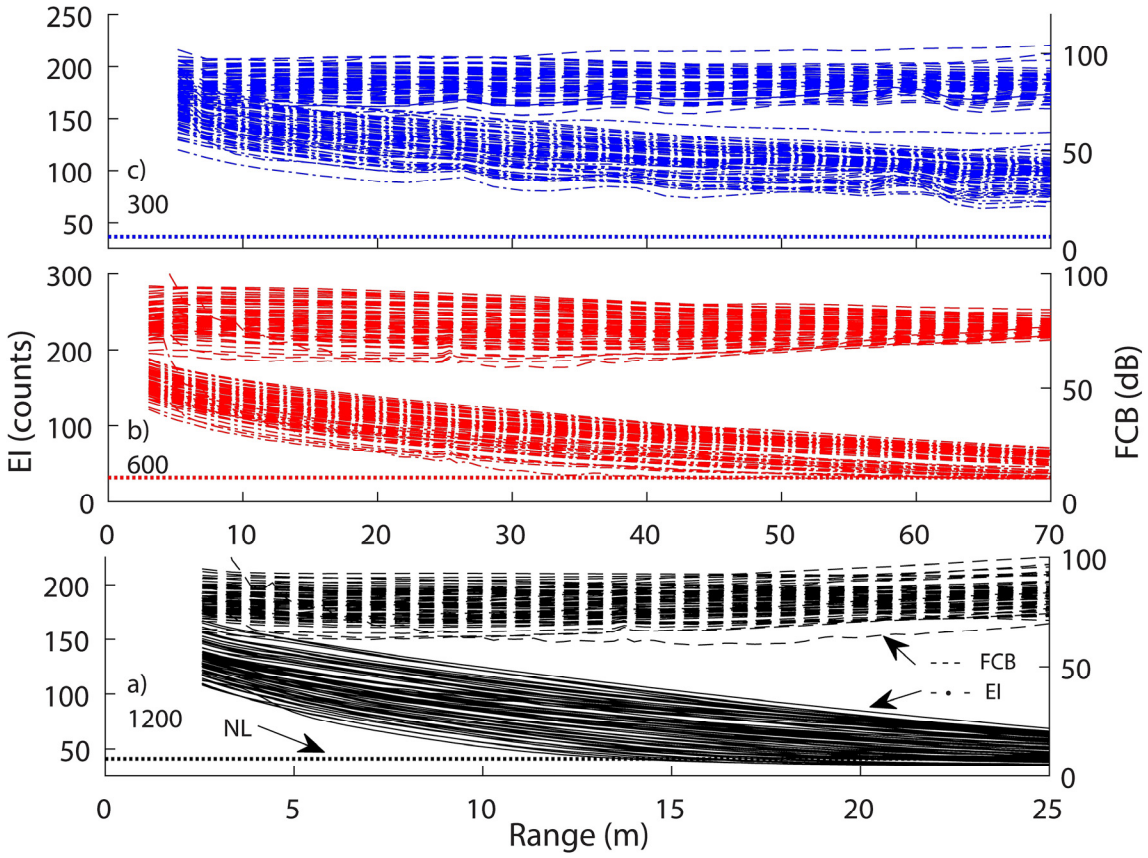

Figure 2.5. Acoustic profiles in from 2012-2014 randomly selected throughout the dataset for the (a) 300 kHz, (b) 600 kHz, and (c) 1200 kHz ADCPs. The horizontal dotted line represents the NL defined by the passive acoustics. Fluid corrected backscatter (FCB) are calculated from EI profiles using Equations 2.4A and 2.6.

Figure 2.5 shows *FCB* calculated using Eq. 2.4A and Eq. 2.6. The 300 kHz *FCB* signals tend to flatten at high concentrations, but the noise at low concentrations is exacerbated. For the 600 kHz ADCP, *FCB* profiles flatten at higher concentrations and exhibit an increase in slope with range making them convex at low concentrations. A trend line fit to these convex profiles would have a positive slope. *FCB* profiles are often convex and positively sloped for 1200 kHz ADCP because *EI* reaches the passive acoustic noise floor frequently due to its higher frequency.

2.4.3. The influence of the acoustic noise floor (NL) on in-situ attenuation

The shape of the *FCB* profiles affects in-situ attenuation because it is defined by a linear regression between *FCB* and range. A constant *FCB* profile slope gives the

most robust estimates of the in-situ attenuation. When the *FCB* profiles are non-linear (concave or convex), the estimate of in-situ attenuation is less reliable. Use of Equation 2.4A is justified for the 300 kHz instrument because the signal does not reach the noise floor within the 60 m range examined. The echo level never goes below 80 counts (~2x the passive acoustic noise level). However, Figure 2.5 shows that Equation 2.4A should not be used to calculate *FCB* for the 1200 kHz instrument or when the 600 kHz instrument reaches the noise floor because it makes the profiles non-linear. This is highlighted in Figure 2.6 which shows four profiles for both high (<SSC>=263 mg/L, April 25, 2014) and low concentration (<SSC>= 16 mg/L, October 3, 2013) for the 1200 and 600 kHz ADCPs. The 1200 kHz *FCB* profiles are concave using Equation 2.4A at high (Figure 2.6a) and low concentrations (Figure 2.6c), showing that it reaches the noise floor in both conditions. The concavity is less obvious in the 600 kHz *FCB* profiles at low concentrations using Equation 2.4A (Figure 2.6d), but is present at higher concentrations (Figure 2.6b). The concavity in the profiles does not appear to be due to changes in concentration or grain size in the ensonified volume. The difference between the inflection point to the end of the profile are between 10 and 13 dB for Figures 2.6a and 2.6c using Equation 2.4A. This would require a 3-4X increase of SSC and/or D_{50} in linear space to account for a 12 dB change, which I do not see in our sediment samples.

There are two methods to avoid the profile concavity. I could conservatively truncate the profile above the noise floor at low concentrations as suggested by *Topping et al*. [2015]. But this would remove nearly 50% of the 1200 kHz profiles at high concentrations, where there is useful data. Additionally, truncation of a concave profile at low concentrations can lead to biasing the profile in the steeper portion, which can influence the linear regression and therefore the estimate of in-situ attenuation. The alternative is the application of Equation 2.4B, which corrects the profile concavity, but requires an objective method for estimating the noise floor that reflects the variation where the profiles reach the noise floor at different flows (Figure 2.5). Thus, I explore different approaches for calculating *NL* to see the influence that they have on an individual profile when converting echo intensity from counts to decibels.

Noise levels were estimated using the passive acoustic approach; at high flow (May-July, 2014) and low flow (Feb.-March 2014) when a tidal backwater affected the flow (Table 2.2). Values of *NL* are within a few percent of each other at low and high flows for the 1200 kHz ADCP. At high flows, *NL* is 8-9% larger than at low flows for the

600 kHz ADCP and *NL* is 89 to 116% larger for the 300 kHz ADCPs (Table 2.2). The increase in *NL* at high flows suggests that the 600 and 300 kHz instruments are more sensitive to ambient noise related to sediment in suspension at high flows. Noise levels were also calculated following previous authors as the minimum *EI* in a profile [*Moore et. al.*, 2012; *Dienes* 1999] and the lowest *EI* over the entire data record [*Gostiaux and van Haren*, 2010; *Topping et. al.* 2015] (Table 2.2).

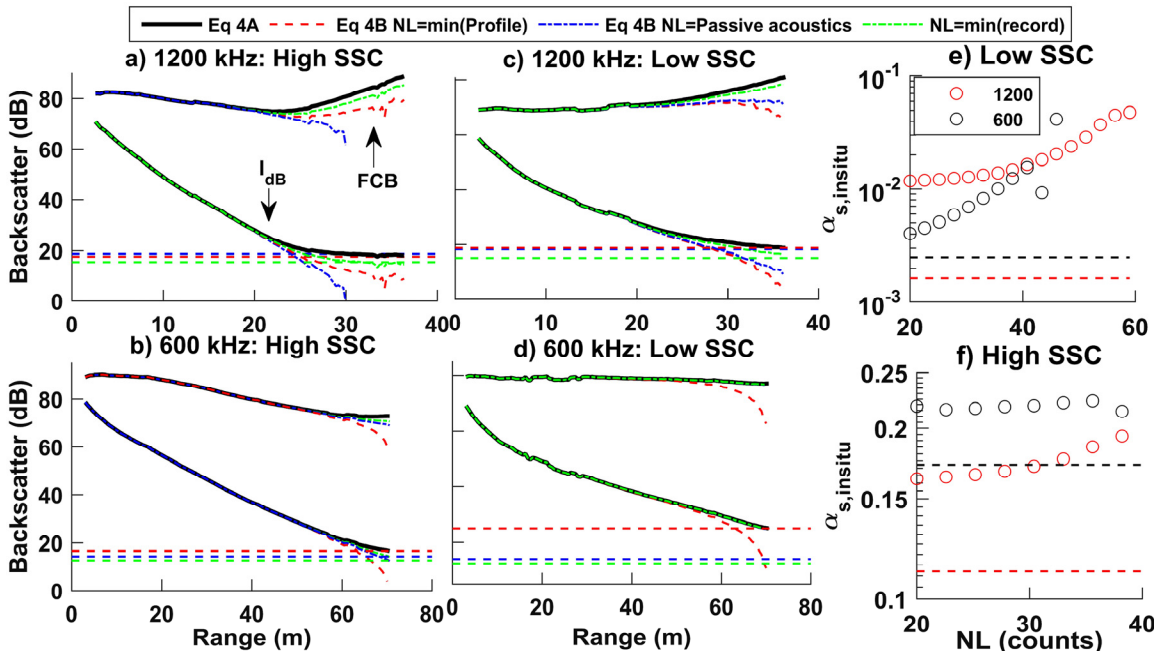

Figure 2.6. I_{dB} and FCB profiles calculated using Eq. 4A and 4B, via Eq. 6 with NL being defined by the minimum of the record, passive acoustics, and minimum of the profile during (a & b) high suspended sediment concentration (SSC) sampling period (April 25, 2014) and (c & d) low SSC period (October 3, 2014) for the 1200 and 600 kHz ADCPs. In-situ attenuation as a function of NL for acoustic profiles using Eq. 4B at low e) SSC and f) high SSC. In panels a-d, the dashed horizontal lines are the NL (in decibels) for the respective definitions. In panels e & f, the horizontal dashed line is the theoretical attenuation measured using LISST GSDs.

Table 2.2. Range of noise level (NL) values calculated from passive acoustics and the minimum of the individual profiles and the full record.

NL by passive acoustics (counts)							
		1200		600		300	
	n	Beam 1	Beam 2	Beam 1	Beam 2	Beam 1	Beam 2
High flow	3	41	40	34	40	69	73
Low flow	15	41.5	41.1	31.4	36.6	37.7	33.9
% change		0%	-2%	9%	8%	82%	116%
Median value (used in further analysis)		41	41	32	37	n/a	n/a
NL by profile minimum (counts)							
		1200		600		300	
		Beam 1	Beam 2	Beam 1	Beam 2	Beam 1	Beam 2
Full record		34 to 84	38 to 83	28 to 111	34 to 117	n/a	n/a
NL by record minimum (counts)							
		1200		600		300	
		Beam 1	Beam 2	Beam 1	Beam 2	Beam 1	Beam 2
Full record		34	38	28	34	n/a	n/a

Figure 2.6 shows the effect of each *NL* definition on the I_{dB} and *FCB* profiles for the 1200 and 600 kHz instruments. I elected to use the passive acoustic median value of *NL* for the 1200 and 600 kHz instruments across all flows in Figure 6. Because the 300 kHz ADCP does not reach the noise floor I do not investigate the influence of *NL*. Deviations from a linear I_{dB} profile occur at ~20m for the 1200 kHz instrument and ~50 m for the 600 kHz instrument, but the location where the deviations occur is different for high and low flows, making truncation of the profiles at a constant range difficult.

For the 1200 kHz signal, the I_{dB} profiles are pulled below the noise floor using the passive acoustics, the profile minimum and the record minimum to define *NL*, except at low concentration using record minimum as the *NL* (Figure 2.6a and 2.6c). In general, when the *NL* value is underestimated, *FCB* profiles are more concave and, when *NL* is overestimated, *FCB* profiles are more convex. Using the passive acoustic definition, *NL* flattens the profiles and makes them more linear at low concentration (Figure 2.6c) and linear with a convex far range at high concentration (Figure 2.6a). Using the minimum profile *NL* flattens the 1200 kHz profiles at low concentration, making them slightly

convex, but makes them concave at high concentrations. Using the record minimum produces strongly concave profiles at low and high flows.

For the 600 kHz signal at low and high concentrations, profiles are less affected by concavity and are instead more affected by convexity due to the definition of *NL* (Figure 2.6b and 2.6d). When defining *NL* by passive acoustics or the minimum of the record, the far range of the profile appears relatively flat at both concentrations. Using the profile minimum, profiles are artificially pulled below the noise floor, producing convex profiles and suggesting that the *NL* value is too large. The inaccuracies that occur when defining the *NL* by the minimum of the profile are likely due to the fact that the noise floor is not reached during low concentrations and may only be approached at higher concentrations (Figure 2.6).

The forgoing analysis suggests that the passive acoustics method most consistently produces near-linear *FCB* profiles using Equation 2.4B. None of the methods for defining *NL* provide *FCB* profiles with a constant slope, causing a problem for calculation of in-situ attenuation. Yet the passive acoustic definition of *NL* seems to produce the most reasonable results. However, in-situ attenuation from the passive acoustic definition of *NL* produces attenuation that is an order of magnitude larger than theoretical attenuation at low concentration and somewhat larger values at high concentration (Figure 2.6e and 2.6f).

In order to determine if there is a particular value of *NL* that would give linear *FCB* profiles and reasonable in-situ attenuation, I varied *NL* values between 27 and 55 counts for a low concentration profile (October, 3, 2013) and 27 and 36 for the high concentration profile (April 25, 2014) and calculated $\alpha_{s,\text{in-situ}}$. Values of *NL* higher and lower than these ranges produced strongly concave or convex profiles. Increasing *NL* generally increases $\alpha_{s,\text{in-situ}}$. However, $\alpha_{s,\text{in-situ}}$ is more sensitive to *NL* at low concentrations (Figure 2.6e) than at high concentrations (Figure 2.6f) when acoustic profiles tend to be steeper. There is no value of the *NL* that gives linear profiles and matching values of $\alpha_{s,\text{in-situ}}$ and $\alpha_{s,theo}$ for both concentrations.

Nevertheless, I require a semi-automated method to compute $\alpha_{s,\text{in-situ}}$. I use Equation 2.4A for the 300 kHz ADCP since the noise floor is not reached. The passive acoustic method for defining *NL* produces values that vary with sediment concentration

so I elected to use an *NL* value in Equation 2.4A of 36 counts, which is the average value for both beams at low flow. For the 1200 and 600 kHz ADCP, I apply Equation 2.4A when the difference between the minimum over the entire record (all profiles) and the minimum of the instantaneous profile is greater than 10 [*Gostiaux and van Haren*, 2010] and Equation 2.4B when the difference is less than 10 (i.e. near the noise floor). When the profile is near the acoustic floor, *NL* is defined by passive acoustics. As in Figure 2.6, I elected to use the passive acoustics median value of *NL* for the 1200 and 600 kHz instruments across all flows. This method prevents the tail of the profile from artificially increasing the slope of the profile. For the 1200 kHz ADCP, which is found to reach the noise floor over most of the year, I additionally truncate the profile at the inflection point (i.e. minimum of the *FCB* profile). In doing so, I correct the profiles for non-linearity, when they approach the noise floor, before they are truncated.

2.4.4. Comparison of in-situ and theoretical attenuation

Figure 7 shows the theoretical attenuation from LS-PSA GSDs from the large sediment samples computed from Equation 2.9 compared to in-situ attenuation calculated from measured backscatter profiles collected at the same time. Data points represent samples from two locations (IB18 and IB48), collected on two days, for each frequency. Recall that the 300 kHz instrument exhibited time stamp drift for the time period over which the low concentration large samples were collected, so those data are excluded in Figure 2.7. At high concentration the attenuation values generally fall close to the line of unity, while at lower concentrations the in-situ attenuation is greater than that of theoretical values. The 1200 kHz in-situ attenuation at high concentrations range from 0.8 to 1 times that of theoretical attenuation, while at low concentrations in-situ attenuation is 1.8 to 2.1 times that of theoretical attenuation. For the 600 kHz at high concentrations, in-situ attenuation are 1.25 times greater than theoretical, while at low concentration values are 2.2 times greater. At high concentration the 300 kHz in-situ attenuation is 1.9-2.7 times greater than theoretical coefficients. Though there were only four samples collected, these results suggest that at higher concentrations the in-situ method of estimating attenuation compares well with theoretical attenuation.

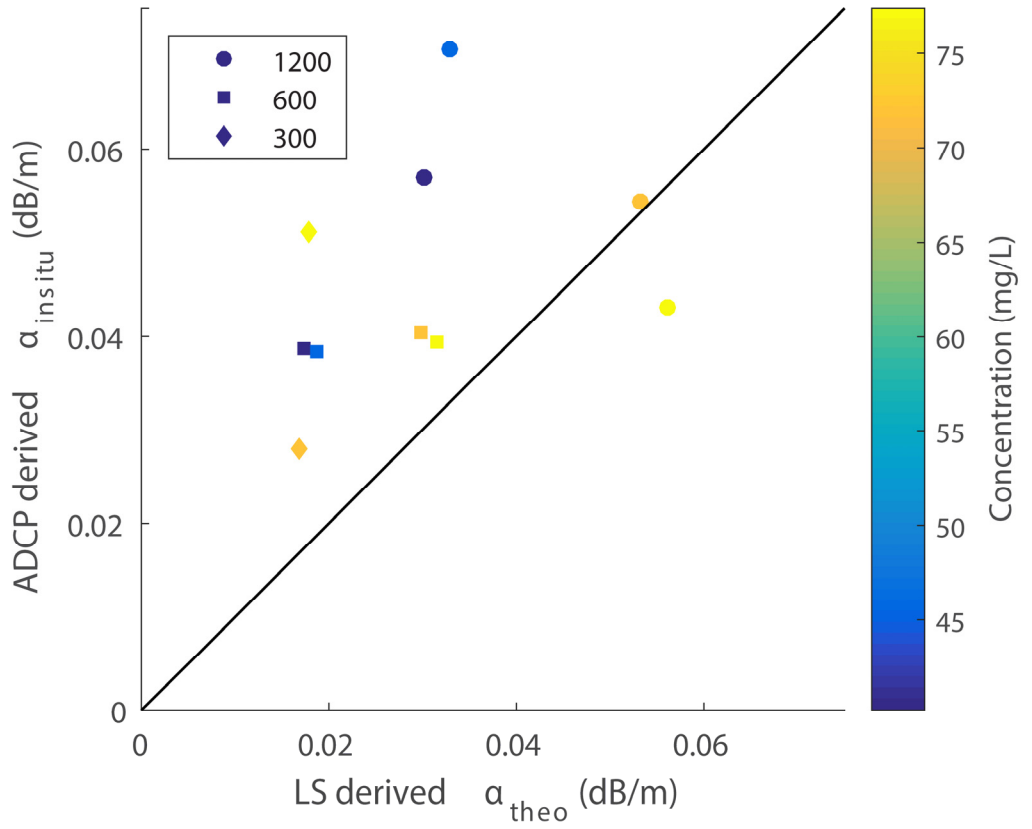

Figure 2.7. Comparison of theoretical attenuation ($\alpha_{s,theo}$) derived from the LS-PSA analyzed large sediment samples with in-situ attenuation ($\alpha_{s,in\text{-}situ}$) from the ADCPs.

Comparison of in-situ and theoretical attenuation computed from GSDs of P63 bottle samples (analyzed with LISST-100) shows that many points cluster around the line of unity (Figure 2.8). Many of the outliers have large relative errors derived from the regressions, suggesting a nonlinear profile. However, $\alpha_{s,\text{in-situ}}$ is generally larger than $\alpha_{s,theo}$, particularly at low concentrations. There is no obvious linear relation between $\alpha_{s,\text{in-situ}}$ and $\alpha_{s,theo}$. Attenuation is generally in better agreement between the two methods at higher concentration than at lower concentration. Figure 2.8 shows that in-situ attenuation is generally greater than theoretical attenuation. This is likely a result of the LISST underestimating the viscous attenuation from fine silt and clay, which is smaller than it can measure. Had that sediment been spread across finer sizes as it is in the LS GSDs, theoretical attenuation would have been somewhat larger.

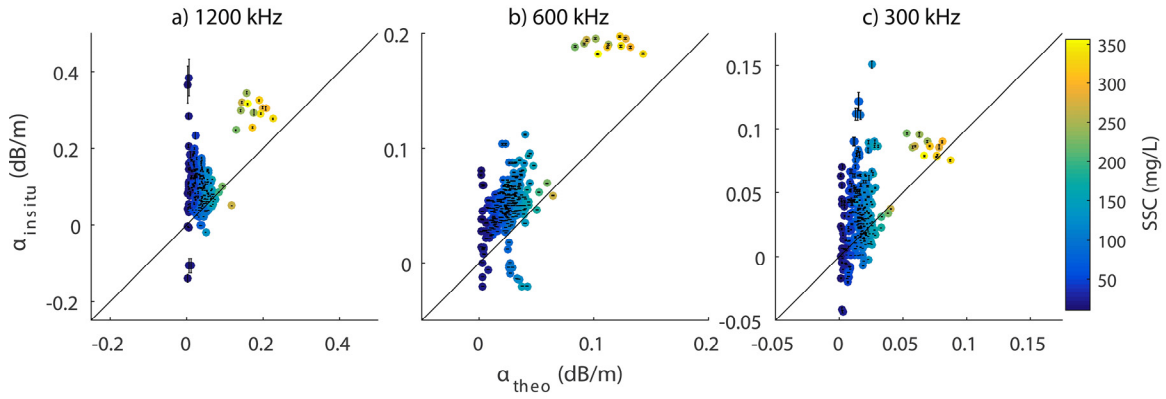

Figure 2.8. Comparison of theoretical attenuation ($\alpha_{s,theo}$) (derived from the LISST-100 analyzed P-63 sediment samples and in-situ attenuation ($\alpha_{s,in\text{-}situ}$) as a function of concentration for the a) 1200, b) 600 and c) 300 kHz ADCPs. Error bars are derived from the error of the regression slope used to calculate in-situ attenuation.

2.4.5. Effect of cross-channel concentration and particle size variation on acoustic profiles shape

The tendency of $\alpha_{s,\text{in-situ}}$ to converge towards $\alpha_{s,theo}$ at higher concentrations (Figure 2.8) is a curious result and begs the question of whether there is some ensonified volume sediment size or concentration gradient affecting the acoustic profiles. To assess if the ensonified volume concentration gradients are affecting our acoustic profiles I selected three days in which the concentrations represent a low, medium and high concentration relative to all sampling campaigns between 2012 and 2014. Figure 2.9 a-c shows coupled 600 kHz daily average *FCB* and *SCB* profiles for the low, medium, and high SSC sample dates (October 3, 2013, June 6, 2013, April 25, 2014, respectively), using Equation 2.4A, 2.6 and 2.7 to give an un-manipulated perspective. Minimum *EI* values for the 600 kHz instrument are 56, 68, and 37 counts for Oct 3, 2013, June 6, 2013, April 25, 2014, respectively, which suggests Eq. 2.4B would be applicable only on April 25th, 2014 and that the use of Eq. 2.4A is appropriate for the other dates.

At low concentrations (Figure 2.9a), a discontinuity in the cross-channel concentration profiles can develop with SSC that is 50% to 2 times the reference concentration 1 m from the ADCP, which is reflected in the large standard deviation in the *FCB* profiles and in the relatively poor coefficient of determination. On October 3, concentration changes from ~11 mg/L to ~22 mg/L between 6 and 22m, while the D_{50} remains relatively constant. After 22 m the D_{50} varies by ~10μm around the mean D_{50} of

39µm. The observed twofold change in the concentration across the profile accounts for a 3 dB change in acoustic intensity ($10*\log_{10}(1/2)$= -3 dB and $10*\log_{10}(2/1)$= 3 dB) that amounts to the variability seen with in the shaded area. At any range from the ADCP, the acoustic intensity in decibels is relative to the reference intensity measured at 1m from the ADCP [see *Moore et. al.*, 2012], therefore when comparing the concentration nearest to the ADCP to that at any range, assuming all other parameters are constant, illustrates how inhomogeneity can influence the acoustic profile. The measured fluctuation in suspended sediment through the ensonified volume reflects the change in the *FCB* profile, while the least squared regression does not adequately capture the trend near the ADCP.

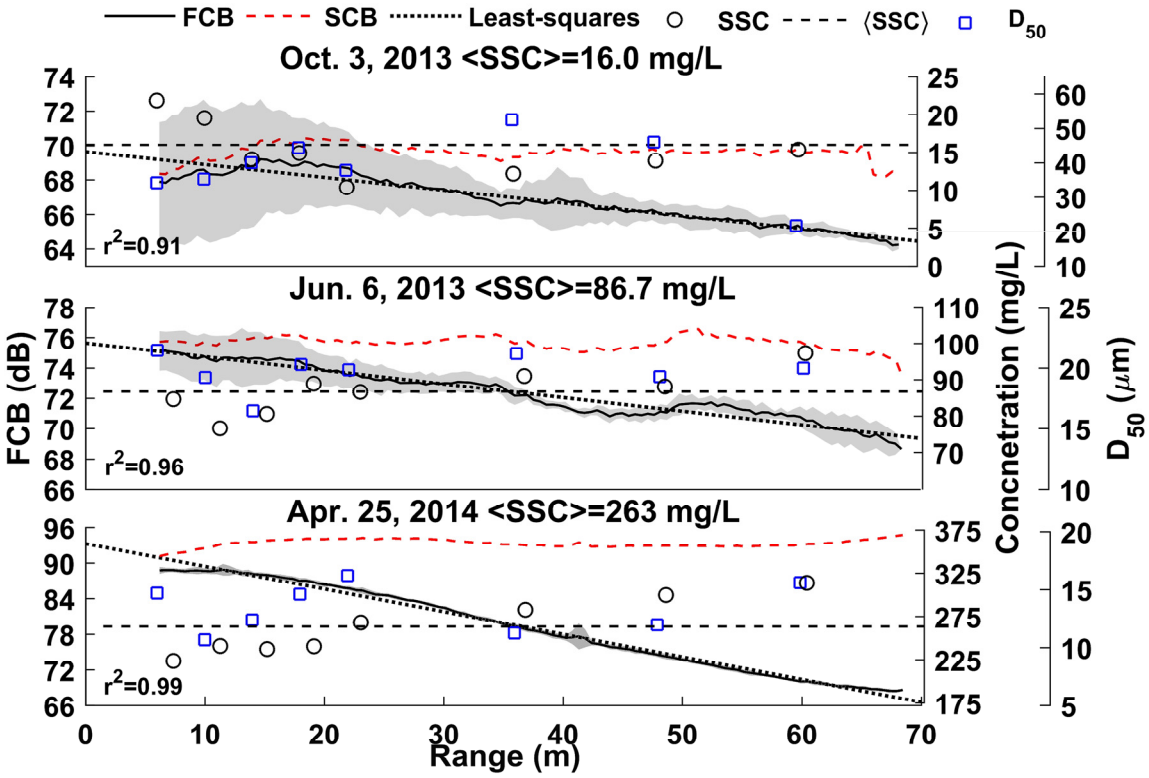

Figure 2.9. Acoustic profiles showing FCB calculated using Equation 2.4A and SCB profiles averaged over the collection period on (a) Oct. 3, 2013, (b) June 6, 2013, and (c) Apr. 25, 2014 using the 600 kHz ADCP. The dotted line is a least-squares regression through the FCB-range relation. The shaded area encompassing the FCB profiles represents the standard deviation around the daily mean FCB profile (12 profiles). Brackets represent spatial average of SSC along the 60 m beam range.

At medium concentrations (Figure 2.9b), D_{50} is relatively stable, changing by only ~5 μm and the concentration fluctuates about 5 mg/L around the mean concentration of 86.7 mg/L. *FCB* profiles decrease ~5 dB with range, have smaller deviations around the mean *FCB* profile, and the coefficient of determination becomes stronger. This -5 dB change would require ~30% change in concentration across the ensonified volume (with respect to the reference SSC) which is not seen in the SSC measurements, suggesting that the acoustic decrease is due to sediment attenuation. *FCB* profiles show the least-square regression traces the profile well with very small residual values, suggesting a more robust in-situ attenuation.

At high concentrations (Figure 2.9c) there is a ~20 dB decline in *FCB* across the channel. This would require a decrease in concentrations of 220 mg/L, which is not observed, instead concentration increases with range. The observed change in concentration is a ~ 100 mg/L increase or ~1.6 dB. Variability around the average *FCB* profile is small and the least-squares regression traced the profile well with small residuals and the coefficient of determination is strong. Therefore, the difference between *SCB* and *FCB* is primarily due to sediment attenuation across the channel.

This assessment provides a way to check whether concentration or particle size gradients influence the acoustic profile and therefore the in-situ attenuation computation. Figure 2.9 shows that at low concentrations the in-situ attenuation is unreliable. As the concentration increases the in-situ attenuation estimate become more robust and concentration or particle gradient become acoustically negligible relative to the absolute concentration.

2.4.6. Effect of concentration on in-situ attenuation

The potential for substantial cross stream concentration changes at low concentration suggests that there may be a lower concentration limit below which $\alpha_{s,\text{in-situ}}$ cannot reliably be calculated. To explore this possibility, I computed the difference between $\zeta_{total,theo}$ and $\zeta_{total,\text{in-situ}}$ and plot it as a function of concentration and particle diameter (Figure 2.10). At low concentration the difference between in-situ and theoretical attenuation coefficients is greatest and as concentration increases the difference converges towards zero. Given that there is not a large variation in median particle radius it is difficult to assess the influence it may have on attenuation

coefficients, but there appears to be no relation between particle diameter and the difference between attenuation coefficients. Additionally, I found no relation between the difference between $\zeta_{total,theo}$ and $\zeta_{total,\text{in-situ}}$ and the coefficient of determination from the regression or the geometric standard deviation of the GSD (not shown). These results (Figure 2.10) show that the threshold concentration below which in-situ attenuation is unreliable is ~50 mg/L for the 1200 and 600 kHz ADCPs and ~75 mg/L for the 300 kHz ADCP for Fraser River sediments.

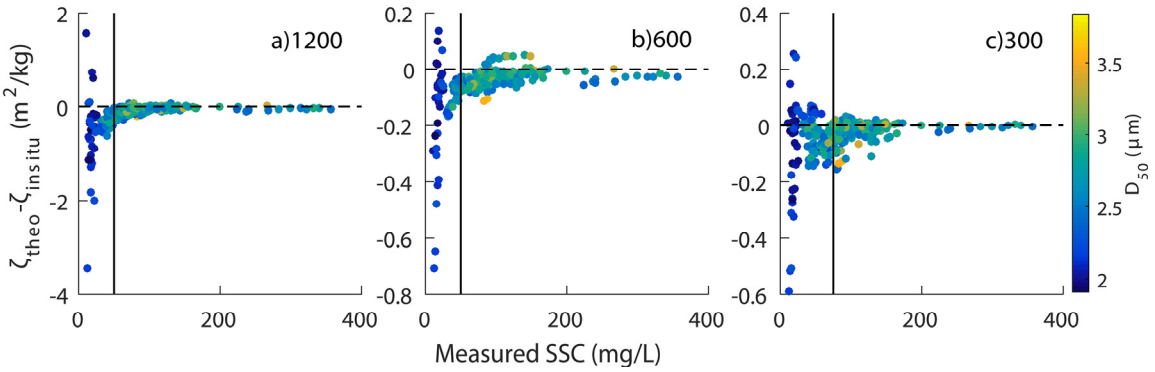

Figure 2.10. Difference between theoretical (Equations 2.10 + 2.12) and in-situ attenuation coefficients as a function of concentration and particle diameter for the (a) 1200, (b) 600, and (c) 300 kHz ADCPs. Vertical lines represent the thresholds of 50 mg/L for the 1200 and 600 and 75 mg/L for the 300 kHz ADCPs.

2.5. Discussion

2.5.1. What is the best practice for obtaining reliable acoustic backscatter profiles where echo intensity is near the acoustic noise floor?

There are two methods for obtaining reliable acoustic backscatter profiles when measured echo intensity is near the acoustic noise floor of an off-the-shelf ADCPs: subtraction of the noise floor from the echo intensity in counts in the conversion to decibels as in Eq. 2.4B [*Dienes*, 1999; *Gostiaux and van Haren*, 2010] or truncation of the profiles when echo intensity reaches the noise floor [*Wood and Teasdale*, 2013; *Topping and Wright*, 2016]. While use of Eq. 2.4B is theoretically more sophisticated and allows for the extension of the profile, it requires some accurate method to predict the noise floor level. Our results suggest that objectively setting the noise floor as the minimum of the instantaneous profile, the minimum over the entire record (all profiles) or

the passive acoustic noise level can all produce acoustic profiles with unrealistic features (i.e. concavity, convexity, positive cross stream *FCB* profiles) which can influence the slope of the profile and hence the in-situ attenuation coefficients. Additionally, it appears that unrealistically large *NL* values are required for the 1200 kHz profile to be extended (using Eq. 2.4B) to remove the concavity that occurs in *FCB* profiles creating a positive slope and negative in-situ attenuation

The alternative to truncating the profile at the noise floor can also be problematic because it requires some objective method for determining when the profile should be truncated. The point where the noise floor is reached varies with sediment concentration and/or particle size. Truncation of profiles is challenging for our environment because the 1200 kHz always reaches the noise floor, and the 600 kHz profiles are near the noise floor at median to high concentrations; also at low concentration acoustic profiles can be influenced by cross-channel concentration inhomogeneity. *Topping and Wright* [2016] suggested that the truncation approach can be used with an additional offset above the noise level, in order to avoid profile concavity as the noise floor is approached. This approach gave accurate attenuation at their field sites, but care still needs to be taken with acoustic profiles that are non-linear or where there is some inhomogeneity in the ensonified volume.

For example, *Gray and Landers* [2014; Figure 18; data in *Landers*, 2012] computed $\alpha_{s,\text{in-situ}}$ for a truncated profile that gave an attenuation coefficient of 0.35 m^2/kg and attenuation of 2.1 dB/m. This is an order of magnitude greater than the theoretical attenuation for the reported concentration of 694 mg/L in *Gray and Landers* [2014; Figure 18], a D_{50} of 25 μm from a log normal GSD, a St. Dev. of 1.0, and a1500 kHz ADCP (computed using Eq. 2.10 & 2.16). The difference between $\alpha_{s,\text{in-situ}}$ and $\alpha_{s,theo}$ is even greater if you use the 185 mg/L given in *Gray and Landers*, 2014; two SSC values are reported for the same site and date due to rapidly changing conditions. In the context of our results, it seems likely that their high value of $\alpha_{s,\text{in-situ}}$ reflects a profile truncated to select the steeper part of a concave profile or the presence of a cross-stream gradient in concentration. Our results highlight the need to verify that the cross-stream variation in concentration and grain size is homogeneous, especially at low concentrations.

The method presented uses Eq. 2.4A for the 300 kHz and for the 600 and 1200 kHz ADCP when above 10 times the noise floor, Eq. 2.4B when below 10 time the noise floor, and additional truncation of the 1200 kHz ADCP since it always reaches the noise floor. Our method of converting *EI* profiles to backscatter prevents both artificially steepened slopes (positive attenuation) and positive slopes (negative attenuation). The additional benefit is that this approach allows for a semi-automated analysis of ADCP data for riverine environments that go from high to low concentrations, as is the case in the Fraser River.

2.5.2. How does in-situ attenuation compare to theoretical attenuation from measured GSDs?

When comparing the theoretical attenuation from the LISST to that of the well constrained GSD from the LS-PSA, a bias appears to exist due to the unaccounted fine portion of the GSD. This influences the estimate of viscous attenuation. Figure 2.1 shows that particle diameters between 0.4 and 4 μm are sensitive to viscous attenuation for 300, 600 and 1200 kHz ADCPs. Though the LISST and LS-PSA GSDs have similar median grain diameter, the unaccounted fine portion of the LISST GSD gives smaller attenuation compared to the LS GSDs. Correcting for this bias is difficult because of the changing GSD over the freshet and from year to year. Figure 2.4 shows that at low flows the fine portion of the GSD is not present (and therefore more unimodal) meaning the bias I observed between the instruments may not be present at low flows. Additionally, the measurements used to derive the apparent bias are limited in number. Comparison of in-situ attenuation from our off-the-shelf ADCPs to theoretical attenuation derived from the LISST shows that values fall close to the line of unity, but are generally less than the in-situ method (Figure 2.8). The unaccounted bias in the LISST theoretical values could partly explain this, but the plate-like shape of clay-sized particles would theoretically decrease viscous attenuation [*Moate and Thorne*, 2009, 2013; *Moore et. al.*, 2013], potentially canceling some of the bias. Additionally, the greater in-situ attenuation may be due to bubbles, biota, or micro-flocs that are not captured in our analysis or in attenuation models derived under more ideal conditions. Our theoretical attenuation calculations assumed a spherical particle model (for ζ_{visc}), while neglecting grain shape and mineralogical models that can be used in our calculations. Using a different grain shape or minerology in our calculations of theoretical attenuation may have some effect on our $\alpha_{s,theo}$ values, but choosing a single grain shape model for the wide range of sizes

in the Fraser is not straightforward. Nevertheless, changing the grain shape model will not account for the order of magnitude difference I observe between $\alpha_{s,\text{in-situ}}$ and $\alpha_{s,theo}$ at low flows. In-situ attenuation is simply less accurate at low concentrations, making comparison of attenuation estimates complicated at low concentrations.

2.5.3. How well does the in-situ attenuation method perform in a system with low concentration?

It is clear from our work that the accuracy of in-situ attenuation, calculated from off-the-shelf ADCPs backscatter profiles, changes with concentration. These inaccuracies at low concentration have been shown in *Topping and Wright* [2016, Figure 20] as well. In the Fraser River, at high concentration in-situ attenuation tends to agree with theoretical attenuation. Below concentrations of ~50 mg/L for the 1200 and 600 kHz instrument and ~75 mg/L for the 300 kHz instrument, in-situ attenuation decreases in accuracy and at very low concentrations (10-50 mg/L) the accuracy is poor. At very low concentrations cross-channel variability can influence the slope of the backscatter profile. The in-beam samples suggest that suspended sediment concentrations and D_{50} are relatively homogeneous in the ensonified volume up to 60 m over the 3 years of our measurement program. Yet at low concentrations a small change in concentration (tens of mg/L) can lead to a substantial cross-stream gradient in measured backscatter and unreliable in-situ attenuation because the change is large relative to the concentration near the ADCPs. This result is perhaps not surprising because weak signals produced at low SSC have relatively larger errors than stronger signals that are produced at higher SSC.

The accuracy of in-situ attenuation can have a direct effect on the computation of concentration from off-the-shelf ADCPs. Re-arranging Equation 2.9 shows that mass concentration can be calculated as:

$$M = \frac{\alpha_{s.in-situ}}{8.686 * \overline{\zeta_{total}}} * 1000 \qquad (2.17)$$

where $\alpha_{s,\text{in-situ}}$ is attenuation converted to the linear form and concentration is in mg/L [*Moore et al.*, 2013]. Using the two well constrained GSDs on June 19, 2014 and July 22, 2014, I find that the estimate of the 600 kHz attenuation coefficient is 0.038 and 0.036 m^2/kg (IB 18), respectively. In-situ attenuation for these two days were 0.043 and

0.033 dB/m, respectively. Using Eq. 2.17 I compute concentrations of 130.2 and 123.5 mg/L, while the measured concentrations were 72 and 40 mg/L. These two days represent concentrations that fall just above and below our estimate of a concentration threshold and show how poor in-situ attenuation estimates can propagate into error in concentration estimates.

Our work has revealed concentration thresholds that provide limits below which in-situ attenuation should not be calculated in the Fraser River. Inversion of the acoustic equation to give mass concentration (Equation 2.17) is particularly sensitive to the parameterization of attenuation. Empirical correlations between fluid corrected backscatter and grain size fractions of suspended sediment concentrations are less sensitive to the sediment attenuation correction and may not even be necessary at low concentrations, especially at lower frequencies [*Hay and Sheng*, 1992; *Gartner*, 2004; *Venditti et. al.* 2016]. However, this limits routine hydroacoustic sediment monitoring with off-the-shelf ADCPs in rivers with large variations in the sediment size and concentration. Our result suggests that the concentration threshold for accurate in-situ attenuation needs to be explored in all rivers where hydroacoustic techniques are being used to measure sediment fluxes. In rivers with large variations in cross-stream SSC or grain-size the in-situ attenuation methods described here are of little value.

2.5.4. Diagnosing when in-situ attenuation methods are apt to work and not work well

There are a number of diagnostic tools that can be used to determine when in-situ attenuation is apt to be a useful metric and when it is not including: 1) Pre-deployment sediment sampling to look for cross-channel concentration and grain size gradients, 2) Checking for cross-channel aberrations in acoustic profiles and 3) comparison of in-situ and theoretical estimates of sediment attenuation. In our study, I found that there was a cross-channel gradient in concentration and grain size at low flows, which I discovered during the deployment. Sampling prior to deployment at a range of flows to check for the cross-channel gradients is an obvious way to avoid problematic sites. I found threshold concentrations where cross-stream gradients were negligible and these thresholds should be identified in the context of what flows are of interest in a sediment monitoring program.

The surest way to diagnose acoustically significant cross-channel gradients in concentration or grain size are to examine the acoustic profiles. If there are abrupt changes in *FCB* with respect to range these may be due to cross-channels gradients. Alternatively, these may be due to interference from the water surface or bed (c.f. *Venditti et al.*, 2016), other backscatterers in the water column (organic matter, bubbles) or other sources of ambient noise. So, comparison of the acoustic profiles with in-beam samples is necessary where aberrations in the profiles are found to determine the exact source of the discontinuity. Then only the portions of the profile that reflects attenuation should be used in calculations. Our Figure 2.9 and the associated calculations of what constitutes an acoustically significant change across the beam range, relative to the absolute measured concentration (see Section 2.4.5) provides a method to assess when problems are apt to arise with in-situ attenuation calculations.

A final diagnostic tool to determine if measured in-situ attenuation values are robust is to compare in-situ attenuation from suitably corrected profiles to theoretical values calculated using a large sample or composite grain size distributions that cover the full range of the GSD. Suitably correcting the acoustic profiles begins with assessing acoustic noise levels. This can be evaluated using either a passive acoustic approach or values from the manufacturer, as I did in our study. If the acoustic profile reaches the noise floor, then our method of extending and truncating prior to the profile reaching the noise floor should be applied. Concavity or convexity of profiles provide ways to assess whether the profiles have been suitably corrected. If care is taken in preventing artificial convex or concave features at the end of the profile, then the computation of in-situ attenuation is only a function of sediment attenuation, concentration, and particle size. Assuming no substantial cross-channel gradients in concentration and grain size, no interference from the bed or water surface and no problems with ambient noise or other acoustical backscatterers in the water column (bubbles or organic matter), in-situ and theoretical attenuation should be nearly identical.

2.6. Conclusions

I have examined the agreement between in-situ sediment attenuation derived from off-the-shelf ADCP profiles and theoretical sediment attenuation calculated from suspended sediment samples obtained within the ADCP beams. To the authors' knowledge, this is the first direct field comparison between in-situ and theoretical

methods applied using samples obtained within the ensonified volume of the acoustic beams. Our observations reveal that when converting acoustic intensity from counts to decibels, acoustic profiles that approach the noise floor need to be corrected for non-linearity before they are truncated in low concentration environments. To accomplish this, care must be taken when defining *NL*. The definition of *NL* can influence the tail of the acoustic profile, which impacts the slope and shape of the backscatter profile with distance from the ADCP. Arbitrary definitions of *NL* or improper truncation can bias the profile and give inaccurate estimates of in-situ sediment attenuation.

In the Fraser River, during very low concentrations, the in-situ sediment attenuation methods are not reliable because gradients in suspended sediment develop across the ensonified volume, creating a non-uniform suspension that is reflected in the acoustic profile. At higher concentrations (>50 mg/L for 1200/600 kHz ADCP and >75 mg/L for the 300 kHz ADCP) the ensonified volume is relatively more homogeneous and acoustic profiles are less sensitive than at low concentrations, creating better agreement between in-situ and theoretical attenuation. Our results highlight the need to explore cross-channel changes in suspended sediment concentration and grain size at a range of flows to ensure homogenous suspensions in the ensonified volume. Application of in-situ sediment attenuation methods in routine monitoring programs without doing so can result in order of magnitude errors in sediment attenuation.

Chapter 3. Acoustically derived annual sediment fluxes in a large alluvial river

Abstract

A two-stage acoustic inversion is developed to predict to sediment fluxes in a 550 m wide river channel using an array of three horizontally mounted acoustic Doppler current profilers (ADCPs). The first stage of the inversion is a calibration between acoustic signals and suspended sediment concentration (SSC) within the ensonified volume of the ADCPs. The second stage is an index-channel average extension used to estimate channel average SSC and flux, similar to index-velocity methods used to estimate channel discharge. I couple acoustic signal values with physical bottle sample SSC measurements within the ensonified volume. Additionally, I measure channel average SSC and flux. Each bottle sample is analyzed for total SSC and for grain size distribution. Twenty-five sampling campaigns were carried-out in the Fraser River at Mission, BC, Canada between 2012 and 2014. Sample concentrations ranged from 20-350 mg/L and were primarily silt to fine sand. Acoustic inversions show strong calibrations between total SSC, sand SSC and silt/clay SSC, while relations between acoustically derived SSC and channel-average SSC provided good correlation, allowing for estimates of continuous SSC and flux on a large river. Acoustic calibration showed both inter-annual and intra-annual variability, but only intra-annual variability could be explained by changes in flow. Flux estimates clearly show hysteretic decoupling of the sedigraph from the hydrograph, while annual flux fell within the same order of magnitude as historical flux from the same location, computed with traditional methods, supporting the robustness of our method.

3.1. Introduction

Knowledge of sediment fluxes in rivers is required for management of navigable waters, reservoir maintenance, understanding sediment budgets that can impact aquatic habitat integrity and prediction of the morphodynamics of rivers and their deltas. Suspended sediment flux can be divided into suspended bed material and washload, the former is responsible for channel morphology while the latter builds floodplains, deltas, and tidal flats. Silt and clay are also important in the prediction of the transport and fate of pollutants that adhere to the suspended particles.

Traditional methods for measuring suspended sediment fluxes rely on measurements of sediment concentration (SSC) in water samples and measured or approximated discharge. Discharge from stage-discharge rating curves or index-velocity acoustic Doppler current profiler (ADCP) relations is obtained relatively easily (both practically and economically) so that a continuous flow record may be reconstructed. However, suspended sediment samples are costly and demanding to obtain, and represent SSC at the time and location of measurement. Furthermore, sedigraphs do not necessarily correlate well with hydrographs, so predicting concentration over a full range of flows is difficult. Traditional methods for combining discharge and sediment concentration measurements, such as sediment rating curves, can produce significant error [*Walling*, 1977], especially when the flow-suspended sediment relation is hysteretic [*McLean et al*. 1999a; *Topping et al*., 2000a, 200b; *Kleinhans et al*., 2007; *Warrick et al*., 2013; *Waters and Crowe Curran*, 2015; *Topping and Wright*, 2016].

Water flow and suspended sediment measurements are possible simultaneously from continuous acoustic monitoring of the water column. Because of the interest in and need for higher resolution sediment data, along with economical acoustic instruments, there has been considerable research on subaqueous acoustic theory, methods, and application to sediment transport [*Flammer* 1962; *Hay*, 1983, 1991; *Lee and Hanes*, 1995; *Thorne and Hanes*, 2002; *Thorne and Hurther*, 2014; *Topping and Wright*, 2016; *Chapter 2*]. The use of an acoustically derived surrogate sediment measure has become an accepted means of approximating suspended sediment concentration and sediment size. Over the last two decades, investigations into the use of acoustics have expanded from, primarily, the oceanographic field to estuarine [*Gartner*, 2004; *Wall et al.*, 2008; *Sassi et al*., 2013b] and riverine environments [*Reichel and Nachtnebel*, 1994; *Topping*

et al., 2007; *Wright et al*., 2010; *Moore et al*. 2013; *Wood and Teasdale*, 2013; *Latosinski et al*., 2014; *Topping and Wright*, 2016; *Venditti et al*., 2016].

In rivers with large drainage basins, source material can vary both inter- and intra-annually, creating variability in grain size distribution (GSD) and composition of suspended sediment. The advantage of increased spatial and temporal resolution that comes with using acoustic methods is coupled to the disadvantage that acoustic signals (and therefore calibrations) are sensitive to sediment mineralogy and GSD, in addition to concentration. This problem can be exacerbated in wide river channels because there are often cross-channel variations in sediment concentration, size and composition.

To use acoustically derived sediment properties (concentration, size specific concentration, or particle size) at temporal scales appropriate for larger scale questions, such as fate and transport of contaminants, sediment budgets and large-scale research investigations, the annual stability and possible bias of the current acoustic methods need to be examined. Though the literature is ripe with data sets that investigate theory, methods, and application at spatial resolutions typically at the laboratory scale (meters) [*Crawford and Hay*, 1993; *Thorne and Hanes*, 2002; *Moate and Thorne*, 2009, 2011, 2013] and at temporal resolution ranging from seconds to hours, to event-based (days to weeks) [*Sassi et al*., 2012; *Moore et al*., 2013], very little work has examined hydroacoustics on large rivers with temporal scales ranging from months to several years.

Venditti et al. [2016] developed a purely empirical, two-stage inversion method for use in wide river channels with cross-stream variability. The first stage involved calibration of a horizontally mounted ADCP using samples obtained within the ensonified portion of the water column (~60 m of a 550 m wide channel). The second stage was to develop a correlation between the ADCP-derived sediment concentrations and the measured channel-averaged concentration. In this respect, the method is similar to the index-velocity methods used to estimate channel discharge in large rivers. *Venditti et al.* [2016] found that ADCP calibrations are robust and conform with sonar theory so long as suspended sediment size distribution remains relatively consistent. The purely empirical calibrations remained subject to variations in the size of suspended sediments. They found that calibrations changed seasonally, shifting between pre-peak to post-annual peak discharge. Though their work suggested that these changes were due to changing

GSD characteristics, the relatively small number of observations prohibited a definitive conclusion. Nevertheless, *Venditti et al.* [2016] showed that the index correlation cancels any calibration bias and permits monitoring of size-classified suspended sediment in absence of detailed information of sediment grain-size distribution. *Venditti et al.* [2016] also found that the combination of acoustic frequency (~300 kHz), sediment size and concentration at their field site in the Fraser River at Mission, British Columbia, produced negligible sediment attenuation below concentrations of ~150 mg/L. As a result, there was no relation between sediment attenuation and silt-clay concentrations; a relation commonly exploited in empirically-based, size-specific sediment monitoring programs [*Wright et al.*, 2010; *Moore et al*., 2013; *Topping and Wright*, 2016]. *Venditti et al.* [2016] suggested that a wider range of acoustic frequencies should be explored to see if they are more sensitive to concentration and sediment size.

Here, I further explore the two-stage method developed by *Venditti et al.* [2016]. I test their inferences using a more comprehensive set of observations that spans three years, using an array of three different frequency ADCPs. This allows for a more temporally resolute investigation. I expand upon the method developed by *Venditti et al.* [2016] by estimating both total and size-partitioned suspended sediment flux at temporal scales that range from hours to years. Size-partitioned sediment flux is estimated by calibrating characteristics of the acoustic signal to specific size classes to which the signal should theoretically be responsive. I: (1) examine the accuracy, precision, and bias of acoustic calibrations; (2) compare annual acoustically derived flux measurements to annual sediment fluxes from past observations; and (3) examine whether the acoustically derived flux can successfully track the sedigraph independent of discharge.

3.2. Acoustic sediment inversion

The use of hydroacoustic instruments to measure suspended sediment is based on a theoretical relation between suspended sediment concentration and measured acoustic backscatter. The sonar equation as presented by *Urick* [1975] is:

$$RL = SL - 2TL + TS \tag{3.1}$$

where *RL* is the reverberation level of the aqueous scatterers, *SL* is source signal strength, *TL* is the two-way transmission loss and *TS* is the target signal strength. *TS*

can be decomposed into two components, one attributed to the instrument, TS_{inst}, and one to the suspended sediment, TS_{sed}:

$$TS = \overbrace{10log_{10}\left(\frac{3\tau c}{8}\left(\frac{0.96}{ka_t}\right)^2\right)}^{TS_{inst}} + \overbrace{10log_{10}\left(f^2\frac{M}{D_g\rho_s}\right)}^{TS_{sed}} \quad (3.2)$$

where M is the sediment mass concentration, c is celerity of sound in water, τ is the acoustic transmit pulse, k is the acoustic wavenumber, a_t is the transducer radius, f is the form function which is the backscattering parameter that is a function of the GSD and acoustic wavelength, D_g is the geometric mean grain diameter, and ρ_s is the sediment density. All the parameters in TS_{inst} are returned to the user by the instrument and can therefore be accounted for, removing some of the seasonal variability in the signal caused by temperature and therefore celerity of sound [*Topping et al*., 2015; *Topping and Wright*, 2016]. While target strength is a function of the ratio of acoustic wavelength to particle diameter, transmission losses are caused by acoustic spreading and attenuation. Transmission losses can be defined as:

$$2TL = 20log_{10}(r) + 2\alpha_f r + 2\alpha_s r \quad (3.3)$$

where α_f is the fluid attenuation, α_s is the attenuation from sediment in suspension, and r is the distance (range) from the transducer. α_f is a function of temperature and instrument frequency (assuming salinity and pressure variation are negligible in shallow rivers). I use the *Francois and Garrison* [1982] model, which is well defined for our conditions.

Commercially available ADCPs report a measure of backscatter as the echo intensity (*EI*) in counts, which is converted to measured backscatter as:

$$I_{db} = \mathrm{f(x)} = \begin{cases} 10log_{10}(10^{\frac{k_c EI}{10}} - 10^{\frac{k_c E_{noise}}{10}}), & k_c EI < 10 + k_c E_{noise} \quad (3.4a) \\ k_c(EI - E_{noise}), & k_c EI \geq 10 + k_c E_{noise} \quad (3.4b) \end{cases}$$

where I_{db} is backscatter in decibels, E_{noise} is the echo intensity noise floor in counts, and k_c is defined by the temperature of the instrument [*Moore et al*., 2012; *Chapter 2*]. The application of Equation 3.4a was first described by *Gostiaux and van Haren* [2010] as a way to subtract out the E_{noise} in linear space to asymptotically extend the profile in logarithmic space. They show that Equation 3.4a should be used when $k_c(EI\text{-}E_{noise})$ is

less than 10. *Chapter 2* has shown that, though this is an appropriate method, when defining the noise level care must be taken to prevent artificially distorting the profile and introducing convexity or concavity, when *EI* approaches E_{noise} in Equation 3.4a. Here I use the method defined in *Chapter 2* which uses two definitions of E_{noise}, an absolute E_{noise} and an effective E_{noise}. The absolute E_{noise} can be defined by the minimum over a year or by passive acoustics (best for short data records), while the effective E_{noise} is defined as the minimum of the profile (E_{noise} in Eq. 3.4). This method allows for a piecewise equation, where difference between the effective E_{noise} and the absolute E_{noise} determines whether to use Equation 3.4a or 3.4b, allowing a semi-autonomous analysis. 'Passive acoustics' refers to the instrument in listening mode when it captures ambient noise only.

When utilizing commercially available acoustic instruments to invert acoustic backscatter to an estimated sediment concentration, Equation 3.1 is rearranged to address the transmission losses (*TL*). To account for water attenuation and spreading losses (Eq. 3.3), backscatter intensity is corrected by:

$$FCB = I_{db} + 20\,log_{10}(r) + 2\alpha_f r + TS_{inst} \tag{3.5}$$

where *FCB* is fluid corrected backscatter, which accounts only for fluid attenuation. In flows with high sediment concentrations, a further correction for two-way transmission losses is required and is accomplished by calculating the sediment corrected backscatter. What constitutes a high sediment concentration in our circumstance is explored herein. I employ the in-situ approach that uses the slope of the relation between *FCB* and range as an estimate of sediment attenuation in decibels per meter [*Moate and Thorne* 2009; *Wright et al*., 2010; *Chapter 2*]:

$$\alpha_s = -0.5 S_{FCB,r} \tag{3.6}$$

where $S_{FCB,r}$ is the slope of the linear regression between *FCB* and *r*.

The sediment corrected backscatter is then:

$$SCB = FCB + 2r\alpha_s = 10log_{10}\left(f^2 \frac{M}{D_g \rho_s}\right) \tag{3.7}$$

Sediment corrected backscatter accounts for both fluid attenuation and sediment attenuation. The in-situ method relies on the assumption that concentration and particle size are homogenous within the ensonified volume. In *Chapter 2* I explore this assumption and show how, in low concentrations (<50 mg/L) the use of Equation 3.6 has limitations due to acoustic fluctuations caused by a relatively inhomogeneous ensonified volume. At higher flows, when concentrations are greater, the in-situ method was shown to produce robust attenuation measurements. The threshold is dependent on concentration and grain size, relative to acoustic frequency and it is therefore site specific. Acoustically derived sediment concentration (SSC_{ADCP}) can then be estimated by:

$$log_{10}(SSC_{ADCP}) = \mathrm{K1}(SCB) + K_t \quad (3.8)$$

where K_t is an instrument and target constant that incorporates particle size, source level, ensonified volume, target strength, and the mass of the suspended material. The constant K1 should be theoretically 0.1 [*Thevenot et al.*, 1992], but has been shown to vary in practice [*Venditti et al.*, 2016]. These factors make the parameter site specific [*Thevenot et al*., 1992; *Gartner*, 2004; *Wright et al*., 2010]. Amongst them, independent variation of grain size at all temporal scales causes changes in K_t, complicating the determination of suspended sediment concentration.

3.3. Methods

3.3.1. Field Site

Field observations were made on the Fraser River, at Mission, BC (Water Survey of Canada [WSC] station no. 08MH024), approximately 85 km from the river mouth at the Strait of Georgia (Figure 3.1a). Here, the Fraser flows in a single ~550 m wide prismatic channel carrying runoff from the 228,000 km^2 drainage basin. This provides an ideal location to measure the flow and sediment influx to the lowermost reach of the river. The runoff pattern is dominated annually by the spring snowmelt in May-June initiating a freshet in late May, June and early July. The freshet recedes in July, August and September. Flow at Mission is influenced by a tidal signal during low flow periods, creating a backwater effect, but the saline wedge does not reach beyond New

Westminster, BC. The mean annual river flow at Mission from 1983 to 2013 was 3183 m^3/s and the mean annual flood was 9534 m^3/s [*Chapter 2*].

Using data obtained by the WSC between 1965 and 1986, *McLean at al*. [1999] found that, on average, 17 Mt a^{-1} of sediment moved past Mission, BC. About one third, $6.1x10^6$ Mt a^{-1}, is suspended sand and half of that (3.0 Mt a^{-1}), is sand finer than 0.177 mm [*McLean et al.*, 1999] that can be assigned to washload (typically suspended material not present in the bed material in quantities exceeding ~10% [*Church,* 2006]). Material coarser than 0.177 mm, defined as suspended bed material, is morphologically significant in the lower Fraser River because it forms the bed and lower banks of the river [*McLean et al.*, 1999].

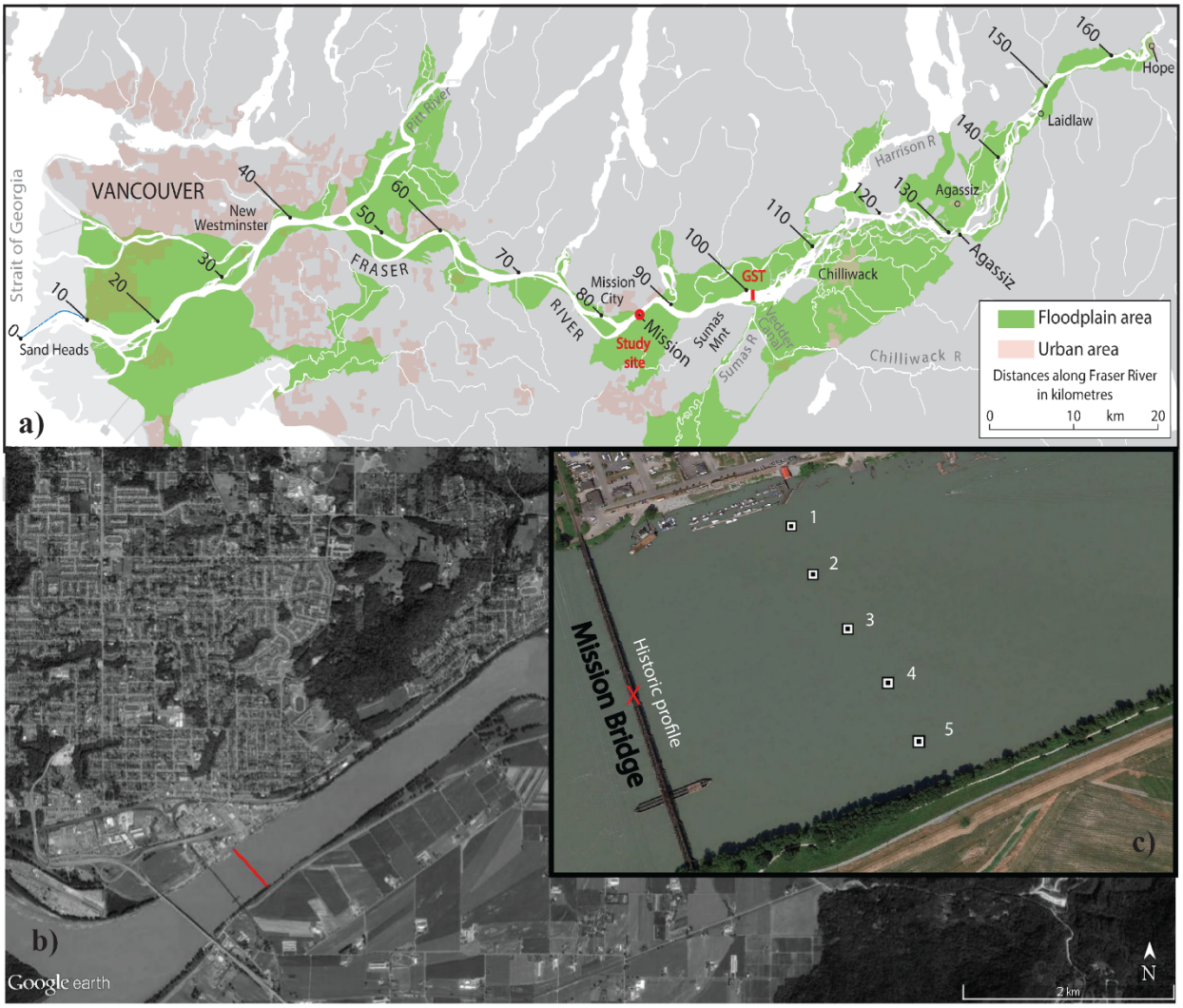

Figure 3.1. a) Map of the Lower Fraser River and Delta, including the Mission, BC field site and the gravel-sand transition (GST). b) Google Earth imagery [2017] of the Fraser River at Mission, BC, Canada. The red line on the bottom panel shows the cross-section used for both moving-boat discharge measurements and horizontal ADCP measurements. c) Google Earth imagery of the Mission Bridge. The "X" shows the location of profiles collected by the Water Survey of Canada from 1966 to 1986 and summarized by *McLean et al.* [1999]. Symbols 1-5 show the location of profiles used in cross-sectional concentration and flux measurements.

3.3.2. Acoustic Doppler current profiler setup and sediment sampling

Three horizontally oriented acoustic Doppler current profilers (ChannelMaster™ H-ADCPs, Teledyne RDI, USA) were mounted on the Mission Harbour Authority dock just upstream of the Mission railway bridge (Figure 3.1b). The three ADCPs were

mounted in a horizontal array, separated by ~77 cm. Power for the instruments was AC power run through an AC/DC converter and a voltage regulator to ensure a constant power between 12 and 13 volts. The instruments have acoustic frequencies of 307, 614 and 1218 kHz, nominally 300, 600 and 1200 kHz. Each ADCP has two beams with a 20^{o} angle from center. One-way beam spreading is 1.5^{o} for the 600 and 1200 kHz ADCPs and 2.2^{o} for the 300 kHz ADCP. Care was taken during installation to reduce the pitch and tilt of the instruments to within ±0.1 degrees from zero. The ADCPs were set to collect data over one minute with a one-minute rest before the next ADCP started collection, creating a 6-minute interval for all ADCPs. Ensemble averaging was done over 100 pings per minute. Instruments were set in low-bandwidth mode to allow for high resolution and minimal noise at a cost of maximum range. The ADCPs collect data in 128 bins across the channel. The spacing of the bins and the distance across the channel over which measurements are obtained depends on the instrument. The 300 kHz instrument has 2 m bins and a 2 m blanking distance, so it nominally measures 258 m across the channel. The 600 kHz instrument has 0.5 m bins and a blanking distance of 2 m, so it measures 66 m across the channel. The 1200 kHz instrument has 0.25 m bins and a blanking distance of 2 m, so it measures 34 m across the channel. The practical ranges of the instruments, over which reliable backscatter can be calculated, are somewhat different and depend on the noise floor for the 1200 and 600 kHz ADCPs and where the 300 kHz ADCP signal hits either the riverbed or river surface during low flows (~60 m) [*Chapter 2*]. In my analysis, I used the downstream beam for all three ADCPs. I explored the use of the other beam, but it had a similar response. The areas of the channel cross-section ensonified by the ADCPs are shown in Figure 3.2. Acoustic backscatter data were recorded from 2012 to 2014, with several interruptions when data were not collected due power loss or instrument cleaning.

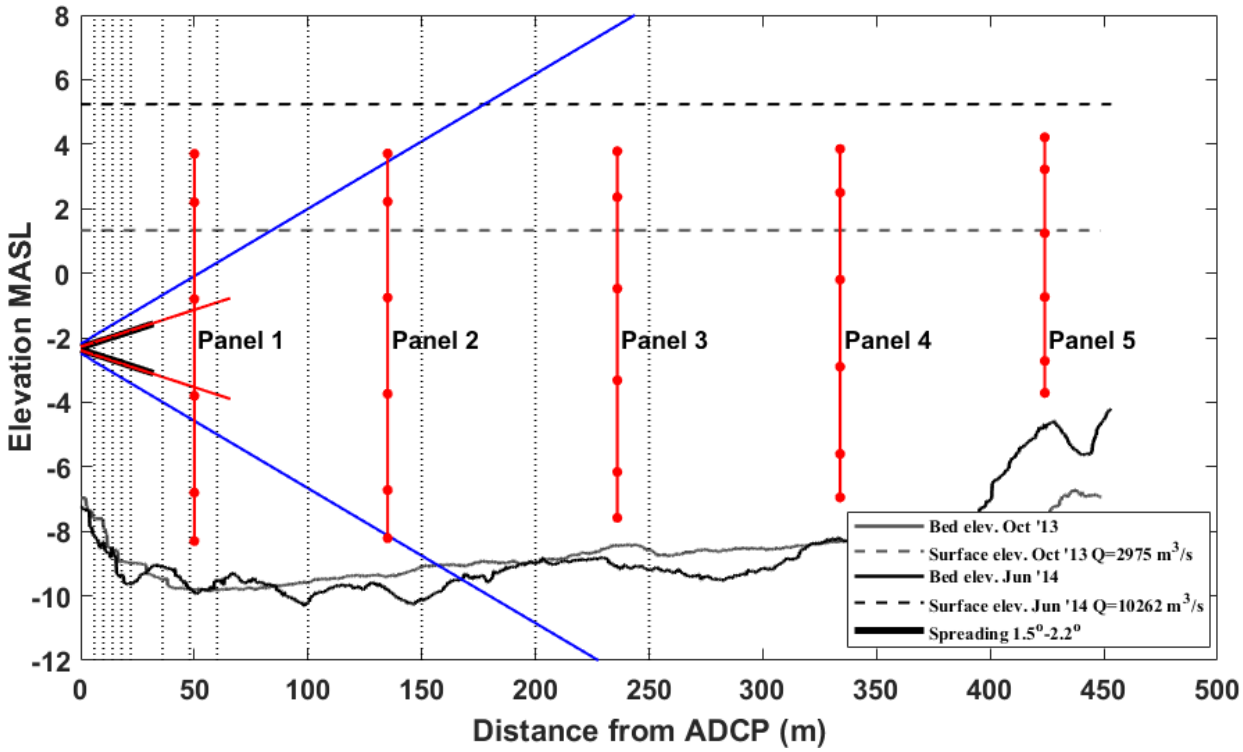

Figure 3.2. Acoustic beams as a function of cross section width and sediment sampling locations. Vertical dashed lines represent the distances from the ADCPs for 'in-beam' samples taken throughout years 2012-2014. Sediment sampling profile locations (or panels) are shown in red with points indicating the sampling height at high flow depths.

Sediment sampling campaigns were undertaken to calibrate and evaluate acoustically derived surrogate suspended sediment concentrations. The suspended sediment samplings consisted of six campaigns in 2012, eight in 2013 and eleven in 2014 and were designed to capture a wide variety of flows through the annual Fraser River freshet hydrograph.

A 90 kg (200 pound) USGS P-63 sampler, deployed from a vessel using a motorized USGS designed E-reel, was used to collect point-integrated, isokinetic suspended sediment samples. A series of 'in-beam' samples was taken at calculated distances and depths across the channel to align with the ADCP beams ($SSC_{IB,meas}$). The locations ranged from 6 to 250 m from the ADCPs and were selected so that there were five roughly equally-spaced samples in each of the three acoustic beams. In addition to the in-beam samples, I collected vertical profiles (panels) of suspended sediment samples ($SSC_{chan,meas}$) at five equally spaced locations across the channel. These samples allowed us to estimate the total sediment concentration and flux in the

channel, which must be correlated with the ADCP derived sediment concentrations to predict continuous suspended sediment flux in the channel. This step was necessary because the ADCP beams did not reach across the entire 550 m wide channel. At each of the 5 verticals, point samples were collected at 6 depths: 0.1*h*, 0.2*h*, 0.4*h*, 0.6*h,* 0.8*h* and 0.9*h*, where *h* is flow depth.

Each of the suspended sediment samples was processed in the Simon Fraser University River Dynamics Lab using a LISST-100 (Sequoia Scientific, USA) instrument that uses laser diffraction to calculate the fractional grain size distribution (GSD). Sediment mass concentration was also obtained using the traditional filter (0.45 μm) method after the sample passed through the LISST-100. Grain size distributions were segregated into total SSC (full GSD), sand (>62 microns) and silt/clay (<62 microns) as well as suspended bed material (>180 microns), washload (<180 microns).

A 600 kHz Workhorse Rio Grande ADCP (downward looking) was also deployed from the vessel to measure flow velocity, depth, and temperature simultaneously with the collection of suspended sediment profiles, allowing for a flux calculation at each profile. Velocity for each measured flux was obtained by taking the mean velocity over the same period as that in which the sample was collected at the bin nearest to the sampler. The ADCP was offset from the sampler by approximately six meters in the horizontal. In a large river, such as the Fraser, this offset is assumed negligible when computing sediment flux.

3.3.3. Acoustic Doppler data filtering

In general, and especially during low flows, raw data in counts are noisy due to ambient noise in relatively quiescent water. Prior to being converted to acoustic intensity in decibels, I_{db}, data were filtered with single spectral analysis (SSA: Appendix 3.1), which is similar to principal component analysis, but in the time domain [*Vautard and Ghil*, 1989; *Vautard et. al.*, 1992; *Plaut and Vautard*, 1993]. The SSA method is a version developed by *Vautard et. al.* [1992] and modified by *Schoellhamer* [2001] that accounts for missing data. For our analysis, I use a maximum lag of 120 (12 hr) to compute the Toeplitz matrix and five principal components to deconstruct the signal. To reconstruct our time-series I use the first four principal components, which account for approximately

94% of the variance for bins within the applied range of the ADCPs, and retain only the dominant frequencies of the signal, while discarding some of the higher-frequency noise.

3.3.4. Discharge analysis

In order to calculate continuous sediment discharge in the channel I require a continuous record of water discharge. I developed an index-velocity rating curve using the ADCP records. Figure 3.3a shows the relation between the mean channel velocity and the index-velocity measured by the ADCPs. The mean channel velocity was provided by discharge measurements made by the WSC. The index-velocity is the corresponding downstream velocity at the ADCP during the discharge measurement.

To determine the best index-velocity to use, I examined the relation between measured mean channel velocity and the ADCP index-velocity as a mean over the entire ensonified volume, as an incremental cumulative average both increasing and decreasing away from the ADCP, and as a cross-correlation between the index and channel mean. For the cross-correlation analysis I use a moving spatial average where I incrementally increased the window size from one bin to 50 bins, thereby changing the index window in width and location. All analyses were optimized for the best sum of squared residuals (SSR). Results showed that the optimal SSR was found using velocity (U_{adcp}) calculated from cells that range from 15.6-17.2 m, 55.7-58.9 m, and 66.9-73.3 m away from the ADCPs for the 1200, 600, and 300 kHz frequencies, respectively.

Figure 3.3b shows the relation between the channel cross-sectional area and stage (relative water level at the ADCP; h_{adcp}). The stage is measured by the ADCPs and the channel cross-sectional area is determined from discharge measurements. The index-velocity and stage curves depicted in Figure 3.3 are distinct for each ADCP because each ADCP ensonifies a different volume of the channel cross-section (Figure 3.2). Using an index-velocity and stage measured by an ADCP, the mean channel velocity and cross-sectional area can be predicted from relations given in Table 3.1.

Table 3.1. Index-velocity and stage-area relations from Figure 3.3.

Frequency	Index-velocity	Stage-area
1200 kHz	$U=1.64U_{adcp}+0.27$	$A=487.3h_{adcp}+3027$
600 kHz	$U=1.08U_{adcp}+0.21$	$A=450.2h_{adcp}+3568$
*300 kHz	$U=0.95U_{adcp}+0.20$	$A=503.9h_{adcp}+3204$

*Used in the computation of discharge for all flux calculations.

Channel discharge is the product of predicted mean channel velocity and area. Figure 3.3c shows the measured discharge compared to predicted discharge from all three ADCPS. In our application, I use discharge values from the 300 kHz instrument (Figure 3.3d) because of the good fit between predicted and measured discharge.

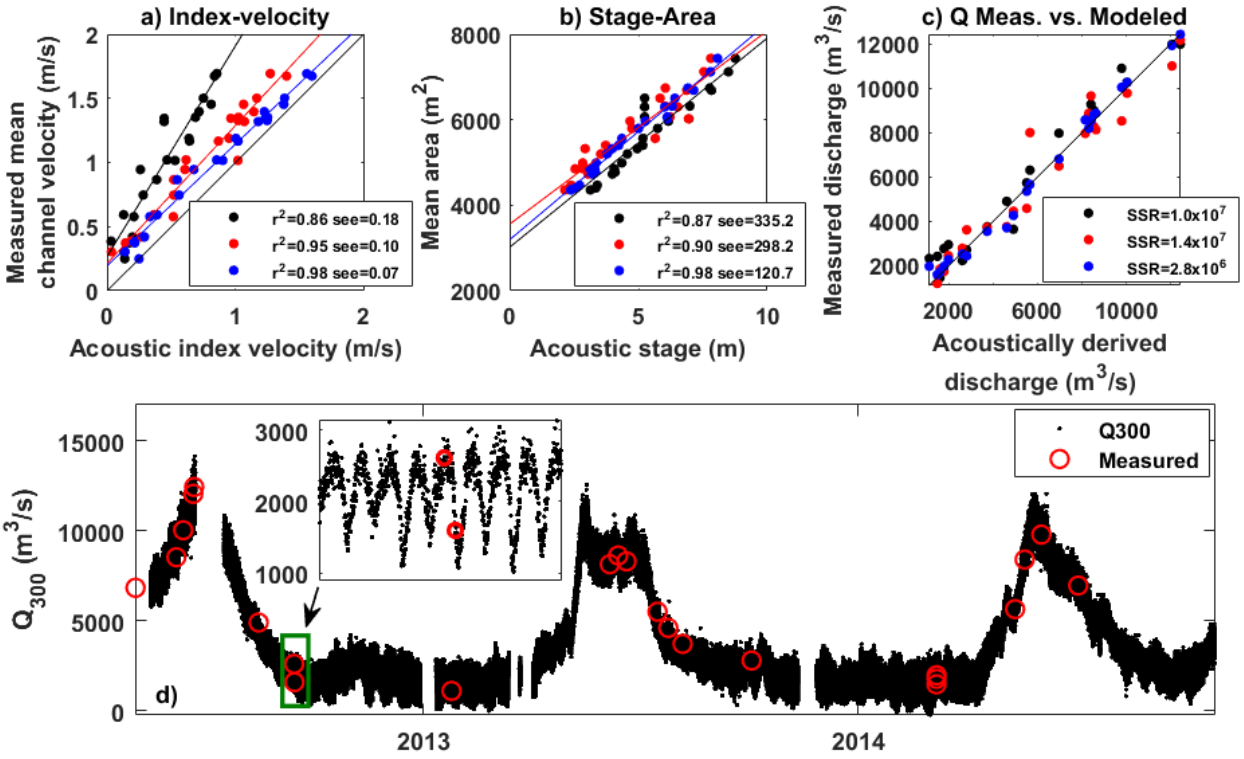

Figure 3.3. ADCP index-velocity discharge relations include (a) Index-velocity, (b) stage-area, and (c) measured versus predicted discharge for 1200 (black), 600 (red), and 300 (blue) kHz ADCPs. (d) Time-series of acoustically derived discharge from the 300 kHz ADCP. The sum of squared residuals (SSR) is based on the line of unity.

3.3.5. Measured and acoustically derived sediment flux

Measured sediment flux (Q_s) in the channel (from the bottle sampling) is calculated using the product of channel average SSC ($\langle SSC_{chan,meas} \rangle$) and ADCP derived discharge ($\langle Q_{chan,,ADCP} \rangle$), which follows the method described in *Attard et al.*, [2014]. First, I calculate measured channel-average SSC, integrated over the cross-section:

$$\langle SSC_{chan,meas} \rangle = \frac{1}{b} \sum_{1}^{5} b_i \sum SSC_i(z) * dz \quad (3.9)$$

where *SSC* is the concentration at depth *z*, *b* is panel width for each profile (i.e. ~ 1/5 of the channel width) and the subscript *i* indicates a single channel panel. Channel-average flux is then computed as:

$$Q_{s,meas,Q-ADCP} = \langle Q_{chan,ADCP} \rangle * \langle SSC_{chan,meas} \rangle \quad (3.10)$$

To calculate acoustically derived suspended sediment flux a linear relation between the suspended sediment concentrations estimated from the calibrations (SSC_{ADCP}) and the measured channel-averaged suspended sediment concentration ($<SSC_{chan,meas}>$) was developed to obtain acoustically derived mean channel SSC ($<SSC_{chan,ADCP}>$). From this relation, I compute acoustically derived suspended sediment flux as:

$$Q_{s,ADCP} = \langle Q_{chan,ADCP} \rangle * \langle SSC_{chan,ADCP} \rangle \quad (3.11)$$

where $Q_{chan,ADCP}$ is the discharge from the 300 kHz ADCP.

3.4. Results

3.4.1. Measured sediment concentration and particle size distribution

To quantify the stability of the acoustic inversion it is critical to have physical measurements collocated with acoustic signal measurements. To this end, I report physical samples collected over the 2012-2014 campaigns. Figure 3.4 shows the GSD characteristics as a function of range and discharge (colorplot). Figure 3.4a shows concentration over the full sample extent for all samples collected in the Fraser River cross-section. The range of SSC values is relatively steady (mean of 90 one standard deviation (±) of 57 mg/L) out to 100 m when concentrations are >75 mg/L, which meets the assumption underlying Equation 3.6, especially considering that the applied maximum range for all ADCPs was 60 m. Here I define ‘steady’ as falling within a range of 0.5x to 2x (±3 dB) the value of the point closest to the ADCPs. *Chapter 2* showed that at low concentrations (SSC< 50 mg/L) the assumption of a homogenous ensonified volume does not hold as relatively small fluctuations in SSC or grain-size can change

the acoustic response by ±3dB and influence the slope of the acoustic profile, and therefore sediment attenuation (Eq. 3.6). To explore this phenomenon, I used in-beam samples to examine the spatial and temporal distribution of SSC and geometric mean particle size (D_g). Figure 3.4b shows that D_g for each sample collected, by range, is relatively uniform out to 100 m. Additionally, during low flow D_g becomes coarser than the mean D_g (29 ± 6.9 μm), likely due to material being composed of locally suspended bed material. Figure 3.4c shows that the standard deviation of the GSD (σ_g) increases with flow, but does not change much as a function of range (mean σ_g = 2.6 ± 0.33). SSC and GSD characteristics show that, with respect to range, two-fold changes do not occur within the first 60 m (the limited range of the acoustic analysis).

The majority of in-beam samples have a log-normal distribution of grain size (Figure 3.4d). During low flow, GSDs are generally coarser, while at higher flows GSDs become finer and broader. At high flow, sediment is sourced locally from the sand bed and from washload supplied from the drainage basin. At low flows, sediment is derived locally from the sand bed and is therefore somewhat coarser. In Figure 3.4a and 3.4c there are a series of relatively high values that stem from one sampling day during the "first flush" of silt and clay from the drainage basin which occurs April 25, 2014 (Q = 5175 m^3/s). The elevated particle size values seen in Figure 3.4b are from one of the low flow measurements (Q=1300 m^3/s) when coarser material dominates the suspended bed material and there is little silt or clay sediment supplied from the drainage basin.

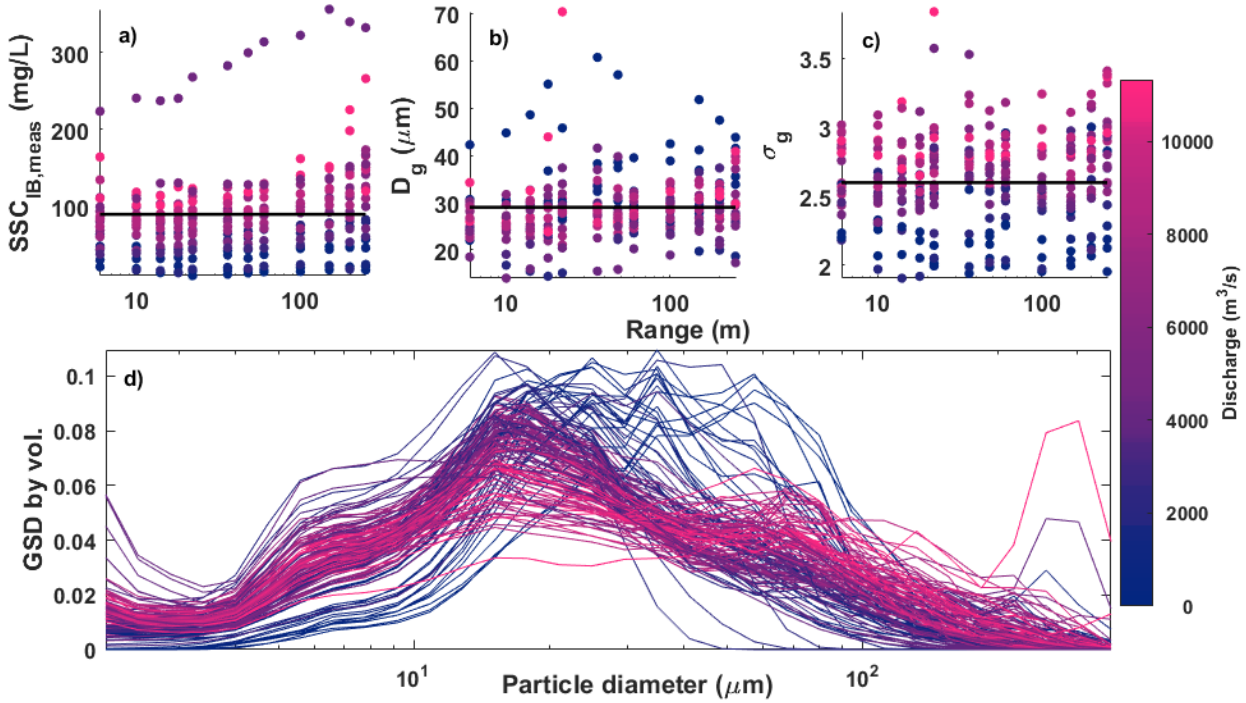

Figure 3.4. (a) Spatial distribution of total suspended sediment concentration, (b) geometric mean particle size, and (c) GSD standard deviation from in-beam samples collected in 2012-2014 as a function of acoustically measured flow. (d) GSDs from the LISST bottle samples as a function of acoustically measured discharge. Every other sample is shown in d to make the figure readable. The horizontal lines in a-c show the respective mean for each parameter.

3.5. Acoustic calibrations and channel-index relations

3.5.1. Acoustic calibrations

I calibrate total suspended sediment (TSS) to *FCB*, sand and suspended bed material (SBM) concentrations to *SCB*, and silt/clay and washload SSC to in-situ sediment attenuation (α_s). The choice to relate the various GSD portions to particular acoustic parameters follows the theoretical basis that coarse sediment should relate most strongly to backscatter while finer sediment should relate to sediment attenuation [*Hanes,2002*a, b; *Topping et al.,* 2007; *Wright et al.,* 2010], and TSS should relate to *FCB*, but only if sediment attenuation is negligible [*Gartner*, 2004]. I do not know *a priori* the threshold where attenuation is negligible, so none is applied in the TSS-*FCB* relation. Because these are formal calibrations I correct regressions using the reduced major axis method of *Mark and Church* [1977].

All samples were used for calibration. *Haught et al.* [2014] used 2012 data for calibration and used 2013 data for validation. They showed that 2012 calibrations predicted 2013 data well. The comparison revealed a near 1:1 relation. Therefore, we used all available data in the calibrations to improve their statistical strength. The collection of validation data is needed and should follow this work.

It is important to recognize that there is error associated with suspended sediment samplers such as the USGS P-63, used to obtain the samples reported in Chapter 2. Working at my field site in the Fraser River at Mission, BC, Canada, *Gitto et al.* [2017] found that variability around the mean concentration increases from 3 to 33% as a function of distance above the bed, where increased error was associated with sampling near the bed. Though this variability is low, particularly for samples taken in-beam and higher in the water column, *Gitto et al.* [2017] did show that the likelihood of collecting a sample not representative of the mean, within the timeframe of my sampling, is high. It also suggests that error may be highest for at-a-point samples collected near the bed, which are then used in computation of channel average SSC and in the Index-extension (see below). This may contribute to the variability in the acoustic calibrations.

Table 3.2 shows the statistical results of the calibrations for each ADCP used in this study. The 600 kHz ADCP has the strongest coefficient of determination (R^2) among all relations, followed by the 1200 then 300 kHz ADCPs. All relations are significant at the 95% confidence level. Calibrations all give coefficient values near the theoretical value of 0.1 (see Equation 3.8), and generally increase with decreasing frequency.

The TSS-*FCB* and Sand-*SCB* SSC R^2 values are strong (Figure 3.5 and Table 3.2). The relations between SBM and *SCB* show more scatter, leading to poorer coefficients of determination for all frequencies (Table 3.2). The calibrations between washload and silt/clay SSC and attenuation (Figure 3.5) have poor R^2 values for the 1200 and 300 kHz, but a strong R^2 value for the 600 kHz. High points in the TSS-*FCB* relation and low points in the Sand-*SCB* relation were removed to improve R^2 values. The TSS-*FCB* outliers occur because there is no sediment attenuation correction applied to *FCB*. Once *FCB* was corrected using the in-situ attenuation, these data points aligned with the trend in the data (as shown in the Sand-*SCB* relation). The outliers in the Sand-*SCB* correlation are a result of very low sand SSC (<5 mg/L). Calibrations do show a visual distinction with regards to the fraction of fine material in the GSD. For the TSS-

FCB calibrations, samples dominated by silt/clay material tend to fall above the line of unity while the coarser samples fall below. For the Sand-*SCB* and SBM-*SCB* calibrations this trend is reversed, in that the coarser samples tend to fall above the line of unity.

Table 3.2 Calibrations based on Equation 8 used to derive suspended sediment concentrations.

	1200 kHz								
	Model	**Slope bounds	R^2	p-value	BCF	SEE	sum of residuals		
							2012	2013	2014
TSS-FCB	Log(TSS)=FCB*0.0541+1.01	0.0463,0.0619	0.69	$3.9x10^{-5}$	1.03	0.10	0.49	-0.26	-0.23
Sand-SCB	Log(Sand)=SCB*0.0788-0.121	0.0653,0.0923	0.53	$5.9x10^{-4}$	1.09	0.18	0.16	-0.30	0.14
SBM-SCB	Log(SBM)=SCB*0.0976-0.694	0.0760,0.119	0.22	$5.2x10^{-2}$	1.23	0.30	-0.14	-0.24	0.38
Washload-α_s	Wash=Atten*887-23.9	722,1050	0.34	$5.7x10^{-3}$	-	39	-27	-140	170
Silt/clay- α_s	Silt/clay=Atten*830-27.1	682,978	0.39	$2.3x10^{-3}$	-	35	-32	-120	150
	600 kHz								
	Model	**Slope bounds	R^2	p-value	BCF	SEE	sum of residuals		
							2012	2013	2014
TSS-FCB	Log(TSS)=FCB*0.0724+0.0760	0.0650,0.0798	0.77	$1.6x10^{-8}$	1.04	0.13	0.63	-0.18	-0.44
Sand-SCB	Log(Sand)=SCB*0.0756-0.684	0.0679,0.0832	0.78	$2.1x10^{-8}$	1.05	0.14	0.09	0.11	-0.20
SBM-SCB	Log(SBM)=SCB*0.0884-1.26	0.0746,0.102	0.48	$2.3x10^{-4}$	1.17	0.25	-0.33	0.38	-0.050
Washload-α_s	Wash=Atten*1290-8.65	1190,1390	0.88	$1.2x10^{-11}$	-	16	45.57	-15	-31
Silt/clay- α_s	Silt/clay=Atten*1210-12.8	1130,1290	0.90	$2.8x10^{-12}$	-	14	41.43	-13	-29
	300 kHz								
	Model	**Slope bounds	R^2	p-value	BCF	SEE	sum of residuals		
							2012	2013	2014
TSS-FCB	Log(TSS)=FCB*0.0828-1.52	0.0705,0.0950	0.52	$7.3x10^{-5}$	1.08	0.19	0.21	-0.080	-0.13
Sand-SCB	Log(Sand)=SCB*0.0962-2.75	0.0810,0.111	0.45	$3.3x10^{-4}$	1.13	0.22	-0.35	0.31	0.030
SBM-SCB	Log(SBM)=SCB*0.111-3.67	0.0920,0.133	0.27	$9.9x10^{-3}$	1.25	0.30	-0.74	0.55	0.19
Washload-α_s	Wash=Atten*2020-0.682	1690,2350	0.39	$9.3x10^{-4}$	-	35	0.76	14	-15
Silt/clay- α_s	Silt/clay=Atten*1880-5.29	1580,1870	0.40	$6.5x10^{-4}$	-	32	-0.29	17	-16

p-value significance based on α = 0.05. BCF is the bias correction factor (Newman, 1993). see = standard error of estimate. ** The 95% confidence range of the slope

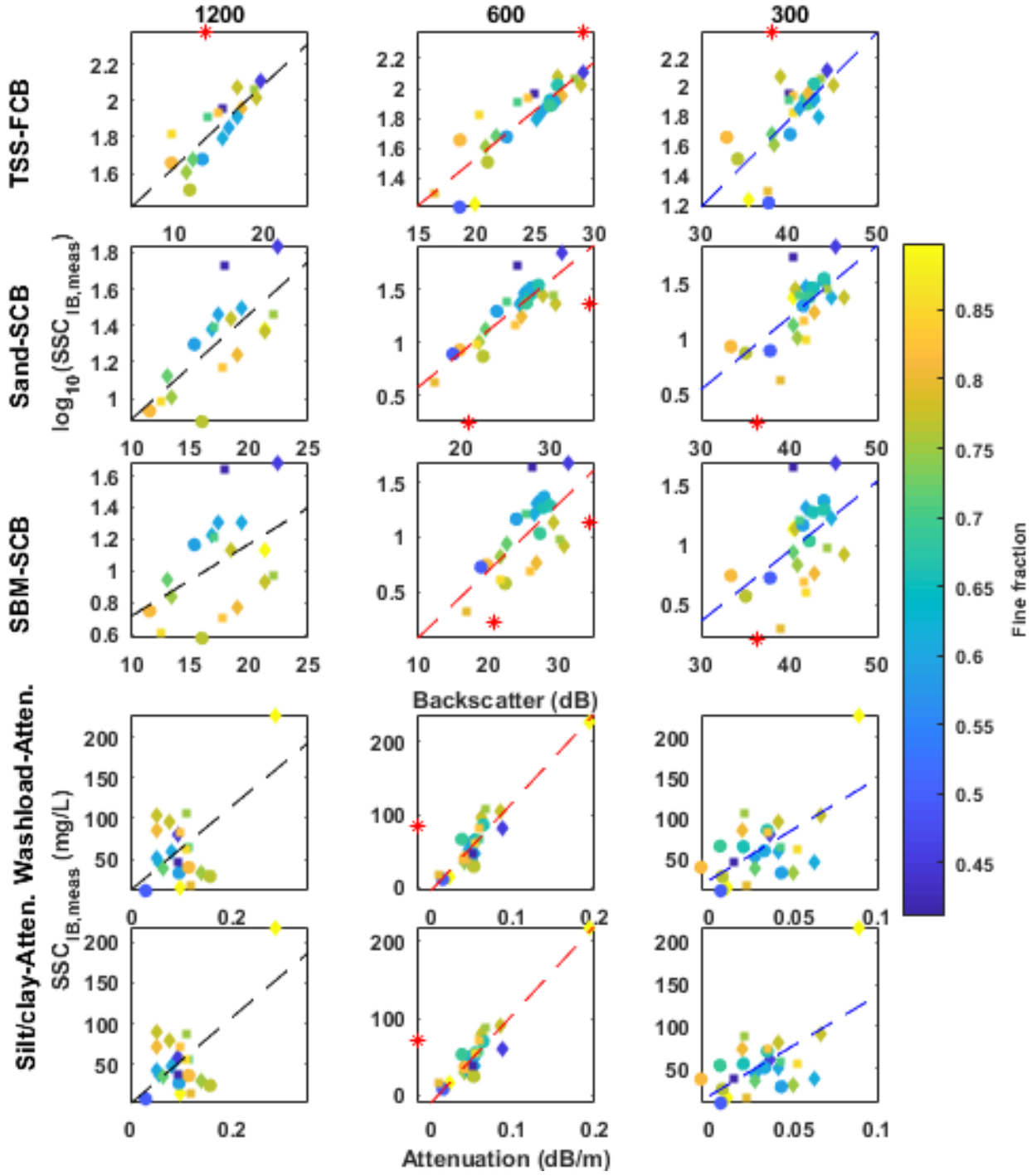

Figure 3.5. Calibration relations between in-beam suspended sediment samples, acoustic backscatter and sediment attenuation. Shapes represent sample years 2012 (square), 2013 (triangle), and 2014 (circle). The asterisks (*) represent outliers removed from the calibrations.

Figure 3.5 shows calibrations with the points distinguished by year and by silt/clay fraction. To assess any bias by year I compute the sum of the residuals for each calibration for each year (Table 3.2). The calibrations show some year-to-year changes around the line of unity (i.e. sum of residuals =0), suggesting some variability exists amongst years with respect to calibration. Table 3.3 lists slopes (*K1*) and intercepts (K_t) for TSS-*FCB* and Sand-*SCB* relations. Variability in K_t is to be expected because it includes frequency dependent parameters including source level and particulate size. There is also variability between years, which may be due to GSD characteristics. There is also inter-annual variability in calibration slopes (Table 3.3). The range of slopes captures the theoretical values of *K1* = 0.1 for 10 of the 16 calibrations. However, the upper bounds of the non-compliant ranges are within 58% of the theoretical value. The year-to-year trends show no clear pattern; they do not all increase or decrease with frequency within a year. This suggests that each frequency is responding differently to in-situ GSD characteristics.

Table 3.3. Slopes and intercepts for calibrations between FCB-TSS and SCB-Sand SSC separated by year

		2012					2013					2014				
Freq.	SSC	N	K1	[a]Range of K1	K_t	[a]Range of K_t	N	K1	[a]Range of K1	K_t	[a]Range of K_t	N	K1	[a]Range of K1	K_t	[a]Range of K_t
1200 kHz	TSS	6	0.062*	0.032-0.077	1.012	0.59-1.43	3**	n/a	n/a	n/a	n/a	11	0.055*	0.033-0.077	1.073	0.74-1.41
	Sand	6	0.081	0.033-0.13	-0.014	-0.76-0.73	3**	n/a	n/a	n/a	n/a	11	0.114	0.076-0.15	-0.737	-1.42--0.06
600 kHz	TSS	6	0.076	0.032-0.12	0.299	-0.60-1.20	8	0.074	0.038-0.11	0.195	-0.55-0.94	11	0.045*	0.021-0.069	0.918	0.39-1.44
	Sand	6	0.085	0.037-0.13	-0.802	-1.95-0.35	8	0.072*	0.055-0.089	-0.483	-0.91--0.06	11	0.042*	0.025-0.059	0.191	-0.25-0.64
	Silt/ Clay	6	1270	678-1862	-9.24	-40.72-22.24	8	1349	563-2135	-20.8	-58.4-16.8	11	1214	1024-1404	-16.9	-32.6--1.2
300 kHz	TSS	6	0.107	0.038-0.18	-2.358	-5.08-0.36	8	0.070	0.028-0.11	-1.019	-2.68-0.64	11	0.079	0.041-0.12	-1.237	-2.74-0.26**
	Sand	6	0.176	0.050-0.30	-6.135	-11.40--0.87	8	0.070*	0.055-0.085	-1.652	-2.27--1.03**	11	0.129	0.054-0.20	-4.325	-7.59--1.01

*Range does not encompass theoretical value of 0.1; ** Too few data points to calculate relation; [a]based on 2 x standard error of the slope and intercept.

An additional test of these calibration curves that has significance beyond the local environment is to analyze how well the predicted concentrations correspond to measured in-beam concentrations. Figure 3.6 shows that ADCP derived sediment concentrations, when compared to in-beam measured SSC, vary around the line of unity for both TSS and sand relations. The high concentrations in April 2014 are clearly outliers in the TSS relation. Figure 3.6 also shows the silt/clay sediment fraction of each SSC measurement (colorplot). The outlier in TSS has a large amount of silt/clay sediment and is the same outlier removed from the FCB-TSS calibration. Sand SSC shows more scatter around the line of unity with increased concentration, with a tendency to underestimate at the highest concentrations, particularly the 300 kHz frequency. Comparison between measured and predicted SBM, washload and silt/clay concentrations show more scatter around the line of unity for all except the 600 kHz ADCP, along with the coefficients of determination from the calibrations being less than 0.5 (Table 3.2), and therefore are not evaluated further in this paper.

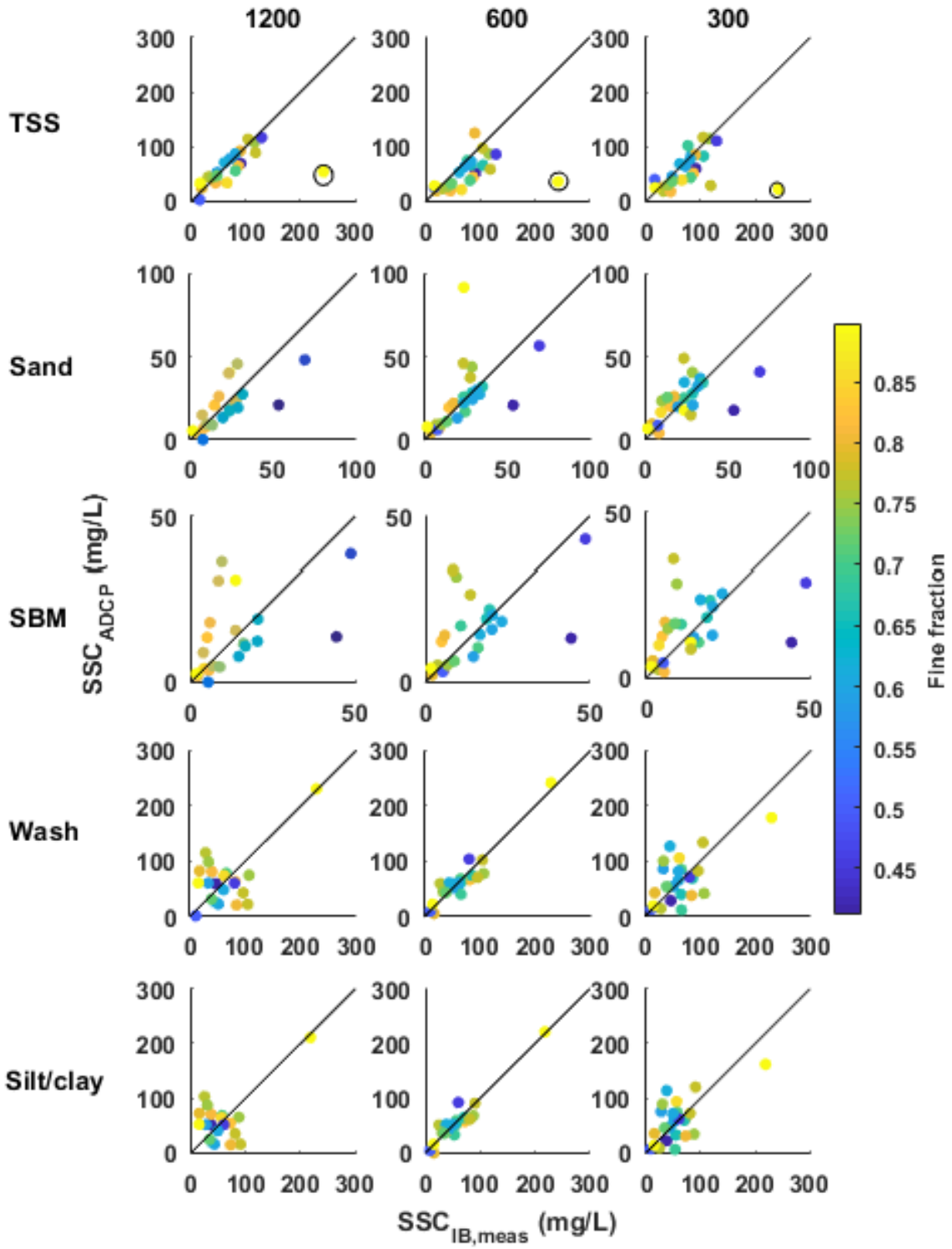

Figure 3.6. Measured in-beam suspended sediment samples and ADCP derived suspended sediment concentrations for total *SSC*, sand fraction, washload fraction and silt/clay fraction. The circled points in the TSS panels are the same outliers from the TSS-*FCB* calibrations in Figure 3.5.

3.5.2. Index-channel average extension

Because the ADCPs have an applied range that is roughly one tenth the width of the Fraser River at Mission, or less, the acoustically derived sediment concentrations reflect only a portion of the river and not the channel-average concentration. Following *Venditti et al.* (2016), I relate acoustically-derived concentration to channel-average concentration from sampling. All relations were forced through zero. Index-extension regression models and statistics are given in Table 3.4.

Slopes from all linear regressions show that channel average SSC is roughly 1.5-2.5X the index SSC. Relations between channel averaged TSS and ADCP derived TSS show $R^2 > 0.6$. Both the 1200 and 600 kHz ADCPs have strong relations for sand ($R^2 > 0.9$), while the 300 kHz has relatively more scatter and a poor R^2. The 600 kHz ADCP yields a strong R^2 for silt/clay (0.81). The regression of the relations for each sediment class are shown in Figure 3.7. The 1200 kHz instrument shows the tightest grouping around the regression model, followed by the 600 and 300 kHz ADCPs. Silt/clay regressions for the 600 kHz show a limited amount of data above 100 mg/L. Overall the 1200 kHz ADCP gave the strongest index correlation for TSS while the 600 gave strongest correlation for sand and silt/clay concentrations. The 300 kHz instrument gave the poorest results for both TSS and sand SSC.

Table 3.4. Regression model and statistics from relations between acoustically derived in-beam SSC and channel average SSC.

	1200				
	Model	**r^2**	**p-val**	**[a]SE of slope**	**[b]SEE**
TSS	Chan=1.83*IB	0.86	5.20×10^{-6}	±0.24	25.2
Sand	Chan=1.98*IB	0.9	7.30×10^{-7}	±0.21	8.09
Silt/Clay	n/a	n/a	n/a	n/a	n/a
	600				
	Model	**r^2**	**p-val**	**SE of slope**	**SEE**
TSS	Chan=2.25*IB	0.65	1.60×10^{-4}	±0.35	37.7
Sand	Chan=1.77*IB	0.96	7.30×10^{-11}	±0.10	5.37
Silt/Clay	Chan=1.26*IB	0.81	1.50×10^{-4}	±0.13	20.7
	300				
	Model	**r^2**	**p-val**	**SE of slope**	**SEE**
TSS	Chan=2.07*IB	0.61	3.70×10^{-4}	±0.34	40.0
Sand	Chan=1.99*IB	0.45	4.60×10^{-3}	±0.38	19.0
Silt/Clay	n/a	n/a	n/a	n/a	n/a

[a]Standard Error; [b]Standard Error of the Estimate; All p-values are significant at the 95% confidence level

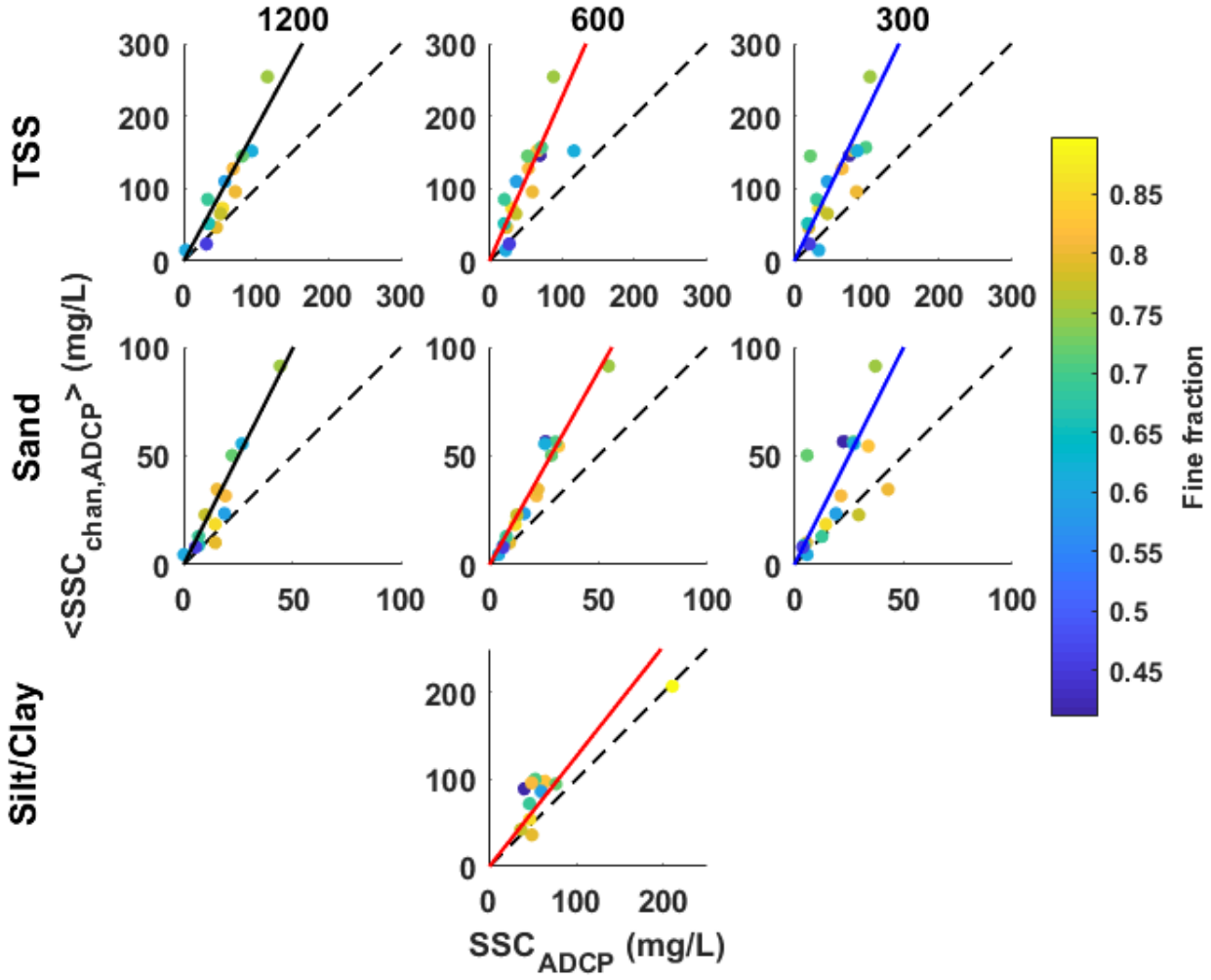

Figure 3.7. Relations between ADCP derived suspended sediment concentrations and channel average suspended concentration. These regression models are used to derive channel average SSC from ADCPs. Dashed lines are the line of unity.

Channel average concentrations are shown as daily average time-series for nearly three years (Figure 3.8). Overall, TSS concentrations show similar results between the 1200 and 600 kHz ADCPs, while the 300 kHz tends to give greater peaks and a narrower response to the freshet. For sand concentrations, the 1200 and 600 kHz ADCPs tend to track the TSS rising limb and generally decline prior to the TSS falling limb. During the freshet, silt/clay concentrations showed a peaked prior to both sand and TSS SSC. During the "first flush" in late April and early May of 2014 the 600 kHz showed a response that tracked the early peak, with concentrations of silt/clay sediment being greater than sand concentrations. Overall, measurements tend to track the 1200 and 600 kHz time-series well.

The Fraser peaked in TSS concentration at around 400 mg/L according to the 1200 and 600 kHz instruments, while the 300 kHz shows peak concentrations of approximately 600 mg/L. The peaks occurred on June 22nd, 2012, May 13th, 2013, and May 25th, 2014. Not all frequencies show TSS being greater than sand concentrations. During each year's freshet, the 1200 and 300 kHz frequencies show TSS values that are almost always greater than or equal to sand SSC, with the peak being the time when the two are close to equal. During peak flows the 600 kHz ADCP gives sand concentrations that are greater than TSS, while silt/clay concentrations tend to be greater than TSS just prior to peak flows and during low flow periods.

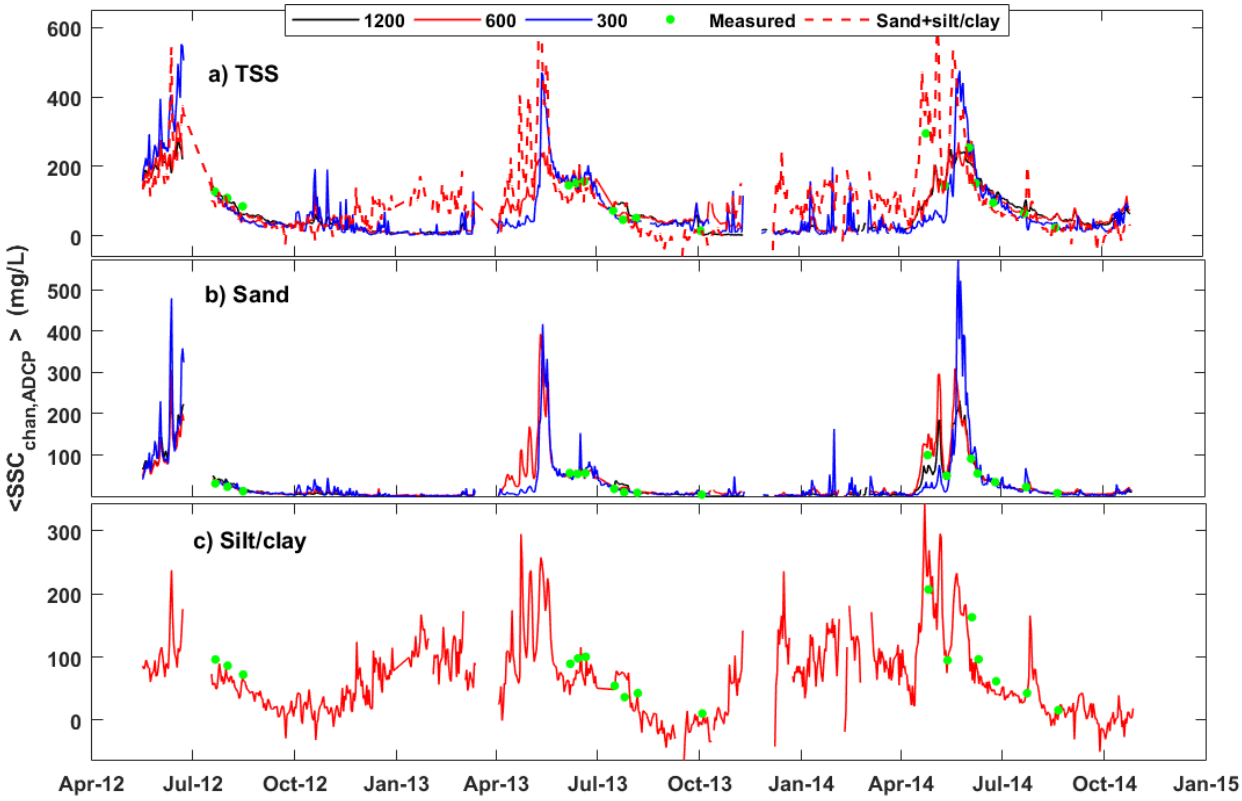

Figure 3.8. Time series of daily-mean channel average a) total, b) sand, and) silt/clay suspended sediment concentration for annum 2012-2014.

3.5.3. Sediment hysteresis

The capability to temporally decouple size-specific suspended sediment concentration from discharge is a significant advantage of the acoustic methods, especially with respect to increased temporal resolution. Different acoustic frequencies are thought to be sensitive to certain grain size distributions [*Topping et. al.*, 2007],

meaning that each frequency will respond differently to the SSC GSD. This allows one to derive sand and silt/clay SSC independent of discharge and of one another. Figure 3.9 shows a time-series of daily average size-specific SSC calculated for the 2014 freshet. I also plot fractional SSC against discharge using the 600 kHz instrument calibrations and index correlations.

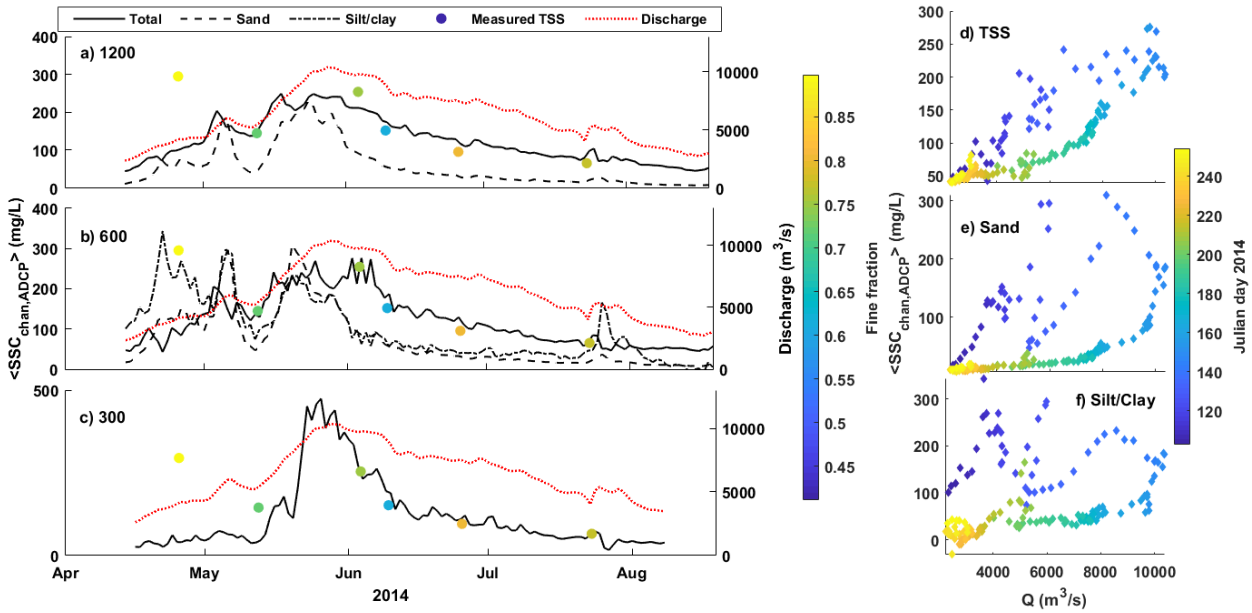

Figure 3.9 Daily average concentration for the a) 1200, b) 600, and c) 300 kHz ADCPs over the 2014 freshet. SSC- discharge relations for d) TSS, e) sand, and f) silt/clay fractions as a function of time.

The observed hysteresis clearly shows decoupling of the sedigraph from the hydrograph. TSS, sand, and silt/clay all respond on different time scales and at different discharges (Figure 3.9 a-c). The 1200 kHz instrument indicates that total and fractional SSC peak sediment concentrations generally lead the peak discharges. The 600 kHz instrument TSS SSC shows two responses, one prior to that of discharge, and another responding concomitantly. Sand SSC responds just prior to discharge, while silt/clay shows a peak prior to both sand and TSS SSC. The silt/clay response occurs earlier in the season when the first flush of silt/clay are delivered from the drainage basin, well before discharge increases substantially. The 300 and 1200 kHz instruments do not exhibit this behaviour. In fact, the 300 kHz instrument responds quite differently than the higher frequency instruments showing a narrower sedigraph response to the freshet. This makes sense because as the instrument frequency decreases, instruments become more sensitive to the coarser portion of the GSD. The 300 kHz is more sensitive to the

sand fraction and should not be as sensitive to the silt/clay fractions. Hence the poorer relations to TSS and silt/clay SSC (Table 3.2). Hysteresis curves proceed clockwise for all sediment size SSC for the 600 kHz instrument (Figure 3.9 d-f). This makes sense given that they peaked prior to discharge. The narrower hysteretic behaviour in TSS is likely due to its response mimicking discharge. The hysteretic observation supports the idea that each acoustically derived sedigraph is responding independently of hydrograph.

3.5.4. Channel average fluxes

Sediment fluxes were computed using Equation 3.11. Figure 3.10 shows a time-series of daily average sediment fluxes. The peak of fractional or total flux is difficult to resolve because the instruments were out of the water during this period. For 2013 and 2014, TSS results from the 1200 and 600 kHz frequencies show similar results in that they peak around 3000 kg/s (Figure 3.10a), while the 300 kHz shows greater peaks (~4700 kg/s). TSS flux measurements show good agreement with the time-series for all ADCPs, while time-series peaks are not captured. The TSS flux measurement during the April 2014 “first flush” is the one measurement that is clearly greater than the estimates derived from *FCB* for all frequencies (Figure 3.10a). I sum the sand and silt/clay flux to derive another estimate of TSS flux. Periods exist when the 600 kHz silt/clay and sand flux do not sum to the TSS flux, suggesting inaccuracies in one or more acoustic inversions. More interesting is that TSS from the sum of silt/clay and sand better aligns with the same April 2014 “first flush” sample.

Sand flux shows good agreement between all frequencies for 2012 on the rising limb and for 2013 over the whole sedigraph (Figure 3.10b). Sand flux for 2014 shows close agreement between the 1200 and 600 kHz, while the 300 kHz shows greater peaks. Sand flux measurements track the time-series sand flux well, with the 1200 and 600 kHz showing better alignment during the rising limb of 2014. This period coincides with the first flush, suggesting the 300 kHz is insensitive to silt/clay material. Measured silt/clay flux for the 600 kHz ADCP show a good response to acoustically derived silt/clay flux for all samples, with the greatest disagreement being in early July, 2013. This sample was taken on the falling limb of the 2013 sedigraph, when sand fractions are high.

Measured values tend to track the rising limb of the sum of sand and silt/clay flux better (Figure 3.10a inset), while the *FCB* derived TSS flux is tracked better during the falling limb (Figure 3.10a). This likely occurs due to silt/clay SSC being slightly overestimated on the falling limb (Figure 3.10c inset), possibly due to a lack of finer sediment in suspension. Additionally, sand tends to track the falling limb better (Figure 3.10b inset), suggesting that intra-annual sediment variability prevents the sum of sand and silt/clay from representing TSS measurements any better than TSS derived from *FCB*.

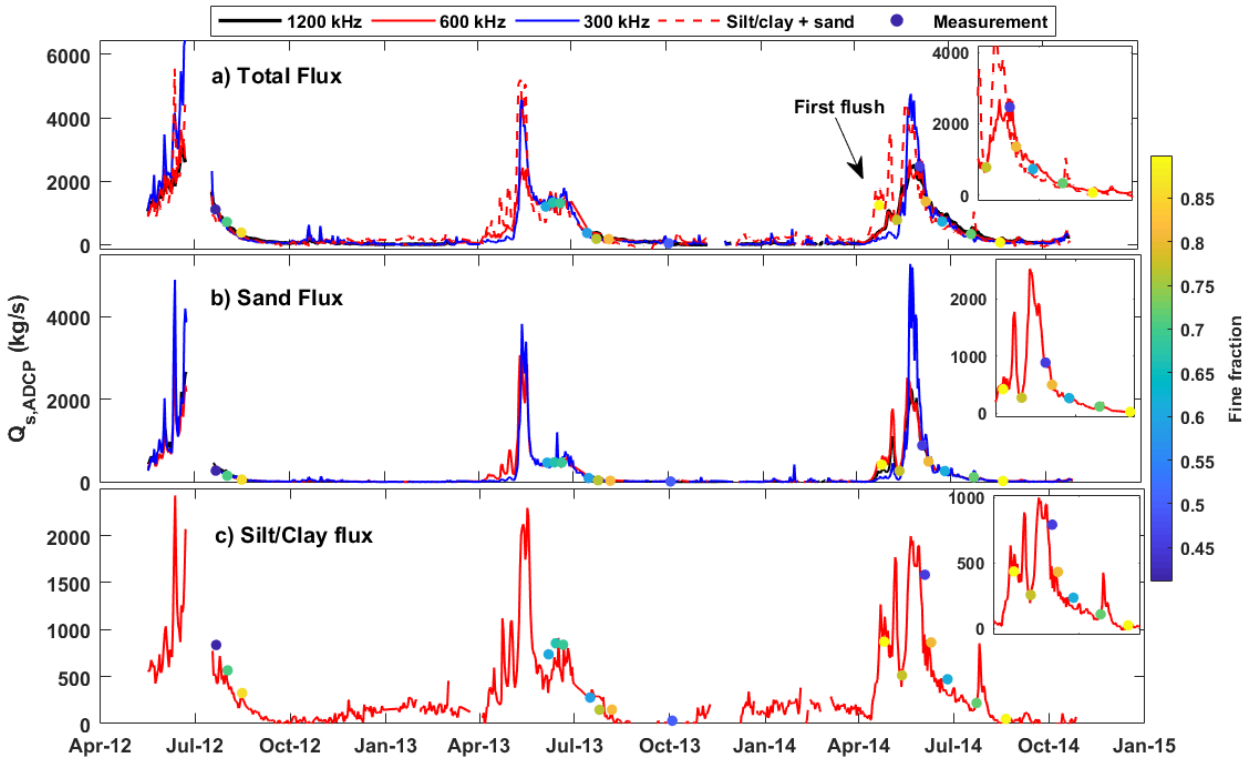

Figure 3.10. Time series of ADCP derived a) total, b) sand, and c) silt/clay sediment flux. Measured *TSS* flux samples computed using Equation 3.10.

Figure 3.11 shows the measured and predicted sediment fluxes. The1200 kHz ADCP gives the highest coefficient of determination results for TSS (0.83). The 600 and 300 kHz give relatively poorer coefficients of determination (>0.7), yet still strong. Sand flux tends to have the highest coefficient of variation and the strongest coefficients of determination for both the 1200 and 600 kHz ADCPs. Silt/clay flux has a coefficient of determination of 0.76 and a coefficient of variance of 52%. Little observed bias occurs along the line of unity for any acoustically derived flux with regards to fine fraction.

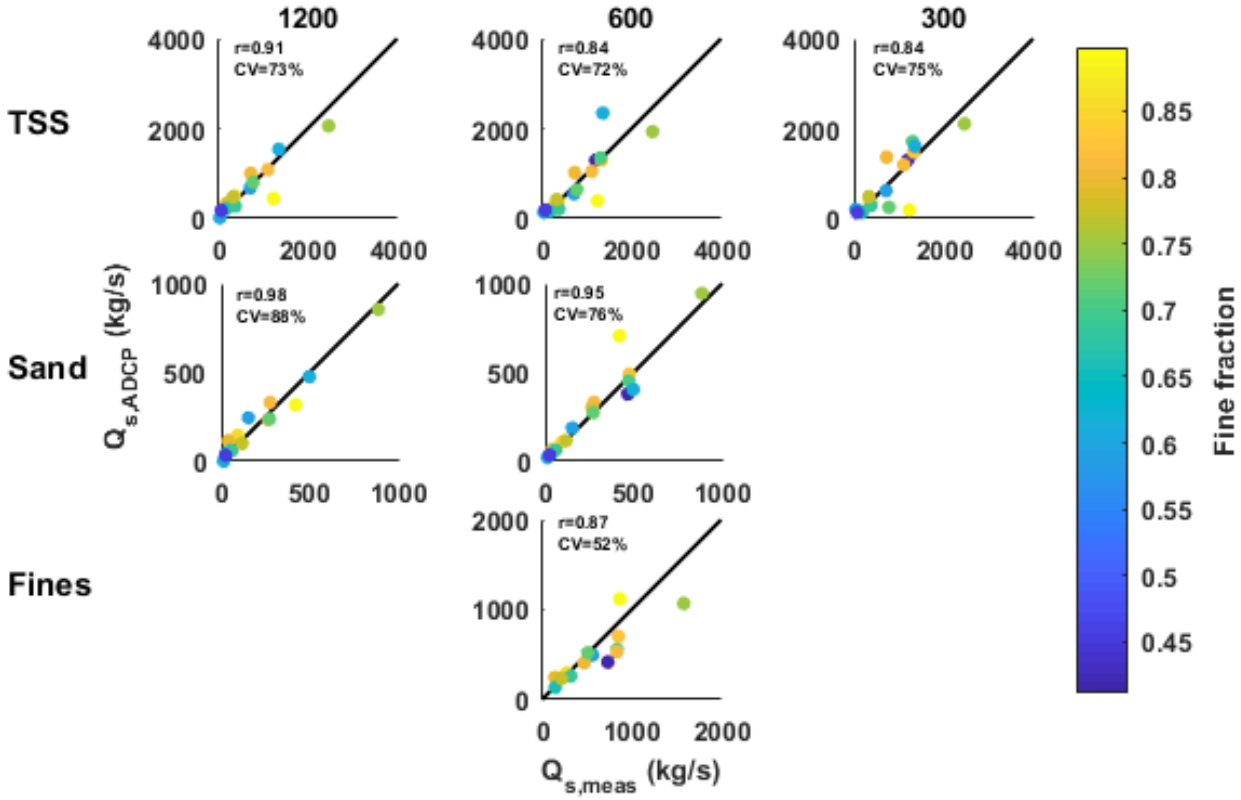

Figure 3.11. Measured versus acoustically derived channel average flux. The coefficient of variation (CV) is computed as the standard deviation of acoustically derived flux divided by the mean flux for each sample date, while r is computed using the Pearson correlation.

3.5.5. Annual flux

The integration of each year's data represents an estimate of the annual sediment load entering the lower Fraser River. To compute the annual sediment loads I integrated instantaneous flux for each relation. Missing days were linearly interpolated. Data from the 2013 freshet for the 1200 kHz ADCP were missing due to the instrument out of the water. Additionally, 2012 data did not encompass the full year, missing a portion of the rising limb. Therefore, the most comprehensive estimates of annual flux are obtained from 2013 for the 600 and 300 kHz ADCPs and from 2014 for all frequencies. Table 5 shows the results of flux computations by annum for all ADCPs.

Table 3.5. Annual flux for each annum by frequency in metric tonne per year (Mt).

	1200 kHz				600 kHz				300 kHz			
2012	$14.2x10^6$	$6.85x10^6$	n/a	n/a	$14.2x10^6$	$6.45x10^6$	$7.63x10^6$	$14.1x10^6$	$19.7x10^6$	n/a	n/a	n/a
2013	n/a	n/a	n/a	n/a	$12.0x10^6$	$5.87x10^6$	$8.45x10^6$	$14.3x10^6$	$11.5x10^6$	n/a	n/a	n/a
2014	$11.1x10^6$	$4.99x10^6$	n/a	n/a	$10.7x10^6$	$5.91x10^6$	$7.63x10^6$	$13.5x10^6$	$10.5x10^6$	n/a	n/a	n/a

When examining annual flux by year, Table 3.5 shows a general trend of 2012 having the highest fluxes, followed by 2013, and then 2014. The high flux for 2012 coincides with higher than usual flows in 2012. When examining annual flux by type, TSS flux from the 1200 and 600 kHz frequencies showed similar values between 2012 and 2014, while all three frequencies are consistent for 2014. The 300 kHz in 2012 gave the largest annual flux amongst all computed values. For sand flux, the 1200 kHz shows similar annual flux to the 600 kHz frequency. Silt/clay flux showed similar annual flux from the 600 kHz frequency for 2012 and 2014, while 2013 had the highest annual silt/clay flux. To test the accuracy of our TSS flux calculation, I sum sand and silt/clay flux from the 600 kHz ADCP (Table 3.5). For 2012, the sum of silt/clay and sand matches that of TSS flux well, while 2013 and 2014 give larger TSS flux than that derived from the TSS-FCB calibration.

3.6. Discussion

3.6.1. Stability of calibration models

The acoustic inversion method relies on two critical factors, the first being the calibration of the acoustic backscatter parameters (*FCB*, *SCB*, α_s) to suspended sediment total and fractional concentrations and the second being the index-channel average extension which relates acoustically derived in-beam SSC and channel average SSC. In order to utilize these acoustic inversions for long term monitoring programs, the slope and intercept of calibrations (Eq. 3.8) with regard to the in-beam/channel-average extension must be examined for stability.

3.6.2. Inter-annual variability

Thevenot et al. [1992] show that theoretically, the slope (*K1*) of the calibrations between backscatter and SSC should be approximately 0.10 (Eq. 3.8) and intercept (K_t) should be approximately -0.10. They assume a uniform a grain-size distribution (GSD) within the ensonified volume. Our observations show that the values of K_t range between -6.135 and 1.073 and the values of *K1* vary between 0.042 and 0.176. Furthermore, there is inter-annual variability (Table 3). If I compare the results of the inter-annual calibrations with the calibrations based on all years (Table 3.2), the median prediction would be 42 to 102% larger for the TSS-FCB calibration. For the Sand-SCB and silt/clay-α_s calibrations, the induced variability is less, 6 to 30% and -8 to 13% difference, respectively. This suggests that there is more inter-annual variability in the TSS-*FCB* calibration than in the size specific calibrations.

Observations from similar applications and environments using ADCPs also show variability in K_t and *K1*. Table 3.6 summarizes values for K_t and *K1* of inversions from other investigations with sediments that are different, both in concentration and GSD, relative to our work. It appears, from Table 3.6, that with increased sand percentage, *K1* increases, while K_t decreases. Table 3.6 suggests lower slopes for studies that occur in environments dominated by silt/clay material. The large variability around a slope of 0.1 amongst years in our calibrations may be a result of the material being finer than those reported in previous studies [*Topping et al*., 2007; *Wright et al*., 2010; *Woods and Teasdale*, 2013]. In dynamic environments where source material

changes annually, size-specific calibrations may vary, inducing error in flux estimates. In cases where the changes are known and consistent and therefore site specific, variability may not be a problem, but when the characteristics of the GSD vary widely and unpredictably, stability in the calibrations should be explored.

Most notable in Table 3.6 are the results of *Venditti et al*. [2016], who used the same 300 kHz ADCP in their investigation as I do, at the same site, but at a different depth and with the ADCP angled down at 1.2°. Their K1 and K_t are similar to our 2012 values shown in Table 3.3, yet deviate from 2013, 2014, and our calibration for all years (Table 3.2). Nevertheless, the K1 standard errors range overlaps with those reported in *Venditti et al.* [2016], but the K_t values are different. This suggests that the calibrations may be site specific and depend on the instrumentation orientation.

Table 3.6 Summary of calibration coefficients from literature using horizontal ADCPs in river and estuarine environments.

Literature	Field/Lab	Suspended material	Concentration range (mg/L)	Slope (K_1)	Intercept (K_t)
Thevenot et al. (1999)	Field-James R. estuary	silt/clay	5-1000	0.042	1.43
Thevenot et al. (1999)	Lab	silt/clay	18-110	0.077	0.92
Wright et al. (2010)	Field-various rivers	sand	5-630	0.13	-9.23
Woods and Teasdale (2013)	Field-Clearwater R.	TSS	3-210	0.056	-2.4
Woods and Teasdale (2013)	Field-Clearwater R.	Sand	3-211	0.076	-4.1
Woods and Teasdale (2013)	Field-Snake R.	TSS	6-414	0.056	-4.7
Woods and Teasdale (2013)	Field-Snake R.	Sand	6-415	0.11	-7.6
Topping et al. (2007)	Field- Colorado R.	Sand	3-3100	0.11	-7.4
Venditti et al. (2016)	Field- Fraser R.	TSS	15-100	0.098	-6.89
Venditti et al. (2016)	Field- Fraser R.	Sand	2-32	0.136	-11
This study- TSS (1200 kHz)	Field- Fraser R.	TSS	40-130	0.054	1
This study- sand (1200 kHz)	Field- Fraser R.	Sand	4-70	0.079	-0.1
This study- TSS (600 kHz)	Field- Fraser R.	TSS	40-130	0.072	0.1
This study- sand (600 kHz)	Field- Fraser R.	Sand	4-70	0.076	-0.7
This study- TSS (300 kHz)	Field- Fraser R.	TSS	40-130	0.083	-1.5
This study- sand (300 kHz)	Field- Fraser R.	Sand	4-70	0.096	-2.8
Mean				0.084	-3.4
Standard deviation				0.031	4.1
Minimum			2	0.042	-11
Maximum			3100	0.136	1.43

3.6.3. Intra-annual variability

Venditti et al. [2016] showed that calibrations can change seasonally. They found that the calibration shifted from pre-peak to post- annual peak discharge. Our results appear to support this finding, although I cannot examine pre- and post-freshet calibrations because of a limited number of pre-freshet samples. So, I explored this intra-annual variation by dividing the calibration of the 600 kHz by high and low flow (Figure 3.12). I choose the division as (>5000 m^3/s) because, in the Fraser, this is when sand stored in the upstream gravel reach is entrained and delivered to the sand reach (*McLean et al.*, 1999; *Venditti and Church*, 2014; *Venditti et al.*, 2015). Figure 3.12 shows the slope and intercept of the calibration are different between high and low flow periods. During the high flow periods slopes decrease for relations between TSS-*FCB* and sand-*SCB*, which suggests finer sediment contributions dominate the calibrations at higher flows while coarser contribution dominate during lower flows. The relation between silt/clay-α_s shows larger slopes at high flow and lower slopes at low flow. This phenomenon is consistent Figure 3.4d in that at low flows the GSDs are coarser because the sediment is sourced from the bed. This is also consistent with Table 3.6 in that calibration slope for coarser sediment regimes were higher. However, all calibration slopes are within a range of two standard errors of one another, showing that there is no statistically significant difference between the high and low flow division. Nevertheless, if I compare the results of the intra-annual calibrations with the calibrations based on all years (Table 3.2), the median prediction would be 5 to 80% different for the TSS-FCB calibration at high and low flow, respectively. For the sand-SCB and silt/clay-α_s calibrations, the median prediction would be 3 to 13% and 3 to -8% difference at high and low flow, respectively.

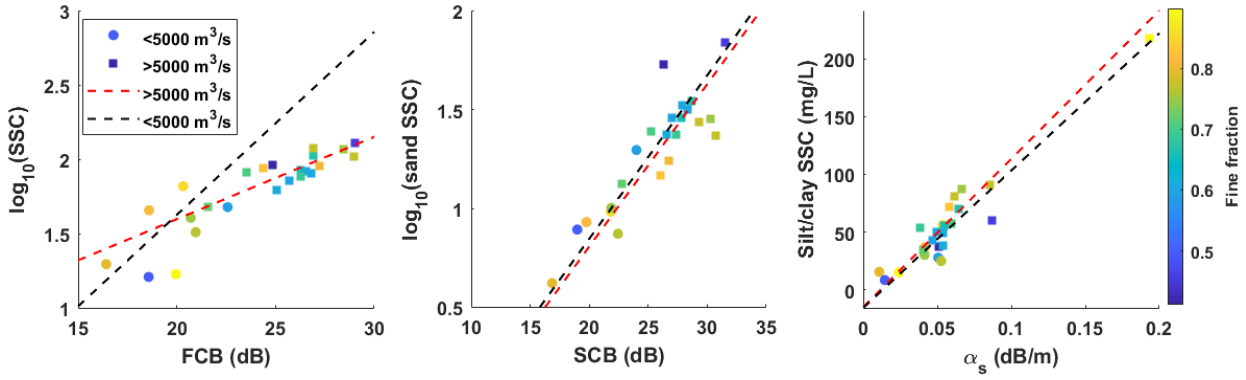

Figure 3.12. Calibrations for the 600 kHz ADCP separated by high and low flow (5000 m^3/s).

3.6.4. Are the calibrations theoretically-based or simple correlations?

Venditti et al. (2016) argued that while the calibrations between acoustic signal properties and SSC have some theoretical basis, they are merely empirical correlations, the continuing validity of which will depend on consistency in the makeup of the suspended sediment load in the river. In sand-bedded rivers where silt and clay transport (washload) is somewhat decoupled from sand transport, *Topping and Wright* [2016] have shown more successful applications of similar semi-empirical methods. These contradicting results suggest that the sedimentological conditions of the river dictate the success of the method, which supports the assertion of *Wright et. al* [2010] and *Venditti et. al* [2016] that the calibrations site specific. The method applied herein is better justified theoretically than the empirical calibrations developed by *Venditti et al.* (2016), who calibrated TSS, sand and silt/clay concentrations against *SCB*. Acoustic backscatter should be more sensitive to sand and sediment attenuation should be more sensitive to silt-clay [*Flammer*, 1962]. However, some of the results suggest that this more theoretically sound approach is still a series of empirical relations and not formal calibrations.

There is inter- and intra-annual variation in the calibrations and a poor fit to theoretical expectations [e.g. *Thevenot et al.*, 1999]. The different frequency ADCPs respond to the sedigraph differently. The sum of the sand-*SCB* and silt/clay-α_s calibrations do not sum to the TSS-*FCB* derived flux (Figure 3.13a and b; Figure 3.10a) during all flows. The problem is in part due to TSS-*FCB* derived contributions being influenced by attenuation, which is not accounted for in the calibration. Furthermore, the sum of sand and silt/clay flux do not better represent measured flux, partially due to a

systematic bias associated with flow (Figure 3.13b), likely due to changing sedimentology. Our results clearly show that when SSC exceeds ~150 mg/L the TSS-*FCB* calibration drifts. There is a lack of high SSC samples in our data set, which prevents exploration of this threshold. However, the one sampling campaign at high concentrations during the first flush in April 2014, which is treated as an outlier, shows the drift. Once *FCB* was corrected using the in-situ attenuation, this outlier aligned with the trend in the data of the sand-*SCB* relation. But I do not know how attenuation affects the TSS-*FCB* relation at lower concentrations. Because attenuation needs to be accounted for in higher concentration environments, TSS-*FCB* relations are not appropriate for long-term monitoring programs where calibration drift would likely increase the error associated with estimates of concentration.

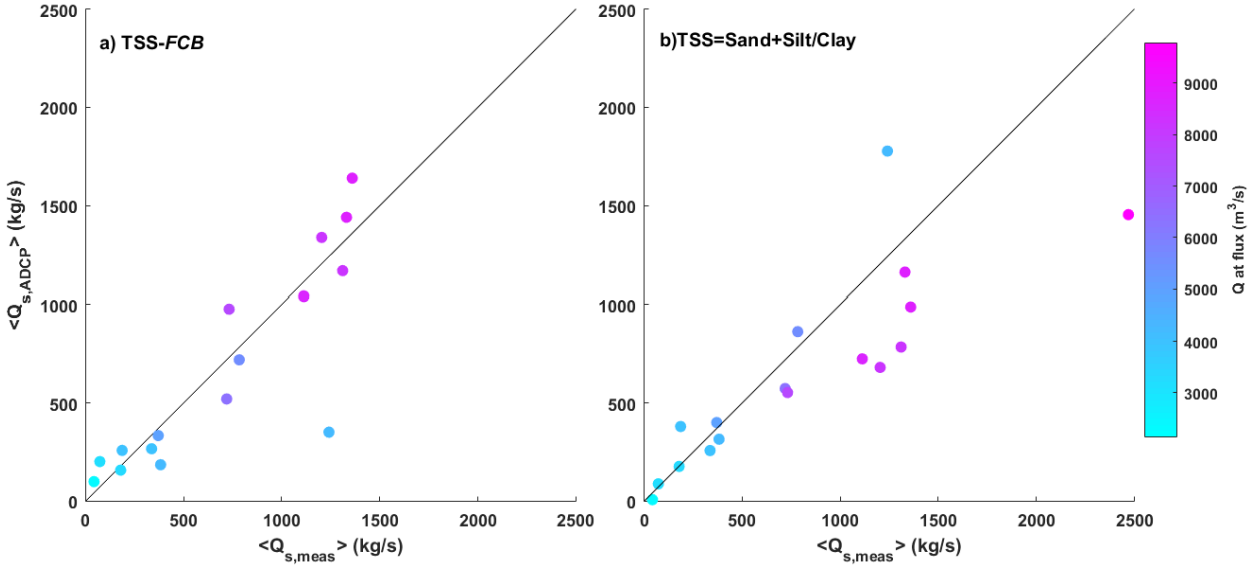

Figure 3.13. Comparison of TSS flux derived from a) TSS-*FCB* calibrations and b) the sum of sand and silt/clay flux as a function of discharge.

Despite the problems with agreement between the sum of fractional calibrations and TSS-*FCB* calibration, the silt/clay-α_s and sand-*SCB* calibrations do perform well at certain flows. The first flush of sediment during a sampling campaign in April 2014 is well captured by the silt/clay-α_s calibration and the predominance of sand in suspension on the falling limb of the freshet is well predicted by the sand-*SCB* calibration (Figure 3.10b inset). There also does not appear to be any systematic bias in the sum of the fractional calibrations and index relations with respect to the measured fluxes. This supports the contention of *Venditti et. al* [2016] that the index correlation cancels any calibration bias and permits monitoring of size-classified suspended sediment in

absence of detailed information of sediment grain-size distribution. Nevertheless, the theoretically more robust approach appears to be sensitive to variations in grain-size, concentration and sediment composition. This makes them site-specific correlations that need to be maintained as conditions change.

3.6.5. How do acoustically derived flux measurements compare to measured fluxes from past observations?

The two-stage method employed here permits calculation of annual sediment fluxes for the Fraser River. *McLean et al*. [1999] who computed size-dependent fractional flux from measurements collected by the Water Survey of Canada between 1966 and 1986. Using methods outlined in *McLean and Church* [1986] they calculated sediment flux from bottle samples measured daily from middle of the Mission Rail Bridge (Figure 3.1c). To compute sand SSC, a power-law relation between sand fraction and discharge was used. The difference between TSS and sand *SSC* was used to compute the silt/clay fraction, which was then further divided by using the ratio 3.3:1 for the silt to clay *SSC* ratio. Annual sediment fluxes for TSS, sand and silt/clay are shown in Figure 3.14. The mean TSS flux from 1966 to 1986 was 17×10^6 Mt with a standard deviation of 6.0×10^6. Sand and silt/clay averages were 6.1×10^6 ($\pm 3.1 \times 10^6$) and 11×10^6 ($\pm 3.5 \times 10^6$), respectively.

I cannot apply the *McLean and Church* [1986] method, because I lack the daily sediment sampling necessary to apply it. However, I can compare our acoustically based fluxes to the historical record (Figure 3.14). I additionally plot the sum of sand and silt/clay in comparison to TSS from *FCB*. Both the sum of sand and silt/clay, along with TSS -*FCB* flux fall in line with historical flux. Acoustically derived annual fluxes are in good agreement with the results of *McLean et al*. [1999], when compared to total discharge, while generally falling in the lower end when compared to peak discharge (Figure 3.14). These results show acoustically derived flux can be used in monitoring programs to generate valuable information for river engineers and scientists.

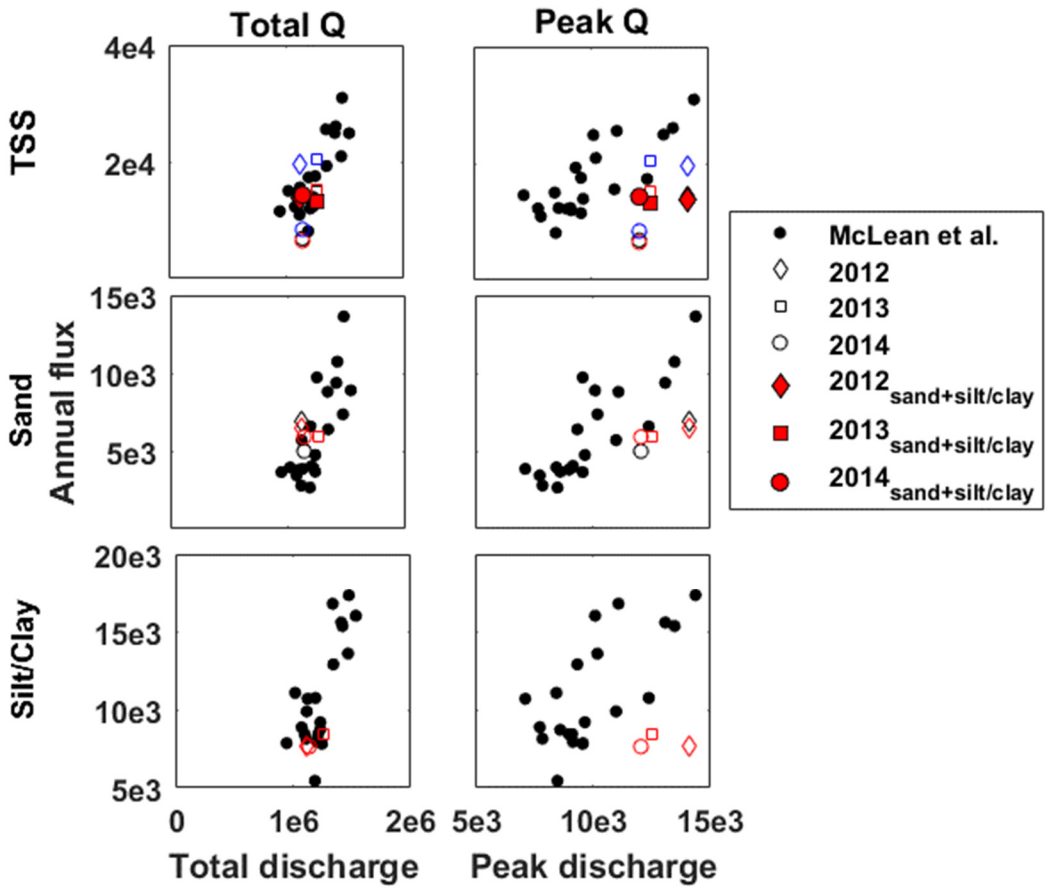

Figure 3.14 Annual flux from this study compared to that of *McLean et al*. [1999]. Value units are in 10^3 ta^{-1}

3.6.6. Recommendations for sediment monitoring in low concentrations environments?

I have shown that that the 600 kHz produces the strongest acoustic calibrations and the second strongest index-channel average extension correlations, which suggests that this instrument produces the most reliable estimates of flux in environments similar to that of the Fraser River. The two-step process I employ for calibrating the ADCP, then using an index relation leads to strong acoustic estimates of *SSC* (Figure 3.6), particularly for sand and silt/clay *SSC*. Though I use the 300 kHz for an estimate of discharge due to its strong index relations, the 600 kHz was strong as well and could have been used (Figure 3.3). The 600 kHz captures the hysteretic behaviour that occurs in the Fraser R. and additionally produce flux estimates that track physical measurements (Figures 3.10 and 3.11). These estimates lead to the estimates of annual flux that align with historical observations (Table 3.5 and Figure 3.14), suggesting a

robust method. Furthermore, the 600 kHz calibrations tend to show the least amount of variability amongst frequencies (Tables 3.2 and 3.3). Therefore, under conditions described in this paper, I recommend the 600 kHz ADCP for use in acoustically estimating *SSC*, discharge, and flux.

3.7. Conclusions

I have examined the capability of semi-empirical acoustic inversions to estimate total and fractional channel average *SSC* and flux. Building on work by *Venditti et al.* [2016], I use a two-stage method for estimating sediment flux that involves 1) calibration of the ADCPs using direct samples in the acoustic beams and 2) development of an index relation extension for sediment that links the ADCP derived concentrations to the channel averaged cross-section concentration. The second step provides a means to estimate channel average concentration and flux in systems with cross-channel variability in sediment concentrations or with greater widths than horizontal ADCPs range. I use data from multiple years, which allows us to explore both intra- and inter-annual variability in the calibrations.

Our analysis has shown that:

- In low concentration environments, the 600 kHz ADCP is best for monitoring sand and silt/clay SSC and that TSS is best calculated as sum of sand and silt/clay SSC or flux.

- Beyond a threshold of 150 mg/L calibrations between TSS and FCB shift due sediment attenuation that is not accounted for in *FCB*. Attenuation may also affect the TSS-FCB relation, but the influence is not obvious from our data.

- In the Fraser River, channel average SSC is 2X that of the index sediment concentration, which shows the inherent need for our method.

- There is inter and intra annual variability in acoustic calibrations, which suggest that calibrations are site specific correlations, sensitive to variations in grain-size, concentration and sediment composition.

- Despite this, acoustically derived annual sediment flux falls are the same order of magnitude as historical observations suggesting that the index relation of the two-stage method cancels out any bias in the calibrations.

The presence of inter and intra-annual variability in the acoustic calibrations could lead to errors in annual sediment fluxes. This variability is linked to changes in grain-size distributions and composition. Maintenance of calibration curves required continuous sampling. Multi-frequency acoustic inversions [e.g. *Hay*, 1991] that can estimate particle size information would provide valuable information that could reduce error associated with changes in GSD characteristics and may eliminate the need for continuous sampling to maintain calibrations. Additionally, when coupled with discharge estimates, multi-frequency acoustic inversions may provide insight into the relations between discharge, grain-size and sediment concentration.

3.8. Appendix 3.1: Single Spectral Analysis (SSA)

The single spectral analysis (SSA) method modified by *Schoellhamer* (2001) that accounts for missing data. For a time-series, x_i, with N samples and a window/lag size G, the Toeplitz, T_x, lagged correlation matrix can be defined as:

$$c_j = \frac{1}{N-j}\sum_{i=1}^{N-j} x_i x_{i+j} \quad 0 \leq j \leq \text{M-1} \tag{A3.1}$$

and from *Vautard et. al.* (1992),

$$\sum_{k=1}^{M} \lambda_k \mathrm{E}_j^k = T_{x,j} = c_j \tag{A3.2}$$

where the eigenvectors, λ_k, and eigenvalues, $E_{j,k}$, are sorted in descending order. Here j and k vary from one to the size of the window, G. The k^{th} principal component is then computed as:

$$a_i^k = \sum_{j=1}^{M} x_{i+j} E_j^k \quad 0 \le i \le \text{M-N} \tag{A3.3}$$

where the principal component of the time-series can be reconstructed by:

$$x_i^k = \frac{1}{M} \sum_{j=1}^{M} a_{i-j}^k E_j^k \quad \text{M} \le i \le \text{N-M+1} \tag{A3.4}$$

A complete description of the SSA method can be found in *Vautard et. al.* (1992) and *Schoellhamer* (2001). For our analysis, I use a maximum lag, G, of 120 (12 hr) to compute the Toeplitz matrix. The eigenvalues contain values of variance of the raw data (*Vautard and Ghil*, 1989; *French et. al.*, 2008) which, when plotted against the number of principal components, reaches a steady state after five principle components and was therefore the number of components used for our analysis. To reconstruct our time-series I use the first four principle components, which account for approximately 94% of the variance (found in eigenvectors λ_k) Figure A3.1 shows a time series (Figure A3.1a) of the raw data during low flow periods and during the peak of the freshet (Figure A3.1b).

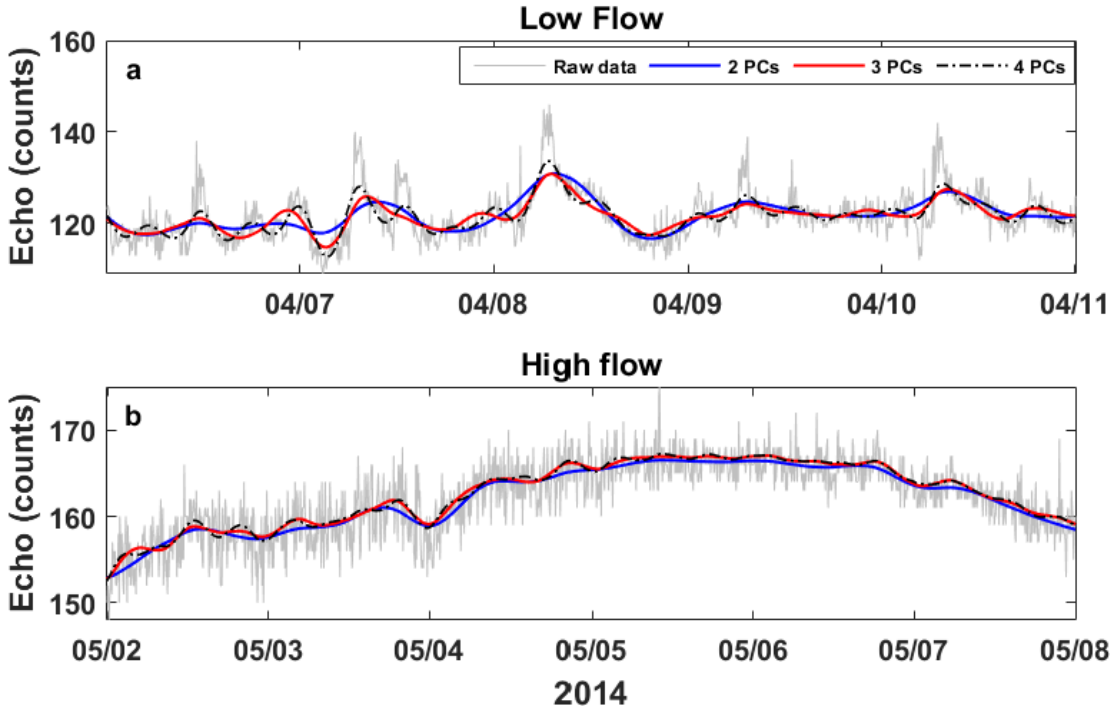

Appendix 3.1 Time series of bin 1 for the 1200 kHz ADCP showing the influence of the filtering process on the raw data during low flow (a) and high flow (b). This process is run for each bin, as described in the text.

Chapter 4. Application of multi-frequency acoustic inversions using “off the shelf” ADCPs

Abstract

An array of three horizontally-mounted acoustic Doppler current profilers was used to estimate, through acoustic signal inversion, suspended sediment concentration, particle size, and grain-size distribution (GSD) breadth on the Fraser River at Mission, BC. I examine two different multi-frequency methods, an explicit and implicit inversion, by systematically varying concentration, median particle size, and GSD standard deviation. I couple these inversions with bottle samples collected within the ensonified volume that were analyzed for suspended sediment concentration and GSD characteristics. Additionally, I estimate the necessary calibration parameters needed for complete acoustic inversions. Fraser River suspended sediment concentrations ranged from 20 to 350 mg/L with GSD characteristics dominated by silt to fine sand. The calibration parameter was shown to be sensitive in the inversion process when estimating concentration, influencing estimates of particle size. Comparisons between the inversion results and sample data show that the implicit method tends to perform best at all flows for estimating concentration, while providing realistic estimates of particle size at high flows only. The explicit method performed well at high flows, but poorly at low flows, for concentration and particle size. Estimates of GSD standard deviation using both inversion methods indicate frequency dependence such that a more robust method is desirable.

4.1. Introduction

Prediction of suspended sediment flux from hydraulics remains a stubbornly difficult problem, particularly for the washload component which is controlled by sediment supply from the drainage basin. Traditional methods, such as sediment rating curves, can produce significant error [*Walling*, 1977], especially when hysteretic relations are present [*McLean et al.,* 1999a; *Topping et al.*, 2000a, 2000b*; Kleinhans et al*., 2007; *Landers and Sturm*, 2013; *Warrick et al.,* 2013; *Waters and Crowe Curran,* 2015; *Topping and Wright,* 2016]. In rivers with large drainage basins, source material can vary both inter- and intra-annually creating variability in grain size distribution (GSD) and composition. Routine monitoring remains the primary means of estimating sediment fluxes in rivers. Over the last several decades the use of "off-the-shelf" acoustic Doppler current profilers (ADCPs) has become an increasingly popular tool for monitoring discharge in rivers and have more recently been used to estimate suspended sediment concentrations (SSC) [*Wall et al.,* 2006; *Sassi et al.,* 2012; *Moore et al.,* 2013; *Woods and Teasdale,* 2013; *Venditti et al.,* 2016; *Topping and Wright,* 2016]. Coupling observations of SSC, velocity and/or discharge data provides an opportunity to estimate sediment flux.

The sonar equation can be inverted to estimate sediment concentration and mean particle size from the returned acoustic backscatter signal. The linear version of the sonar equation has the following form:

$$P_{rms} = \overbrace{P_o r_o \beta \left\{\frac{3\tau c}{16}\right\}^{1/2} \frac{0.96}{k a_t}}^{k_t} \overbrace{\left[\frac{\langle f \rangle}{\sqrt{\langle a \rangle \rho_s}}\right]}^{k_s} \left[\frac{M^{1/2}}{r\psi}\right] e^{2r(\alpha_n)} \tag{4.1}$$

where P_{rms} is the root-mean-square pressure and is derived from acoustic intensity received by the ADCP (see Appendix 4.1), P_o (1 μPa) is the reference pressure at range r_o (1 m), r is distance from transducer, a is particle radius, a_t is transducer radius, τc is pulse length (c is speed of sound and τ is the acoustic transmit pulse), ρ_s is particle density, k is the acoustic wave number, M is mass concentration, f is the backscatter form function that describes the scattering properties of the GSD (see Appendix 4.2), k_s is a combination of the backscattering parameter that is a function of the GSD and acoustic wavelength (see definition in Appendix 4.2), $\beta = T_v R$ where T_v is the voltage

transfer function of the ADCP and *R* is the transducer receive sensitivity, ψ accounts for departure from spherical spreading in the near-field, and α_n is the attenuation coefficient [*Thorne and Hanes,* 2002] and is due to the fluid and sediment within the ensonified volume (the sediment attenuation coefficient is defined in Appendix 4.3). The *n* subscript denotes attenuation in nepers/m, while the angle brackets represent an average over the GSD. To simplify Equation 4.1 instrument constants or variables that vary solely with the celerity of sound and not environmental conditions are combined into k_t (further defined in Appendix 4.4).

Two different approaches to inverting acoustic backscatter to concentration and grain size have been previously used; single and multi-frequency inversions. When using ADCPs, single frequency inversions [*Hointink and Hoekstra,* 2005; *Sassi et al.,* 2012*; Venditti et al.,* 2016; *Topping and Wright,* 2016] commonly use the sonar equation rewritten in logarithmic form as:

$$RL = SL - (SP + AT) + 10log_{10}(M) + \overbrace{10log_{10}\left\{\frac{\langle f\rangle^2}{\langle a\rangle}\frac{3\tau c}{16}\left[\frac{0.96}{ka_t}\right]^2\right\}}^{TS} \tag{4.2}$$

where *RL* is reverberation level, *SL* is source level, *SP* is the spreading loss, *AT* is the attenuation loss and the last term *TS* is the target strength. In logarithmic form the units are decibels. Combining *SL* and *TS* into a system variable K_t, which varies with particle size, frequency, and celerity of sound, the sonar equation is:

$$log_{10}(M) = 0.1(RL + 2TL) - 0.1K_t \tag{4.3}$$

where 2*TL* is the two-way transmission loss (*SP* + *AT*) [*Wright et al.,* 2010]. The theoretical value of 0.1 derives from the definition of the decibel. The term (*RL* + 2*TL*) is the measured backscatter corrected for transmission losses along the beam path by fluid and sediment attenuation. Equation 4.3 can be used to invert backscatter to compute concentration, but only if particle size is specified. Since particle size is often not known, and variable, Equation 4.3 has been typically applied empirically through regressions between log10(M) and (RL+2TL); using this approach, the slope and intercept provide the necessary parameters for the inversion (slope is typically allowed to vary from its theoretical value of 0.1). The primary limitation of this approach is that it implicitly

assumes that particle size is constant, which limits its accuracy [*Topping and Wright*, 2016].

An alternative to the single frequency semi-empirical approach is to use multi-frequency methods (defined as two or more frequencies) to estimate *M*, mean grain size, [*Hay,* 1983, 1991; *Thorne et al.,* 1991; *Thorne at al.,* 1993; *Thosteson and Hanes,* 1998; *Thorne and Hanes,* 2002;] and, using at least three frequencies, the standard deviation of the GSD. Multi-frequency methods have been successfully applied using custom built transducers in sandy nearshore environments [*Hay and Sheng,* 1992; *Thorne et al.,* 2007] and laboratory experiments [*Sheng and Hay,* 1988; *Thorne and Campbell,* 1992; *Thosteson and Hanes*, 1998; *Moate and Thorne,* 2009] where grain size distributions have a near constant standard deviation (σ_g), but the geometric mean particle diameter (D_g) changes. Multi-frequency inversion techniques have also been used in estuarine environments [*Thorne et al.,* 1994; *Thorne and Hardcastle,* 1997] where GSDs are more dynamic due to differing sediment sources, rapid settling and resuspension, or flocculation. This has led to laboratory studies of the acoustic response to suspensions with different particle shapes [*Thorne et al.,* 1995a; *Richards et al.,* 2003; *Thorne and Buckingham*, 2004], mixed mineralogy [*Schaafsma and Hay*, 1997; *Moate and Thorne*, 2011, 2013], broad GSDs (*Moate and Thorne,* 2009), and flocculated aggregates [*MacDonald et al.,* 2013; *Thorne et al.,* 2014].

The successful application of multi-frequency inversions in lab experiments as well as nearshore and estuarine environments has led to interest in using similar methods with ADCPs in rivers. This application is somewhat more difficult because ADCPs have greater spatial range (10's of meters), larger sampling volumes (cubic meters) and require the estimation of various instrument constants for the acoustic inversions. Custom built transducers do not suffer from the latter problem, because instrument constants can be easily measured in laboratory settings or are known from instrument design. Here, I examine the effectiveness of the multifrequency inversions using 'off-the-shelf' ADCPs in a low concentration setting.

4.2. Multi-frequency inversion theories

In multi-frequency approaches, mass concentration, *M*, is calculated by inverting Equation 4.1 for an individual frequency [*Hay*, 1991], by:

$$M = \frac{P_{rms}^2 r^2 \psi^2}{k_t^2 k_s^2} e^{4r(\alpha_f + \alpha_s)} \tag{4.4}$$

where α_f and α_s are attenuation of sound from fluid and particulates in suspension, respectively. Sediment attenuation is defined as:

$$\alpha_s = \langle \zeta_{total} \rangle M = M\langle \zeta_{visc} \rangle + M\langle \zeta_{scatt} \rangle \tag{4.5}$$

where ζ_{scatt} and ζ_{visc} are the sediment and viscous attenuation coefficients defined in Appendix 4.3.

Equation 4.4 is an implicit equation because *M* is on both sides of the equation and cannot be separated from the computation of sediment attenuation (Eq. 4.4 and 4.5). In multi-frequency implicit inversions, concentration is determined by minimizing the variation of the inverted signal among all frequencies. This requires large computation times because iterations occur at each time-step for each location along the acoustic beam. Implicit inversions also tend to propagate error from uncertainties in inversion parameters cumulatively by integration over the acoustic beam range. There are two different methods to determine suspended sediment concentration and mean particle diameter using implicit methods, which I term 'coupled' and 'decoupled'. The decoupled method first determines particle diameter from the minimization process, then computes concentration using the given particle diameter [*Hay and Sheng,* 1992; *Crawford and Hay,* 1993]. This approach minimizes the acoustic response (essentially concentration) to the <*f*>. For frequencies common to ADCPs (300-2000 kHz) in environments dominated by silt/clay size particles there is no variation in <*f*> among frequencies, so the method is only suitable for sand suspensions.

The coupled method uses iterations that determine concentration and particle diameter simultaneously by computing α_s and k_s theoretically [*Thorne et al.,* 2007; *Thorne and Hurther,* 2014]. Previous applications of this coupled implicit method [e.g. *Thorne et al.*, 2011; *Wilson and Hay*, 2015] have not included viscous attenuation which limits its application to sand suspensions, however the addition of viscous attenuation should make it appropriate for all conditions as it includes all factors that cause attenuation loss and scattering for all grain sizes.

Moore et al. [2013] developed a decoupled method, adapted from *Crawford and Hay* [1993] that is more suitable for settings dominated by silt/clay sediments, but the minimization among frequencies is accomplished using in-situ attenuation coefficients rather than <*f*>. In-situ attenuation is computed by the linear regression between acoustic backscatter that accounts for all parameters except sediment attenuation and distance from the transducer [*Topping et al.,* 2007; *Moate and Thorne,* 2009; *Wright et al.,* 2010]. *Moore et al.* [2013] assumed that the attenuation coefficient $<\zeta_{total}>$ is constant, which limits its application to settings without substantial variation in the GSD or time periods when this assumption can be satisfied. The method is also limited to high concentration conditions (10^2-10^4 mg/L) because it requires a reliable estimate of in-situ attenuation. In rivers with low concentrations (i.e. <75 mg/L) in-situ attenuation calculated from the acoustic profiles has been shown to incur error from fluctuations in acoustic signals that represent variability in *M* or D_g across the channel [*Chapter 2*].

To work around the intense computational time of the implicit methods, *Lee and Hanes* [1995] modified Equation 4.4 into an explicit form. The explicit method utilizes the natural logarithm of Equation 4.4:

$$\ln(M) = 2\ln(P_{rms}T_v R\psi) + 4\alpha_f r - 2\ln(k_s k_t) + 2\ln(r) + 4\int_0^r \langle\zeta_{total}\rangle M dr. \qquad (4.6)$$

This equation can be applied to acoustic systems that do not apply a time-varied gain, and therefore if k_t does not change with range, its derivative with respect to range is zero. Differentiation of Equation 4.6 leads to a Bernoulli-type, nonlinear, differential equation, which allows -- through substitution and integration -- the removal of concentration from the right-hand-side of Equation 4.6 [*Lee and Hanes,* 1995; *Thorne and Hanes,* 2002]. The explicit method has the advantage of substantially quicker computation time when compared to the implicit inversion, but has the same limitation as the implicit inversion in that error propagates with distance from the transducer [*Thorne et al.,* 2011]. To determine particle size, the explicit method can be used in both the coupled and decoupled fashion, similar to the implicit method. *Thosteson and Hanes* [1998] describe a multi-frequency approach that uses the coupled explicit method to minimize *M* amongst frequencies using Equation 4.6 to determine both particle size and concentration (simultaneously) as a function of distance from the transducer.

Additionally, *Topping and Wright* [2016] present a dual frequency approach that computes silt and clay concentration, sand concentration, and sand median grain size. Two fundamental assumptions are invoked: 1) silt and clay dominates attenuation and 2) sand dominates backscatter. Similar to *Moore et al.* [2013], their method uses linear regression to estimate the in-situ attenuation, which is in turn calibrated to silt and clay concentration. For sand concentration and median particle size, a "base" calibration is developed for each frequency for a narrow range of particle sizes (e.g. the median particle size as measured at a given site). To compute sand concentration and particle size for a given measured backscatter, the theoretical target strength for a given size and base calibration are used iteratively to determine the particle size that minimizes the difference in sand concentration between the two frequencies. In addition, methods are presented for making corrections for conditions when silt and clay contribute to backscatter, which can have a significant effect on the results. The method is particularly suited to sand-bedded rivers where silt and clay transport (washload) is somewhat decoupled from sand transport. Additionally, their method requires a reliable estimate of in-situ attenuation, which limits the application to high concentration conditions (10^2-10^4 mg/L).

Here, I apply the coupled explicit method of *Thosteson and Hanes* [1998] and the coupled implicit methods of *Thorne and Hurther* [2014], which builds on the method of *Thorne et al.*, [2007]. I include viscous attenuation to the method so that it can be applied to settings with a wide grain size distribution that includes substantial silt/clay. I do not apply the decoupled implicit method of *Crawford and Hay* [1993] because it is only applicable to sand sized suspensions. I also elected not to test the *Moore et al.* [2013] or *Topping and Wright* [2016] because both rely heavily on reliable estimates of in-situ attenuation, which *Chapter 2* showed is problematic low concentration settings using the same data set presented herein. This work is novel for five reasons: 1) This is the first application of the complete multi-frequency inversion using an ADCP, 2) The multi-frequency inversions are adapted to include viscous attenuation, 3) A method is developed to predict the standard deviation of the grain size distribution, 4) Instrument constants critical to the acoustic inversions for ADCPs are explored and 5) The multi-frequency inversions are tested over a three-year period using direct samples within the acoustic beams in the field.

4.3. Physical observations and field site

Field observations were made on the Fraser River at Mission, British Columbia, 240 m upstream of a Water Survey of Canada (WSC) gauging station (no. 08MH024). Mission, BC is ~85 km from the river mouth at the Strait of Georgia and 15 km downstream of the gravel-sand transition [*Venditti and Church*, 2014]. Here, the Fraser is confined to a single ~550 m wide channel carrying runoff from the 228,000 km^2 basin. This provides an ideal location to measure the input of flow and sediment to the Fraser Delta and Estuary [c.f. *McLean et al*., 1999]. The runoff pattern is dominated annually by the spring snowmelt, initiating a freshet hydrograph beginning in April and ending in August/September. Peak flows typically occur in June. The mean flow at Mission from 1983 to 2013 was 3183 m^3/s and the mean annual flood was 9534 m^3/s. Flow at Mission is influenced by a tidal signal. During low flow periods, significant stage variation occurs as tidal forces create a backwater effect, but the saline wedge only penetrates ~30 km upstream of the ocean at low flows and a few km at high flows [see review in *Dashtgard et al.*, 2012]. At high flow, tidal stage variations are minor but velocity variations remain in the signal.

4.3.1. Acoustic instrument setup

Three horizontally oriented acoustic Doppler current profilers (ChannelMaster™ H-ADCPs, Teledyne RDI, USA) were mounted on the Mission Harbour Authority dock just upstream of the Mission railway bridge. The three ADCPs were mounted in a horizontal array, separated by 77 cm. The instruments have acoustic frequencies of 307, 614 and 1218 kHz, nominally 300, 600 and 1200 kHz. Each ADCP has two beams with a 20° angle from center. One-way beam spreading is 1.5° for the 600 and 1200 kHz and 2.2° for the 300 kHz. Care was taken during installation to reduce the pitch and tilt of the instruments to within ±0.1 degrees from zero. ADCPs were set to collect data over one minute with a one-minute rest before the next ADCP started collection, creating a 6-minute interval for all ADCPs. Ensemble averaging was done over 100 pings per minute. Instruments were set in low-bandwidth mode to allow for high resolution and minimal noise at a cost of maximum distance from the transducer.

The ADCPs collect data in 128 bins across the channel. The spacing of the bins and the distance across the channel over which measurements are obtained depends

on the instrument. The 300 kHz instrument has 2 m bins and a 2 m blanking distance, so it nominally measures 258 m across the channel. The 600 kHz instrument has 0.5 m bins and a blanking distance of 2 m, so it measures 66 m across the channel. The 1200 kHz instrument has 0.25 m bins and a blanking distance of 2 m, so it measures 34 m across the channel. The practical range of the instruments is limited to the shortest distance from the transducer when using a multi-frequency application, which in this setup is the 1200 kHz ADCP. Though the maximum distance from the transducer is 34 m, *Chapter 2* shows that distance from the transducer is further limited to the location of the noise floor. The 600 and 300 kHz ADCP profiles were linearly interpolated and mapped to the 1200 kHz range bins. Acoustic backscatter data were recorded from 2012 to 2014, with periods when data were not collected due to instrument loss of power or cleaning.

4.3.2. Physical sediment observations

The physical sediment observations described in this paper were previously reported in *Chapter 2*. Samples were collected between 2012-2014 using a USGS P-63 sampler at locations ranging from 6-250 m from the ADCPs. Here I present only samples collected within 25 m of the ADCPs. Samples were collected at the elevation of the ADCP based on a known distance below the water surface for a given water level measured at WSC gauging station 08MH024, 240 meters downstream of the ADCP array, and are referred to as “in-beam” samples. The in-beam samples were run through a LISST-100 (Sequoia Scientific, USA) laser particle-size analyzer using a random shape model which provides volumetric GSD in 32 logarithmically-spaced bins from 2-356 microns, then filtered to obtain mass concentration.

In order to calculate the calibration parameter β, I needed to calculate theoretical attenuation as accurately as possible. To this end, I used a modified USGS P-61 sampler [*Chapter 2*] to collect a larger amount of suspended sediment (~5g) than was possible with the P-63. The larger samples were collected over 4-hour periods at distances of 18 and 48 m from the ADCP array on June 19, 2014 at a discharge of 10,000 m^3/s and July 22, 2014 at a discharge of 5,000 m^3/s. The samples were run through a Beckman Coulter Laser Diffraction Particle Size Analyzer (LS-PSA; model LS 13 320) which provides a wider effective particle diameter range of 0.4-2000 microns, which ensures that the fine tail of our β calibration samples is well represented.

On the basis of sediment samples obtained from 2012-2014, *Chapter 2* showed that concentrations ranged from 15 to 350 mg/L with a mean of 90 mg/L. The geometric mean particle diameter (D_g) ranged from 14 to 70 μm with a mean of 31 μm. The geometric standard deviation (σ_g) ranged from 1.9 to 3.8 with a mean of 2.55. The LISST GSDs show that the majority are lognormal (Figure 4.1). The LISST GSDs also show that throughout the freshet, subdominant modes occur in the coarser end of the GSD.

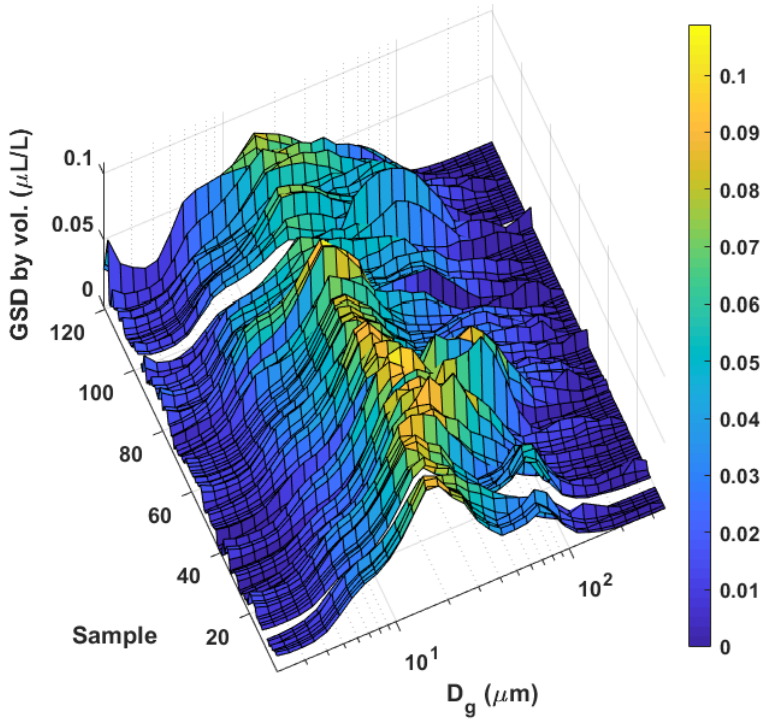

Figure 4.1 Grain size distributions for all 121 bottle samples collected from 2012-2014.

Figure 4.2 shows GSD characteristics over a range of flows, in addition to the large sediment sample GSDs. As flows change from 2000 m^3/s to peak flow around 12,000 m^3/s, D_g changes from local, coarse suspended bed material to finer silt/clay material during mid flows, finally becoming coarser at the highest flows (Figure 4.2a). Additionally, with increasing flows σ_g broadens (Figure 4.2b). Though concentration increases as a function of flow (Figure 4.2c), hydrograph classification (Low< 3500 m^3/s; 9000 m^3/s < Peak) shows hysteretic behavior between the rising and peak flows. The LS GSDs from the larger samples obtained with the modified p-61 (Figure 4.2d), show a broad distribution with a median diameter of ~11.1 microns and a geometric standard

deviation of 4.0. Additionally, they show that the LS GSD has a particle diameter breadth of 0.375-310 µm, which is broader than the size range resolved by the LISST.

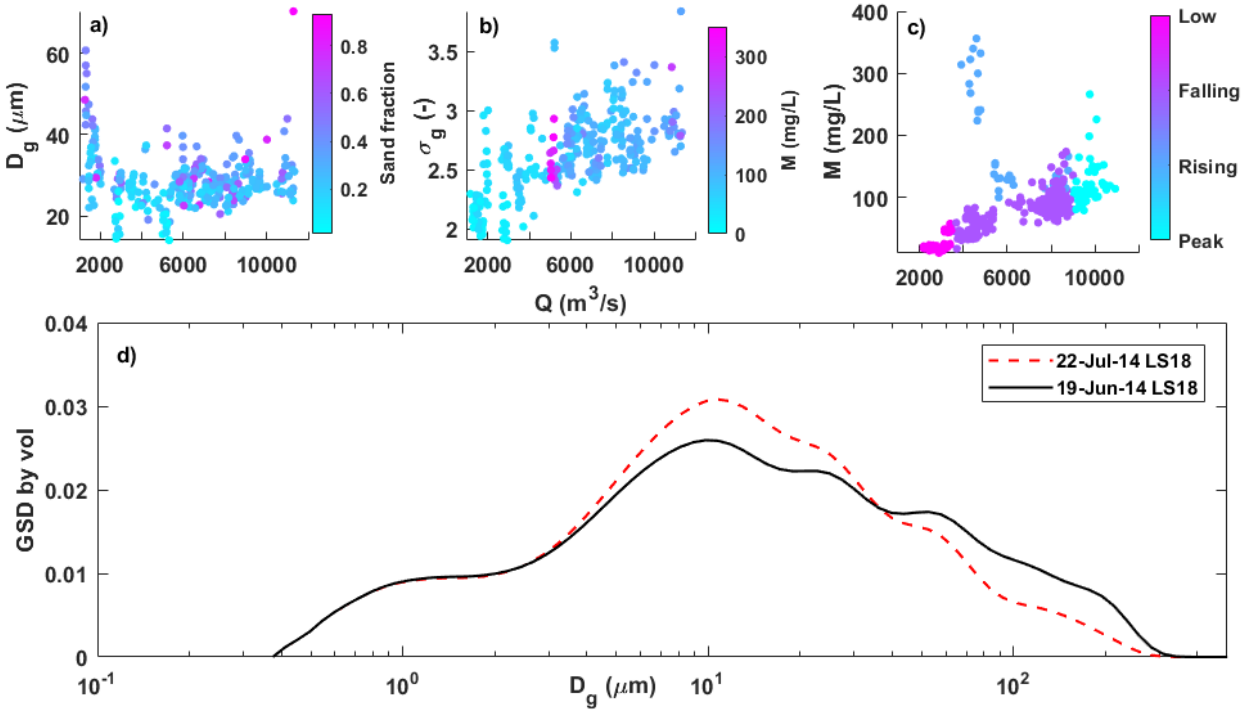

Figure 4.2. Results from all 298 processed suspended sediment samples showing (a) geometric mean particle diameter and sand fraction (colorplot), (b) the geometric standard deviation and M (colorplot), and (c) SSC and hydrograph classification (colorplot), all as a function of flow. (d) Grain size distribution for samples collected with the modified P-61 sediment sampler and run through a LS 13 320 (LS).

4.3.3. Acoustic Data Filter

In general, and especially during low flows, raw acoustic data in counts were noisy due to ambient noise. Prior to being converted to acoustic intensity in decibels, I_{db} (Appendix A4.1), data were filtered with single spectral analysis (SSA), which is similar to principal component analysis, but in the time domain [*Vautard and Ghil*, 1989; *Vautard et. al.*, 1992; *Plaut and Vautard*, 1993]. The SSA method is a version developed by *Vautard et. al.* [1992] and modified by *Schoellhamer* [2001] that accounts for missing data. For our analysis, I use a maximum lag of 120 (12 hr) to compute a Toeplitz matrix and five principal components to deconstruct the signal. To reconstruct the time-series I use the first four principal components, which account for approximately 94% of the

variance for bins within the applied range of the ADCPs, and retain only the dominant frequencies of the signal while discarding some of the higher-frequency noise.

4.4. Testing inversion methods

In order to examine the effectiveness of the coupled implicit acoustic inversion techniques with an ADCP, I apply the method described by *Thorne and Hurther* [2014], termed “IM” methods. I also apply the *Thosteson and Hanes* [1998] method to examine the effectiveness of the coupled explicit method, termed “EX” method. I systematically test both methods by first varying one variable, then two, and finally three. Because *M* is being minimized by the coefficient of variation between all three frequencies, the process outlined is the same for both inversion methods, but the computation of *M* differs. In the first set of tests (single-variable), I hold the geometric mean particle diameter (D_g) and geometric standard deviation (σ_g) constant while calculating the mass concentration (*M*). This procedure assumes that the GSD characteristics are known. In the second set of tests (dual-variable), I hold σ_g constant while solving for D_g and *M*.

The first step in the procedure is to define a range of mean particle diameter which encompasses the full range of suspended bed material and washload. Here I use D_g values from 0.1 to 1000 microns. Next, for every mean particle diameter, D_g, from the predetermined range, I use a hypothetical GSD (by number) with a log-normal distribution with a predetermined σ_g. The GSD is used to compute sediment attenuation and backscatter form function, which are then used in the computation of *M* for every D_g. Particle diameter and mass concentration are estimated from the minimization of the coefficient of variation (*CV*) computed as:

$$\mathrm{CV} = \frac{\sigma_{\overline{M_{J,\iota}}}}{\overline{M_{J,\iota}}} \tag{4.7}$$

where the overbar represents the mean of all three frequencies and σ_M is the standard deviation of the mean concentration. The resulting GSD is used to compute the final theoretical sediment attenuation (Appendix 4.3), the backscattering parameter (Appendix 4.2), and *M* for each frequency.

In the third set of tests (tri-variable), I vary D_g, σ_g, and *M*. In the tri-variable test, I first find D_g and $M(D_g)$ exactly as in the dual-variable test described above, then for σ_g I

undertake a sensitivity analysis by varying σ_g between 1.25 and 5.5 (in 0.25 unit increments) in the computation of *M* for the 600 kHz to find the lowest value of the coefficient of variation of *M*. Once σ_g is determined at the minimization of CV, *M* is recomputed for the 1200 and 300 kHz frequencies using σ_g and D_g in the computation of sediment attenuation and the backscattering parameter. The choice of the 600 kHz is due to the fact that estimated values of *M* fall between the values from 1200 and 300 kHz frequencies.

4.4.1. Implicit inversion (IM)

I compute an mass concentration using Equation 4.4, assuming sediment attenuation is negligible in the first range bin. Concentration is computed at every distance from the transducer--for each frequency--for each potential geometric mean particle size and GSD derived sediment attenuation (α_s) and backscattering parameter (k_s). Because sediment attenuation is dependent on concentration, I iterate attenuation and mass concentration, after the first range bin, until convergence is satisfied [*Thorne and Hurther*, 2014]. The convergence criterion that terminates the iteration is arbitrarily set as 1% relative error.

4.4.2. Explicit inversion (EX)

In the explicit method, Equation 4.4 is also used to compute an initial estimate of concentration for a range of particle diameter, but it is computed only for the range bin nearest to the ADCP, but outside the nearfield (~2.5 m from the ADCPs). The initial concentration in the first range bin is then iterated to account for sediment attenuation. Following the criteria laid out in *Thosteson and Hanes* [1998], I utilize Equation 4.6 which allows concentration to be computed as:

$$M_{o,j}(r) = \frac{[(P_{rms} r\psi)^2 / k_s^2]}{\gamma_{j,0-I_j}} e^{4\alpha_f r} \tag{4.8}$$

$$\gamma_{j,0} = \frac{(P_{rms,j,o} r_o \psi)^2}{k_{s,o}^2 M_{o,j}} \tag{4.9}$$

$$I_j(r) = 2\sum_{n=1}^{n=N}\left(\zeta_{total}\frac{[(P_{rms,j,n}r_n\psi)^2}{k_{s,n}^2}\exp\left(4\alpha_f r_n\right) + \zeta_{total}\frac{[(P_{rms,j,n-1}r_{n-1}\psi)^2}{k_{s,n-1}^2}\exp\left(4\alpha_f r_{n-1}\right)\right)\times(r_n - r_{n-1}) \quad (4.10)$$

where γ is the integration constant, n is the range bin, N is the total number of range bins, and the subscript o indicates the bin nearest to the ADCPs. The discrete form of the integral, I, and the final estimate of concentration are both a function of range. As with the implicit method, concentration and particle size are determined by the minimum of the coefficient of variation between all frequencies.

4.4.3. Verification of the inversion method

For both the explicit and implicit methods, the minimization of the acoustically derived concentration is quantified with the coefficient of variation between the three frequencies. Here I illustrate the process of determining all variables in the tri-variable explicit method (though I could have used the implicit method as well) for a sample collected on June 19, 2014. The advantage of using this date is that I have two sets of GSDs (one from the LISST and one from the LS), which allows for a thorough examination of the observed D_g and σ_g. The value of *CV* can itself vary with particle size, standard deviation and range. Additionally, it is expected that some variation will be inherent in these tests as the instruments are not exactly collocated nor do they measure at exactly the same time.

The minimization between frequencies is central to the idea that when the ADCPs are collocated, the number of particles in the ensonified volume should be the same, and therefore the variance should be small. Our setup doesn't permit ensonification of the exact same volume of water, but the close proximity of the instruments (particularly with respect to distance above the bed) and the large, overlapping ensonified volumes should reduce variation. This challenging aspect is an active component of this research.

Figure 4.3 shows how the minimization is computed over the range of D_g and σ_g for a single sample. Figure 4.3a shows the computation of M (Eq. 4.4) for all three frequencies at all range bins (hence the stacked, broad lines). Figure 4.3b shows CV

computed at a range of 18 m for all three frequencies, along with the measured value from the in-beam sample GSD processed by the LISST. The result shows a clear minimization point at 22 μm, which is close to the measured D_g value of 23 μm. The GSD from the LS (Figure 4.3d) gave D_g equal to 13 μm, suggesting that the particle diameter may be slightly smaller. Figure 4.3c shows CV computed for a range of σ_g as a function of range from the ADCP. The minimization trough suggests that σ_g ranges from 2 to 3, which falls around the value of 2.8 given by the LISST and less than the σ_g of 4.3 given by the broader LS GSD.

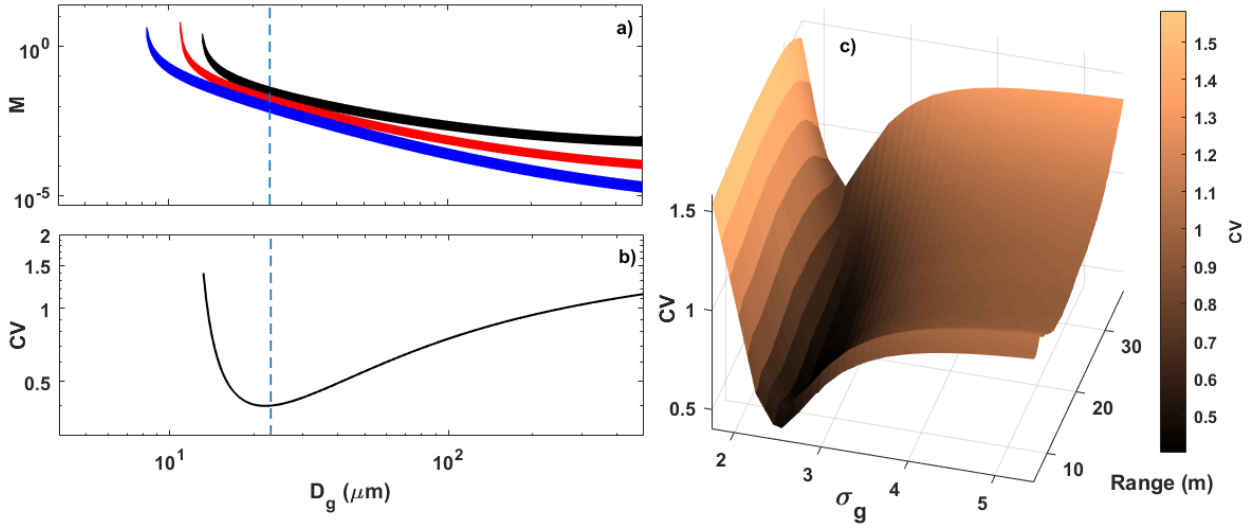

Figure 4.3. Acoustic inversion using the EX method for determining D_g and σ_g on June 19, 2014. (a) Computation of Eq. 4.4 using the set range of D_g for the 1200 (black), 600(red), and 300 (blue) kHz ADCPs for all range bins. (b) CV computed using Eq. 4.6 18 meters from the ADCPs (IB18). The vertical dashed blue line represents the measured D_g from the LISST100 on the same date at the same location, which was 11.5 μm. (c) CV computed for the determination of σ_g. The measured σ_g was 2.76.

To test the precision and accuracy of the two methods and number of variables used with respect to the measured (or observed) *M*, I must quantify the error between measured and acoustically derived (or predicted) values. I use the mean absolute error (MAE) and the magnitude of the deviation (MAG) to quantify the results. The mean absolute error can be defined as:

$$MAE = N^{-1}\sum_{1}^{N}|e_k| \tag{4.11}$$

where e_k= acoustically derived *M*- measured *M* associated with the k^{th} observation and N is the number of observations. To quantify the magnitude of the error with respect to over or underestimation, I calculate the magnitude as:

$$MAG = log_{10}\big(Median(e_{r,k})\big) \tag{4.12}$$

where $e_{r,k}$= acoustically derived *M*/measured *M*. The benefit of using MAG is that when in logarithmic units it directly quantifies the distance of the central tendency of predicted values to the measured values by the number of orders of magnitude, without being influenced by some of the larger values (i.e. outliers). Lastly, to quantify the bias associated with the GSD standard deviation, I use the Spearman rank coefficient to correlate between $e_{r,k}$ and LISST measured σ_g, which I denote $\rho_{s,e/\sigma}$. This non-parametric analysis provides insight into the influence that σ_g has on the deviation of the acoustically derived values from *M* measurements, while being less sensitive to outliers than the Pearson correlation coefficient. A strong rank correlation indicates a bias is likely due to LISST measured σ_g, while the negative or positive correlation indicates whether the bias is indirect or not. I evaluate the correlations at the 95% confidence level. If the p-value is > 0.05, then no correlation exists and there is likely no influence of σ_g on acoustically derived *M*.

4.5. Parameter calibration and verification

4.5.1. Calibration of β parameter

The calibration of the voltage transfer function (T_v) of the ADCP and the transducer receive sensitivity (*R),* which I lump into one variable, β, can be done using standard spherical targets or with a hydrophone in-situ or through the back-calculation described by *Betteridge et. al.* [2008]. Using “off-the-shelf” ADCPs, in-situ measurements and lab-based tests are difficult because of the scale of the ensonified volume. So, I follow *Betteridge et. al.* [2008], where I simplify and re-arrange Equation 4.1, using measured GSD’s and mass concentration to solve:

$$\beta = \frac{P_{rms}\psi r}{k_s M^{1/2}} e^{4r(\alpha_f+\alpha_s)} \tag{4.13}$$

Sediment attenuation and k_s are computed from LISST-measured GSDs, while mass concentration, M (kg/m^3), comes from the bottle samples. I set ψ=1, which accounts for the departure from spherical spreading in the near-field, because the first bin used is outside the near-field.

Figure 4.4 (a-c) show how β varies with range for each frequency, along with the mean value, excluding the outliers that exceed the mean by 1.5σ, where σ is the standard deviation. I use only β values within 20 m and between 50 and 200 mg/L to prevent poor estimates due to environmental conditions. The upper limit excludes samples taken over the first flush of sediment from the drainage basin in April 2014 which range in M from 200 to 350 mg/L (Figure 4.2c). These samples have a high percentage of clay/silt material derived from fine sediment accumulated over the winter season and entrained when the flows initially start to rise during the annual snow melt freshet. It is likely that GSDs during this time period are not well resolved by the LISST. The lower limit excludes the use of acoustic signals that incur a relatively large amount of noise due to variability in M or D_g within the ensonified volume [*Haught et al.,* 2017].

Mean values of β are $1.6\text{x}10^{-3}$ ($\pm 0.79\text{x}10^{-3}$), $1.5\text{x}10^{-3}$ ($\pm 4.5\text{x}10^{-3}$), and $2.0\text{x}10^{-2}$ ($\pm 1.2\text{x}10^{-2}$) for the 1200, 600 and 300 kHz frequencies, respectively. All three frequencies show variability within an order of magnitude from the mean. The large volume GSDs from the LS instrument (red asterisks) fall close to the mean β values, suggesting an accurate estimate when using LISST derived GSDs that arise from a narrower range of sediment size used to compute α_s and k_s.

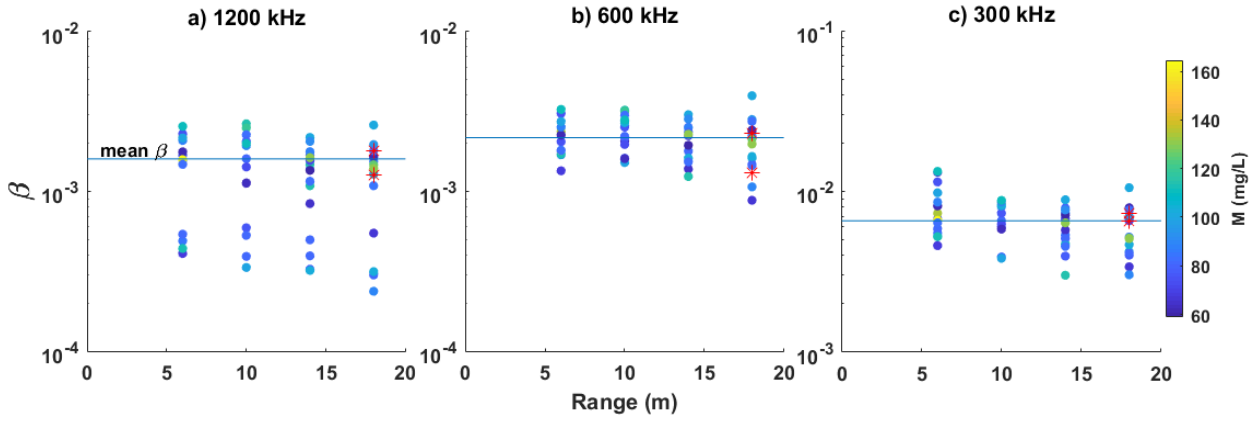

Figure 4.4. Instrument constant, β, for the (a) 1200, (b) 600, and (c) 300 kHz instruments, using the LISST GSD samples to the compute the mean value. The red asterisk is β computed using the large sample GSDs from the LS instrument.

The variability in β calibration results requires an evaluation of its influence on the calculation of concentration. To test the sensitivity of β as a function of mass concentration I computed *M* for all three frequencies over a range of β values (±3σ) on a day where I have both LS and LISST GSDs (June 19, 2014; Figure 4.2d). To compute *M*, I use the IM method, though either method could be used. Values of *M* fall within two orders of magnitude, suggesting that *M* is a sensitive parameter to changes in β (Figure 4.5a). Additionally, I see that fitted lines cross the measured *M* (Figure 4.5a) and D_g (Figure 4.5b) prior to the estimate of β derived from Equation 4.13 and shown in Figure 4.4. It is important to note that this was done for only one day, yet suggests that the mean β may be overestimated.

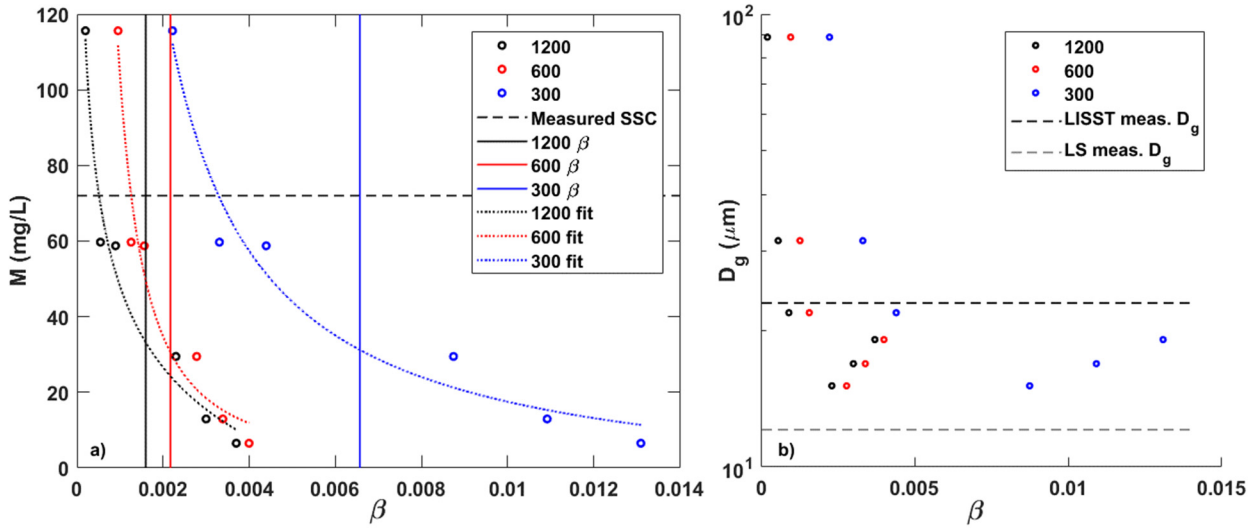

Figure 4.5. Variability in (a) frequency average M (Eq. 4.4) and (b) particle diameter as a function of varying β ±3σ of the mean. Vertical line represents mean β used in the inversion (Figure 4.4) while horizontal dashed lines are measured M (a) and D_g (b) from the LS GSD on June 19, 2014 18 m from the transducer.

4.5.2. Ensemble averaged Form Function

A check to see where the form function lines up with theoretical values from measured GSDs is necessary to validate our inversion. I simplify and re-arrange Equation 4.1 following methods outlined in *Moate and Thorne* [2013], using measured concentration and LISST GSD derived sediment attenuation with mean β values to define k_t:

$$\langle f \rangle = \frac{P_{rms}\psi r\sqrt{\langle 1/2D \rangle \rho}}{k_t M^{1/2}} e^{2r\alpha} \tag{4.14}$$

where f is related to k_s by Equation A4.3 in Appendix 4.2.

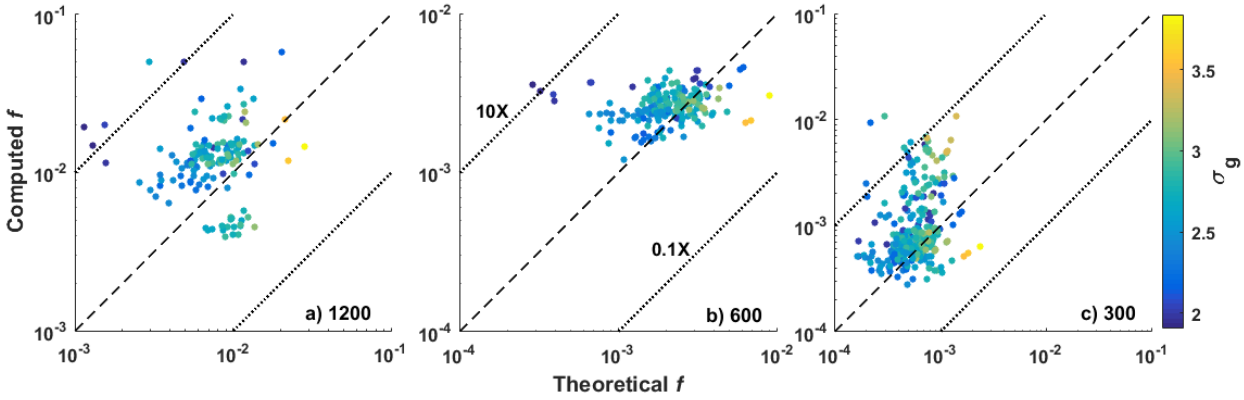

Figure 4.6. Computation of ensemble form function, f, from Equation 4.14 compared to theoretical ensemble form function, Eq. A4.4, computed from measured GSDs. The color bar shows LISST measured σ_g.

Figure 4.6 shows that computed ensemble form function values fall around the line of unity for all three frequencies, all falling within an order of magnitude and relatively tightly bound to the line of unity. The 600 kHz results are best. The 1200 and 300 kHz frequency results fall within two orders of magnitude with the 300 kHz ADCP showing the tightest grouping between the two. Though there appears to be some trend in geometric standard deviation in the results, it is not unexpected that ensemble form function would increase with increasing σ_g.

4.6. Multi-frequency acoustic inversion results

4.6.1. Single-variable test

For the single-variable test I hold D_g and σ_g constant at values of 29 μm and 2.6, respectively. The single-variable inversion produces an estimate of concentration for each frequency at the respective sampling range bin. Figure 4.7 shows estimated *M* values at the respective sampling distance using the IM coupled method and the EX coupled method. The two methods produce similar results. The best results are obtained from the IM method using the 1200 kHz frequency, followed by the 600 and 300 kHz ADCPs. Table 4.1 gives the statistical results for all methods with regards to

measured versus acoustically derived *M*. MAE and MAG values show that the 1200 has the least error with respect to the line of unity. MAG values show that acoustically derived *M* is underestimated with respect to measured *M* by -0.5 to -0.9. A bias is suggested by Spearman rank coefficients that are positive and statistically significant with respect to the measured σ_g, in that, as the standard deviation decreases, acoustically derived *M* moves away from the line of unity. When varying the constant σ_g between the full range of LISST derived values (Figure 4.2b; 1.9-3.8), *M* changes from -55% to 340% for the IM method, while ranging from -50% to 280% for the EX method. When varying the constant D_g between the full range of LISST derived values (Figure 4.1a; 14-70 µm), *M* changes from -90% to 490% for the IM method, while ranging from -82% to 480% for the EX method.

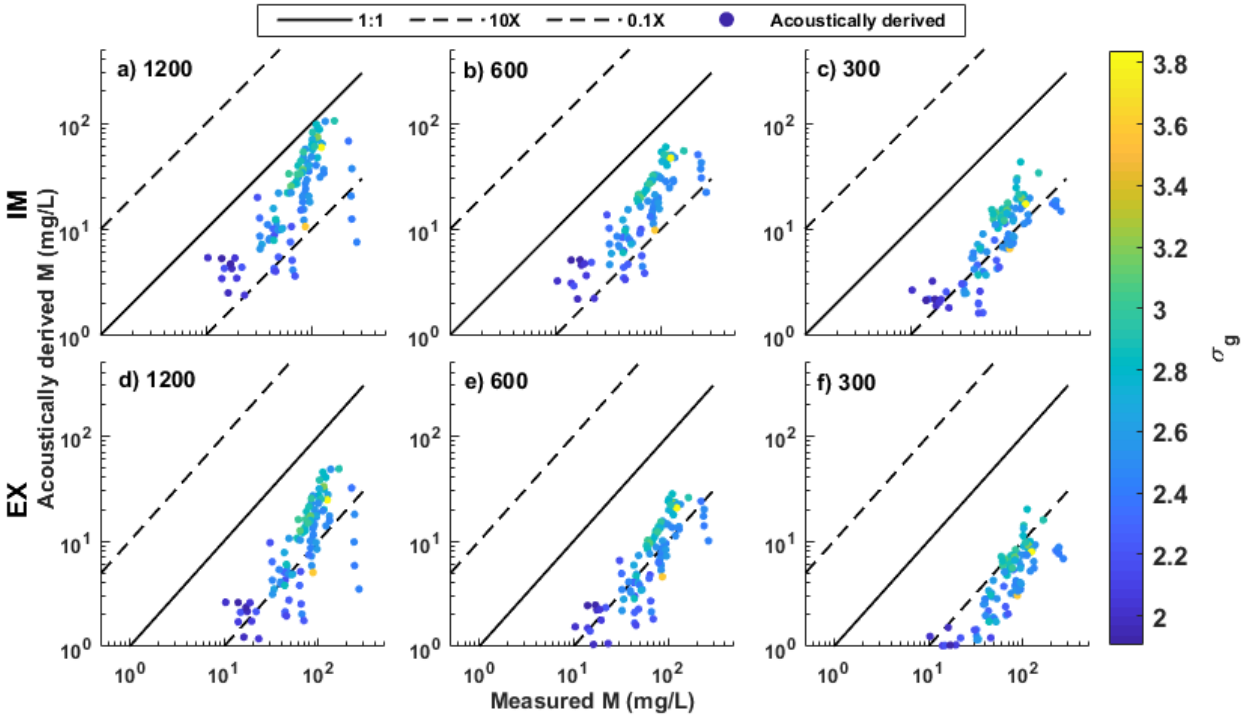

Figure 4.7. Acoustically derived concentration with a constant D_g and σ_g using the IM method (top) and the EX method (bottom) for the 1200, 600, and 300 kHz ADCPs.

The EX method gives similar results to that of the IM method, but with increased error and therefore larger MAE values. MAG values range from -0.9 to -1.2, showing that median acoustic derived values are over an order of magnitude less than measured *M*, which is also seen in Figure 4.7f. Spearman rank correlation reveals a bias with respect to the measured σ_g also exists for the EX method.

Overall, the IM method performed better than that of the EX method. The clear bias that exists suggests that assuming the GSD is constant in both mean value and breadth does influence the results and therefore needs to be accounted for in the inversion. Additionally, given the large difference in computation time between the methods, it shows that the use of the more efficient EX method is likely superior in conditions where the GSD can be assumed constant.

Table 4.1 Statistical evaluation of acoustically derived M, with respect to measured M.

Acoustic Inversion Statistics for Suspended Sediment Concentrations												
Method	**IM**											
Analysis	**Single**				**Dual**				**Tri**			
Frequency	MAE	MAG	$\rho_{s,e/\sigma}$	pval	MAE	MAG	$\rho_{s,e/\sigma}$	pval	MAE	MAG	$\rho_{s,e/\sigma}$	pval
1200	50.65	-0.54	0.54	$7.8x^{-9}$	35.78	0.004	0.23	$2.3x10^{-2}$	52.20	-0.33	0.29	$4.0x10^{-3}$
600	58.01	-0.65	0.52	$3.4x10^{-8}$	33.81	-0.09	0.05	$6.1x10^{-1}$	35.16	-0.09	0.21	$3.2x10^{-2}$
300	68.18	-0.88	0.49	$2.2x10^{-7}$	48.28	-0.33	0.08	$4.2x10^{-1}$	64.67	-0.98	0.22	$3.0x10^{-2}$
	EX											
Analysis	**Single**				**Dual**				**Tri**			
Frequency	MAE	MAG	$\rho_{s,e/\sigma}$	pval	MAE	MAG	$\rho_{s,e/\sigma}$	pval	MAE	MAG	$\rho_{s,e/\sigma}$	pval
1200	65.71	-0.85	0.52	$3.3x10^{-8}$	48.41	-0.37	-0.09	$3.8x10^{-1}$	46.19	-0.34	0.076	$4.5x10^{-1}$
600	69.07	-0.97	0.52	$5.3x10^{-8}$	55.27	-0.50	-0.18	$7.6x10^{-2}$	52.83	-0.43	-0.01	$9.1x10^{-1}$
300	73.81	-1.21	0.49	$3.3x10^{-7}$	66.67	-0.78	-0.15	$1.4x10^{-1}$	65.55	-0.70	0.03	$7.6x10^{-1}$

4.6.2. Dual-variable test

When solving for *M* and D_g (and holding σ_g at the same value as the single-variable test), Figure 4.8 shows that the IM and EX methods give different acoustically derived D_g and *M* results relative to measured *M*. Table 4.2 gives the MAE, MAG and correlation results for particle size compared to measured particle size.

The IM method gives MAE values that range from 36-48 for *M*, with the 600 having the smallest values, followed by the 1200 and 300 kHz ADCPs. MAG values range from -0.3 to 0.004, suggesting that acoustic results underestimate measured values, but by no more than a third of an order of magnitude. Spearman rank coefficients show no correlation and therefore no bias exists for the 600 and 300 kHz ADCPs with regards to measured σ_g. The 1200 kHz has a significant Spearman rank coefficient,

albeit weak. When acoustically deriving D_g, the IM method gives a MAE of 14 and a MAG of -0.26 (Table 4.2). Correlation analysis reveals that no significant bias exists between the deviation from measured values and the GSD σ_g.

The EX method gives results for acoustically derived particle size that cluster around the line of unity with a trend that tends to follow the 1:1 line (Figure 4.8), suggesting a better response to changes in measured D_g. This is supported by MAE values for *M* that range from 48-66, which are slightly better than the single variable inversion (Table 4.1). Though better than the single variable inversion, MAE and MAG values are still greater than those of the dual-variable IM inversion. Like the IM method, no significant bias exists with respect to measured GSD σ_g. Particle size shows MAE values of 7.5 and a MAG value of 0.02, with no significant bias (Table 4.2). Figure 4.8 shows that the acoustically derived D_g fall along the line of unity with a better response to increases in measured D_g, which is supported by a MAG value close to zero.

Overall, both dual-variable methods are an improvement over the single-variable method with constant D_g and σ_g. When estimating *M*, the IM method out-performs the EX method, giving lower MAE and MAG values. When estimating D_g, the EX method appears to outperform the IM method, in that the LISST measured observations align better. When varying the constant σ_g between the full range of LISST derived values (Figure 4.2b; 1.9-3.8), *M* changes from -20% to 4% for the IM method, while ranging from -33% to 30% for the EX method. Additionally, when comparing the dual-variable test to the single-variable test (Table 4.1), *M* results tend to center around the line of unity (Figure 4.8), suggesting that this method is improved when introducing an estimate of D_g.

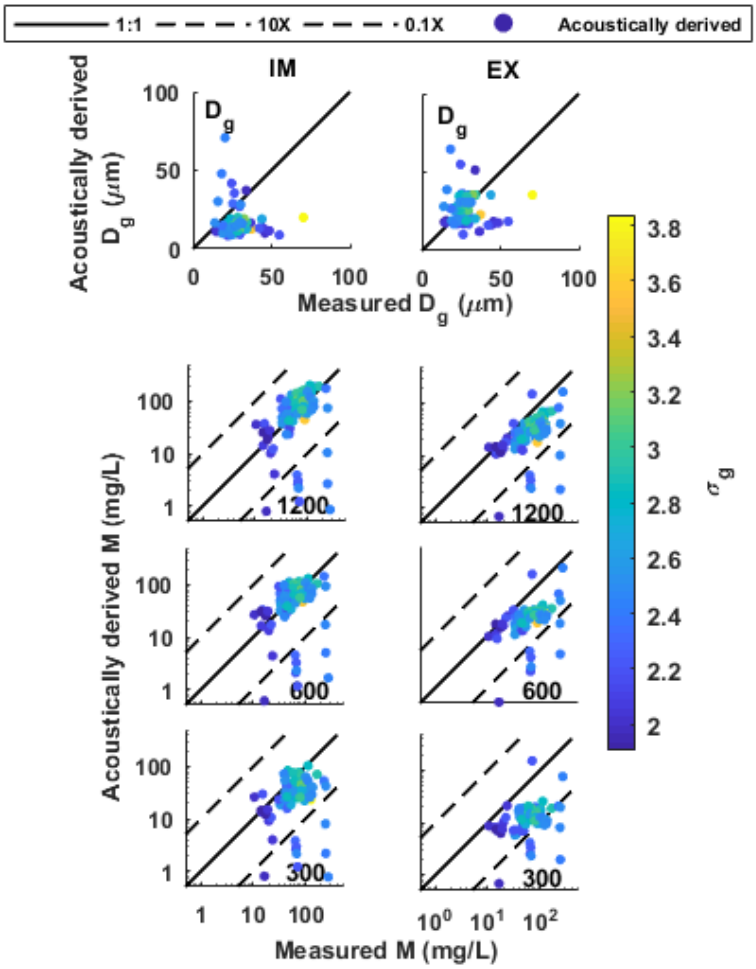

Figure 4.8. Results for the dual-variable inversion showing the acoustically inverted M and D_g compared to measured values.

Table 4.2. Statistics for acoustically derived particle size and GSD standard deviation.

Acoustic Inversion Statistics for Suspended Sediment Size and GSD Standard Deviation								
Method	IM							
Analysis	Dual				Tri			
Parameter	D_g				σ_g			
Statistic	MAE	MAG	$\rho_{s,e/\sigma}$	pval	MAE	MAG	$\rho_{s,e/\sigma}$	pval
Measure	13.96	-0.26	0.01	0.95	0.78	0.11	n/a	n/a
Method	EX							
Analysis	Dual				Tri			
Parameter	D_g				σ_g			
Statistic	MAE	MAG	$\rho_{s,e/\sigma}$	pval	MAE	MAG	$\rho_{s,e/\sigma}$	pval
Measure	7.47	0.02	0.18	6.8×10^{-2}	0.30	1.6×10^{-3}	n/a	n/a

4.6.3. Tri-variable analysis

When varying all three parameters using the IM method, acoustically derived *M* shows more scatter than for the dual-variable inversion (Figure 4.9). MAE values increase to 52 and 65 for the 1200 and 300 kHz ADCPs, respectively (Table 4.1). The 600 kHz shows the best results with a MAE value of 40, which is slightly higher than the dual-variable result. The fact that the 600 kHz is not improved is surprising, given the sensitivity analysis used to find σ_g was conducted using the 600 kHz ADCP. Because of the method used, there is no difference between the results of the dual-variable and tri-variable inversion with regards to D_g. Acoustically derived σ_g fall within a range of 2.5 to 4, with several outliers falling above 4. These estimates are greater than that of the LISST measured σ_g, which is supported by a positive MAG value of 0.8.

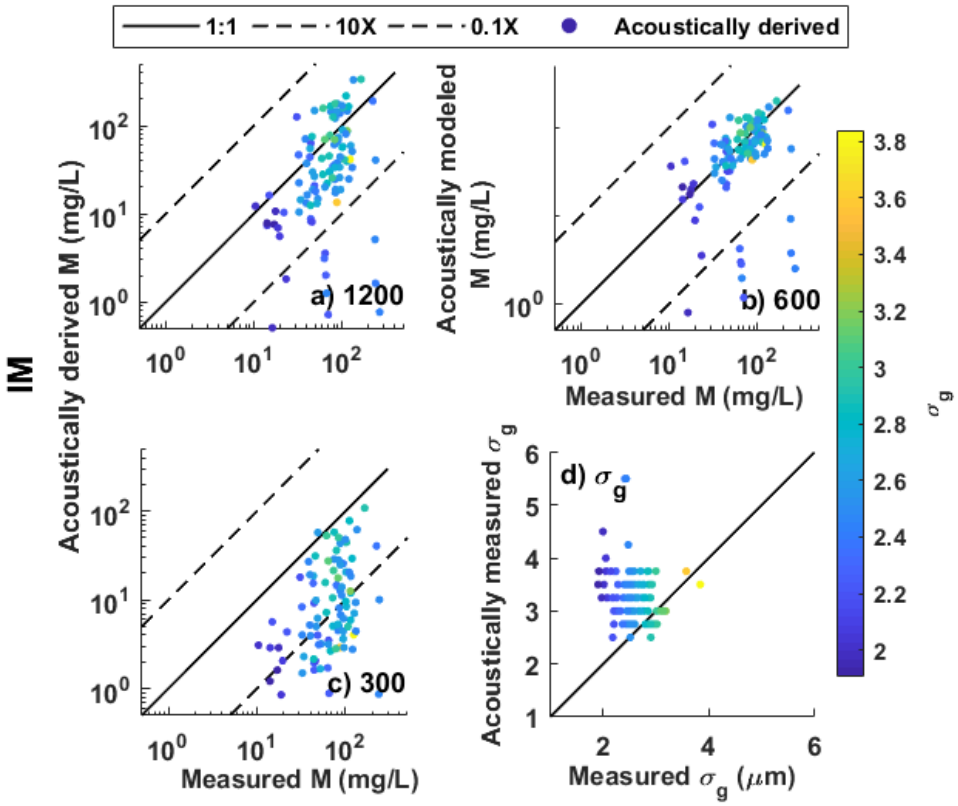

Figure 4.9. Results for the tri-variable inversion showing the acoustically inverted M, and σ_g compared to measured values using the IM method.

The EX method shows *M* values that fall within an order of magnitude of the measure values (MAG= -0.7 to -0.34), with the 1200 kHz giving values that fall closest to the line of unity, followed by the 600 then 300 kHz ADCPs (Figure 4.10). Unlike the IM method, the EX method shows improved MAE (46-65), albeit minimal. Acoustically derived σ_g values are between 2 to 3, which is similar to LISST measured values. Table 4.2 shows MAE and MAG values of 0.3 and 1.6×10^{-3} for σ_g, respectively.

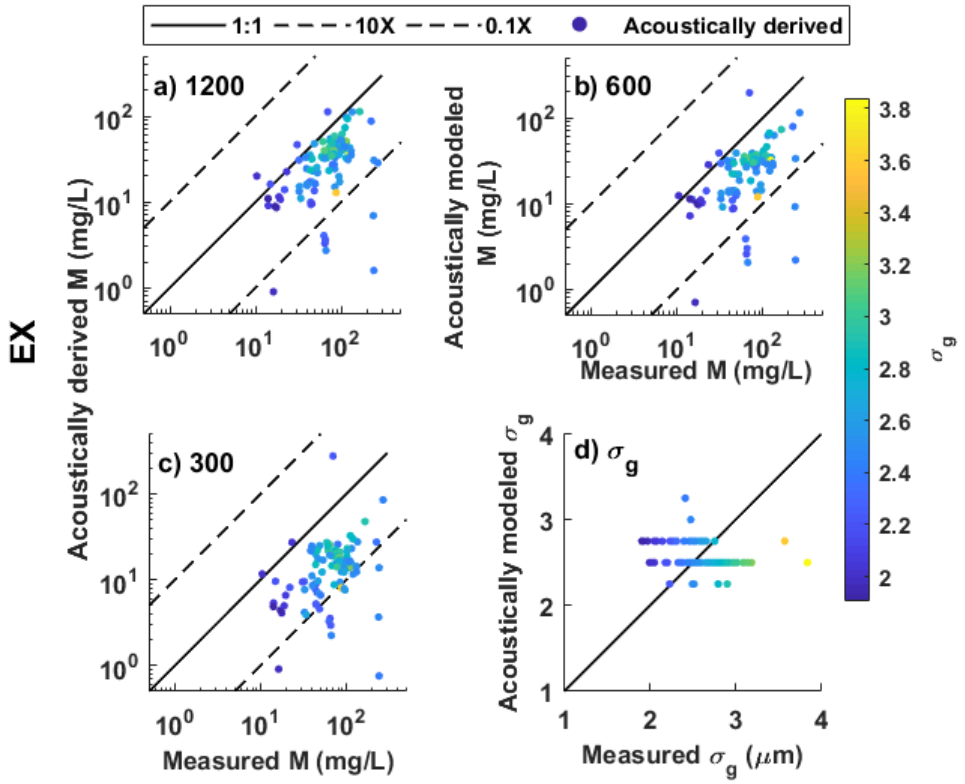

Figure 4.10. Results for the tri-variable inversion showing the acoustically inverted M and σ_g compared to measured values using the EX method.

Overall, when deriving *M*, both tri-variable inversion methods perform worse with respect to the dual-variable method. Though acoustically derived σ_g using the IM method has a larger MAE value than that of the EX method, the striated pattern and significant bias in the EX results suggest that the IM method provides more robust σ_g values. With that said, the increased computational time for the sensitivity analysis with the 600 kHz frequency in the tri-variable tests does not appear to yield substantially improved results, compared to the dual-frequency results.

4.6.4. Time-series of dual variable inversion

In addition to examining the acoustically derived sediment properties on days when I obtained bottle samples, it is possible to calculate a time-series of acoustically derived sediment attenuation, *M* and particle size over the three-year period. Though most of the sediment in the Fraser R. is transported over the freshet, estimating GSD properties during low flow illuminates how well the inversion does in all flow conditions. Because of the long processing times and the lack of improved tri-variable results in

comparison to the dual-variable results, I chose to process the time series for all three years using the dual-variable methods only (IM and EX). Therefore, the parameters of interest are acoustically derived *M* and D_g. Figure 4.11 compares the IM frequency average sediment attenuation, frequency average *M*, and D_g to that of the EX method.

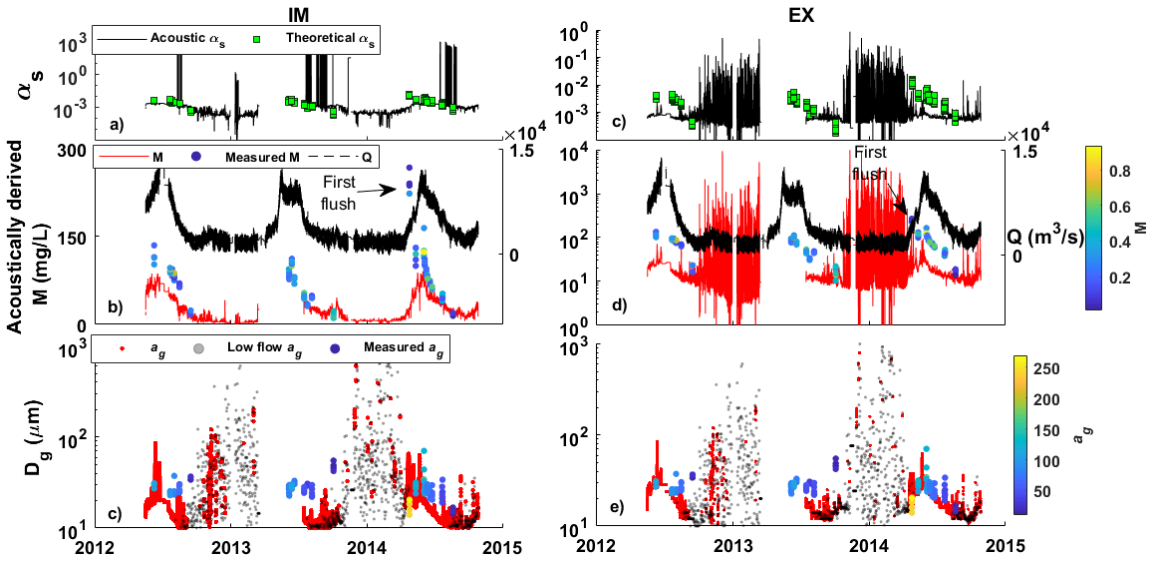

Figure 4.11. Time-series of frequency average sediment attenuation, frequency average M, D_g, for the IM method (a-c) and for the EX method (c-e). Note that D_g is divided by flow velocities greater and less than 0.3 m/s (in c and e).

The IM method gives attenuation values that are within an order of magnitude for most of the three-year period. Figure 4.11a shows that there are also clear spikes (where α_s increases by five to six orders of magnitude) that are unrealistic given our concentrations and GSDs. Also shown are the averages of all frequencies for theoretical attenuation values from bottle samples. Theoretical attenuation values track the acoustically derived α_s well, except for the first flush event in April 2014. This result is also seen in Figure 4.11b when examining the acoustically derived *M*. Sampled concentrations show the large event that had concentration reach ~250-300 mg/L, yet the acoustically derived *M* shows a small increase only. Absent the missed event, the IM method provides good results for *M* that track discharge well. Samples show that even though they are greater than acoustically derived values, they mimic the freshet's rising and falling limbs and show little noise during the low flow periods. Acoustically derived D_g shows results that contain a lot of noise during low flow periods and tend to track better during the freshet. Interestingly, the outlying spikes from attenuation do not align with the D_g spikes.

For the EX method sediment attenuation shows large variability during low flow periods that range over three orders of magnitude. At freshet flows attenuation tends to be underestimated by the acoustic inversion relative to the frequency average theoretical attenuation (Figure 4.11c). Acoustically derived *M* shows more variability during low flow periods with variability in *M* mimicking that of attenuation, likely stemming from the poor α_s estimates. During high flow periods, the values tend to underestimate bottle samples, but track the measurements well. Additionally, the April 2014 first flush shows a better acoustic response, albeit still lower than measured *M*. While the acoustically derived D_g gives values that fall within an order of magnitude at high flows, the range during three low flow periods is on the scale of two orders of magnitude.

Overall, acoustically derived *M* is better represented during all flow conditions by the IM method, although predicted D_g values are noisy at low flow and under predict bottle samples at high flow. Nevertheless, D_g tracks freshet flow conditions well. The low flow variability in D_g is illustrated in Figure 4.12. Though there is a clear delineation between the larger D_g values and those that range between 10-40 μm at 0.3 m/s, it is difficult to infer any process that is occurring during the low flow periods without more in-situ observations. During the low flow periods, when flow velocity locally reverses (i.e. helical flow circulation), several processes that could impact the acoustic signal are increased ambient noise, bubbles from decomposing organic matter, or micro flocculation of clays, silts, and organics in suspension.

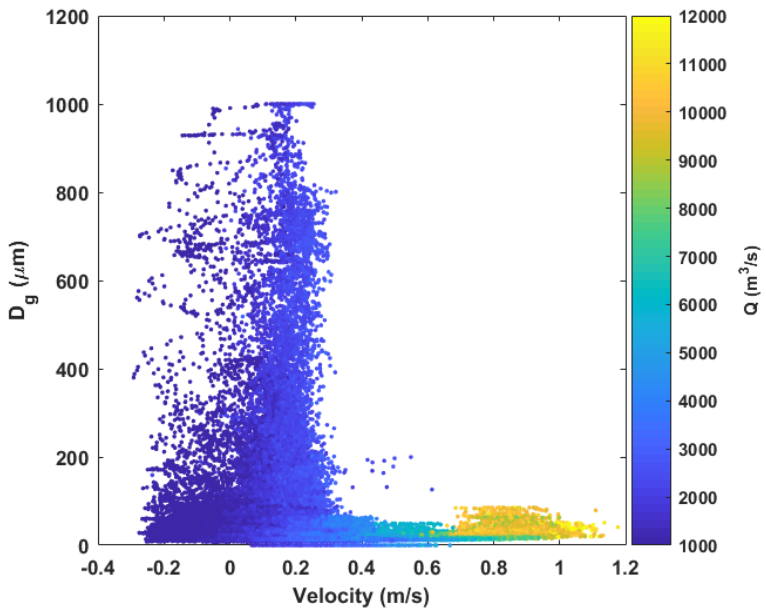

Figure 4.12. Daily average D_g as a function of velocity 15 m from the ADCPs. Colorplot shows channel average discharge

To determine the best method to use in an environment where the sediment source and GSD characteristics change through time, I need to examine the hysteretic effect that takes place in the Fraser River [*McLean et al.,* 1999]. Figure 4.13 shows the daily average time-series of the IM dual-variable inversion for D_g, and *M*. Because there is no 2012 data over the rising limb of the freshet and the 2013 freshet is missing because the 1200 kHz ADCP was out of the water, I choose the 2014 freshet and low flow period to examine the hysteresis.

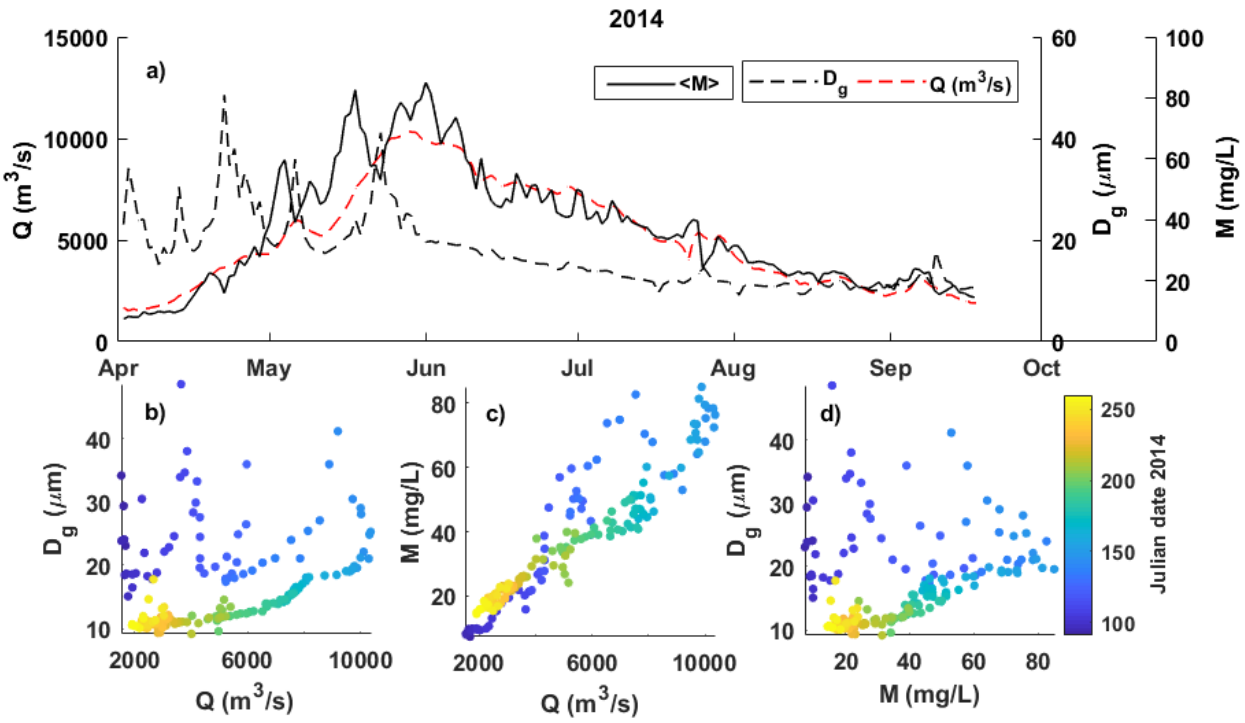

Figure 4.13. IM dual-variable method showing the daily-average a) time-series, b) discharge-D_g relation, c) discharge-M relation, and d) M-D_g relation. Note that <M> is the spatial average for all three frequencies.

The time-series shows how two peaks in *M* occur, one prior to peak discharge (the 'first flush' event) and one at peak discharge, which is a reasonable result. The time-series of D_g shows a peak prior to peak discharge and coarser material at low flow. This is also seen in the relation between Q-D_g (Figure 4.13b) and Q-*M* (Figure 4.13c), where clockwise hysteresis is apparent. Furthermore, a clockwise hysteresis can be seen, to a lesser degree, between D_g-*M*. The ability of the acoustic inversion to capture the hysteresis and therefore *M* and D_g fluctuations independent of discharge is a clear advantage of acoustic methods and demonstrates the robustness of the inversion method when successful.

4.7. Discussion

4.7.1. Known sources of uncertainty in acoustic inversions

There are two known sources of uncertainty in the inversions that include variability in the calibration constant β and increased noise with respect to distance from the transducer.

Uncertainty caused by the calibration constant β

In single frequency inversions (Equation 4.2) the β parameter is included in the source level (*SL*). In multi-frequency inversions, this value is necessary (particularly for implicit methods), and must be estimated directly. For custom-built acoustic instruments, its value can be measured using known targets in the acoustic beam. This is logistically challenging in field applications using off-the-shelf ADCPs, which have larger ranges (10's of meters) and ensonified volumes on the order of cubic meters. So, I have estimated its value using Equation 4.13.

The true value of β is constant for a given instrument. Our results show variability in β calculated using Equation 4.13, but no apparent bias with respect to the mean, so I chose to use the mean value of β in our inversions. An inverse relation exists between β and the initial estimate of *M* such that if β is smaller than the mean value used it would likely increase *M* and vice versa, which would increase errors in *M* that translate into error in estimates in D_g. This occurs because β sets this initial acoustically derived *M*. In the process of finding the final *M* via the minimization of *CV* for all three frequencies, the difference between the initial estimate of *M* and its final value is accounted for by changing sediment attenuation and backscattering form function, which are a function of D_g. Any increase in attenuation or backscattering form function could induce either larger or smaller estimates of D_g. Given that our measured mean D_g (~31 um) falls between the viscous and scattering regions [*Chapter 2*; Figure 2.1], any increase in sediment attenuation would likely increase particle size (Figure 4.5b).

An alternative method for calculating β is to use a well constrained, measured *M* and D_g from a large sediment sample (Figure 4.5). I calculate *M* from Equation 4.4 for a range of β values, then fit non-linear regressions to them and select a value of β where it intersects with the measured *M* and D_g from our LS GSD from June 19, 2014. This

alternative method shows that β is 32 to 74% less than the mean which translates to a ~32% decrease in D_g. It is difficult to assess whether this is a better estimate of β than the mean because it is based on one sample. Nevertheless, if β is indeed overestimated, it could explain the underestimation of particle size using the IM method (Figure 4.8). This suggests that I need a better method for defining β than either the mean from LISST samples or a large GSD. Using a known target appears to be a necessity to improve estimates of M and D_g.

Uncertainty caused by increased noise with respect to distance from the transducer

There are other sources of variability in acoustically derived M (Eq. 4.4) that may stem from noise in the signal. *Hurther et al.* [2011] showed that error in M propagates along the acoustic beam when M> 1kg/m^3, D_{50}>200μm and instrument frequencies are >2 MHz. I do not have these conditions, but I do see variability of the signal along the beam. *Chapter 2* found variability in the shape of the acoustic profile towards the end of the profile due to acoustic noise, as the signal approached the noise floor. Signal variability occurred at low concentration and at high concentration when the signal was strongly attenuated.

I can evaluate the effect of conditions on profiles by examining CV (Eq. 4.7) from both inversion methods as a function of range and measured M. For both methods, I see substantial variance in the predicted CV(M) at the end of the profile, with the EX method showing slightly more elevated CV values at lower concentrations (Figure 4.14). The increase in CV occurs in all M conditions at the end of the profile range and is larger at low M conditions. This is likely due to an increase in noise in the 1200 kHz ADCP as it approaches or reaches the noise floor at the end of the profile [*Chapter 2*].

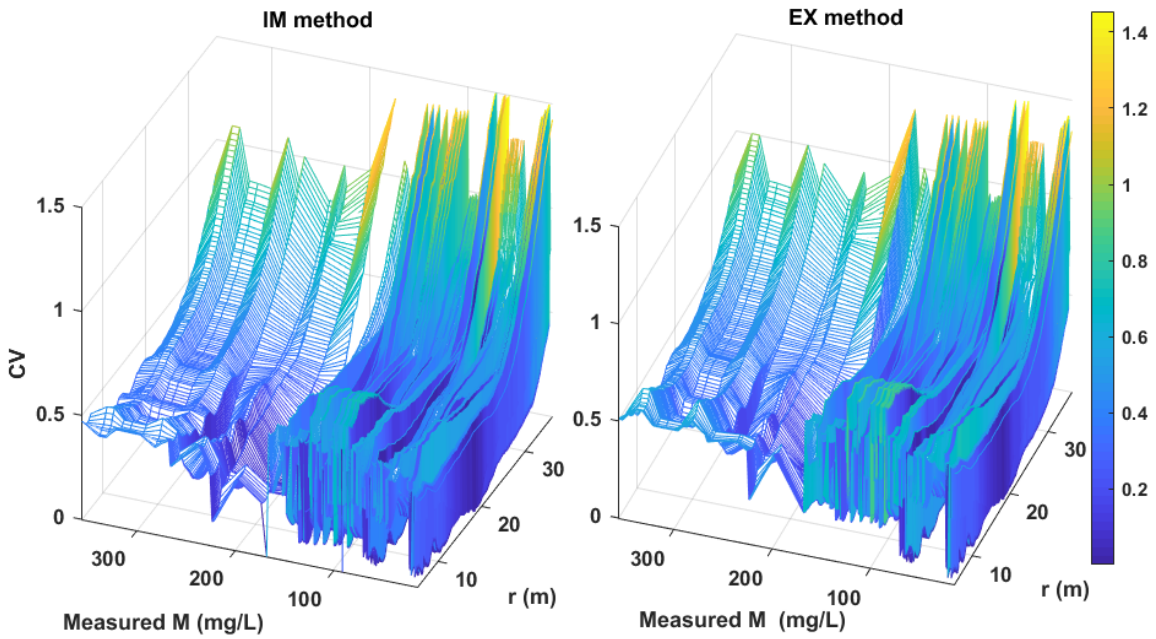

Figure 4.14. Coefficient of variation (CV) for each measurement profile as a function of distance from the transducer and M using a) the IM method and b) the EX method.

How the increased noise influences the acoustic inversion methods needs to be examined and can be tested by truncating the profiles prior to the noise floor. I use the methods presented in *Chapter 2* to truncate the profiles at the noise floor for 1200 kHz ADCP and filter the results of the IM and EX methods. Applying the truncation to *M* and D_g, I see D_g results for the EX method move closer to the line of unity (Figure 4.15a), while frequency average *M* values move away from the line of unity (Figure 4.15b). Using the IM method, results do not change substantially (Figure 4.15 c and d). Application of the noise floor filter from *Chapter 2* to both the IM and EX methods suggests that the IM method tends to be less sensitive to the noise floor than the EX method. Additionally, application of the filter does not improve results substantially.

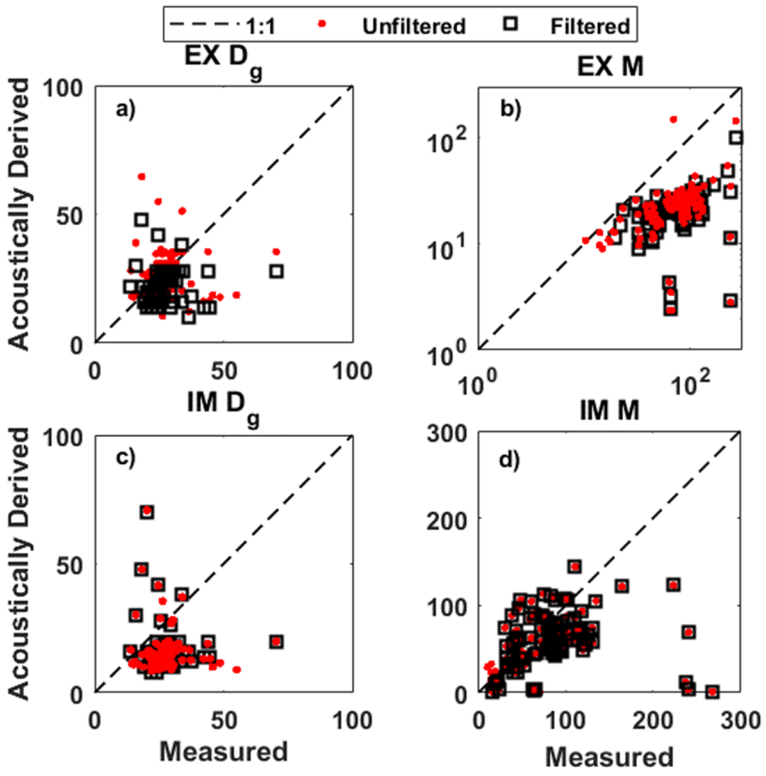

Figure 4.15. Observed concentrations compared to acoustically derived frequency averaged concentrations and particle size for both the filtered and unfiltered results (i.e. Figure 4.8). The dual-variable method was used.

4.7.2. How well can we resolve the standard deviation of the GSD using a sensitivity analysis

Previous applications of implicit or explicit inversions have determined concentration and particle size, without estimation of GSD standard deviation. *Thosteson and Hanes* [1998] indicated that the standard deviation of the GSD could be calculated using three or more frequencies, but did not apply the method because it is generally not necessary in environments where the width of the GSD does not vary substantially. In many rivers, including the Fraser, grain size and the shape of the GSD varies depending on sediment sources. I have developed a method for calculating σ_g using three frequencies and a sensitivity analysis that minimizes CV of *M* amongst all frequencies (Equation 4.7). The sensitivity analysis holds the determined *M* and D_g for the 300 and 1200 kHz instruments constant and recalculates *M* from the 600 kHz frequency over a range of σ_g to further minimize CV.

In the tri-variable inversion, I recalculate *M* for all three frequencies using the estimated σ_g to see how it influences *M* for the 1200 and 300 kHz. I find, using the IM method, that it increases the scatter relative to the dual-variable results. The 600 kHz *M* is about the same, suggesting that σ_g is a function of frequency. This makes sense because the sensitive portion of the theoretical attenuation and backscatter form function curves are frequency dependent [*Flammer*, 1963; *Moore et. al*, 2013; *Chapter One*]. This leads to the acoustic instruments 'seeing' different concentrations, resulting in the poorer estimates of *M* with an estimate of σ_g for the 1200 and 300 kHz frequencies. Therefore, any improvement of *M* using the tri-variable method would need to come from frequency dependent estimates of σ_g. For the EX method, application of the sensitivity analysis does not change the σ_g substantially from its initial estimate through the iterations (Figure 4.10d). As a result, the EX method produces acoustically derived σ_g values that appear unreasonable because there is no obvious variation, despite variation in measured σ_g (Figure 4.10).

Adding another frequency ADCP to the three frequency array could be a more robust method than the sensitivity analysis for improving acoustically derived *M* because with a fourth frequency, the third variable σ_g could be found by minimization for each frequency. For our setup, the addition of another ADCP would be impractical and expensive. However, an off-the-shelf ADCP with multiple frequency capabilities, similar to custom built lab scale instruments, could improve the practicality of acoustically derived sediment properties from ADCPs.

Nevertheless, the estimate using the IM method is reasonable and works well for one frequency, in our case the 600 kHz frequency. I examined how well the 600 kHz σ_g predict acoustically derived GSDs, averaged over all samples (Figure 4.16). The IM method gives an acoustic GSD that is relatively finer and more broad than the EX method and resembles that of the large LS GSD. The EX acoustic GSD resembles the average bottle sample GSD from the LISST, while also showing a secondary, coarse mode. This suggests that our sensitivity analysis method is effective to estimate σ_g.

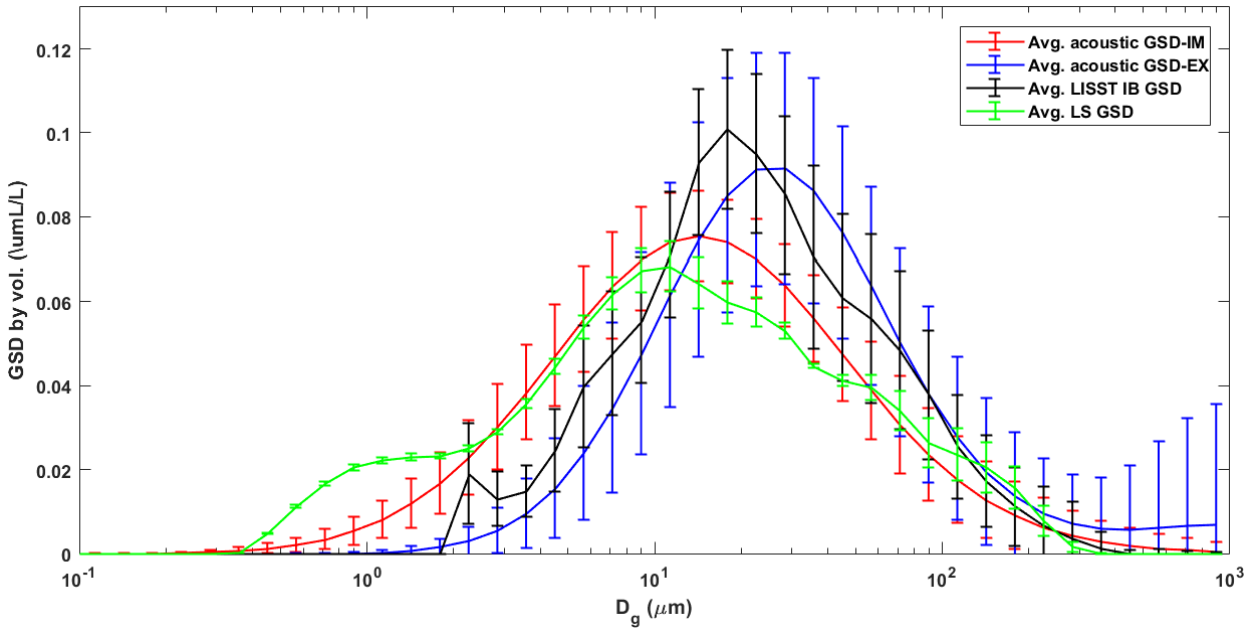

Figure 4.16. Average acoustically derived GSD in for both the IM and EX methods compared to the average GSD from the LISST and the LS.

4.7.3. Recommendations for implementation

In rivers such as the Fraser River where concentrations are low (10-500 mg/L), the capability to estimate *M* and D_g at both low and high (freshet) flows is important. Generally, the dual-variable inversion using either the implicit or explicit methods closely approximates measured *M* during freshet flows. However, the IM method outperforms the EX method at low flows with respect to acoustically derived *M*. Though the IM method gives the best *M* values throughout all three years examined, the average amongst frequencies slightly underestimates the measured *M* samples. Still, given the robust estimates at all flow conditions, it is the most appropriate method to use.

Both the IM and the EX methods give reasonable results for D_g using the dual-variable inversion when flow velocities are above 0.3 m/s (Figures 4.11 and 4.12). The IM method tends to give D_g values that are less than the LISST measured D_g, while the EX method determines D_g that resemble LISST measured D_g well. However, the measured GSD from the LISST, against which I compare our predicted D_g, may not completely capture the fine tail of the GSDs [*Chapter 2*]. So, a well resolved comparison is difficult to make. Nevertheless, using a constant D_g in the single-variable inversions produces poorer estimates of *M* compared to the dual-variable inversions. This result

further demonstrates that the dual-variable IM method is likely the most accurate when estimating *M* using multifrequency acoustic inversions in conditions similar to those of the Fraser River.

4.8. Conclusion

I explored a series of acoustic inversion tests (single-, dual-, and tri-variable) using the implicit (IM) method of *Thorne and Hurther* [2014] and explicit (EX) method of *Thosteson and Hanes* [1998], which are two common approaches to acoustically derive *M*, D_g, and possibly σ_g. Three off-the-shelf ADCPs with different frequencies (300, 600 and 1200 kHz) were deployed for a three-year period and samples were collected within the ensonified volume at high spatiotemporal resolution. I examined the influence of the variables *M*, D_g, and σ_g, along with the measured GSDs, on the acoustic inversion process. Our results show that:

1. *M* values are well predicted when using both dual-variable inversion methods, but the implicit method better predicts *M* in all flow conditions.

2. Both the IM and EX methods gave reasonable values for D_g at high flows, while at low flow incoherent noise dominated the signal. The EX method aligns well with measured D_g, while the IM method tends to underestimate D_g values. However, this may be due to limitations of the instrument used to measure the GSDs.

3. Our sensitivity analysis used to determine σ_g shows reasonable values using the IM method, but the estimate does not improve *M* estimates for all three frequencies. Acoustically derived σ_g values tend to be frequency dependent and a more robust method is required to estimate σ_g., such as an additional frequency.

4. A more robust method to determine the calibration parameter β is needed to improve inversion method.

5. The dual-variable IM method provides the most robust results for low concentration environments such as the Fraser River.

Our systematic evaluation of multifrequency inversions in a large river using off the shelf instruments shows that the essential elements of the annual sedigraph can be captured at high spatial and temporal resolution. Hysteretic relations between discharge and sediment properties-- including mass concentration and grain size—provide more detail than typical physical sampling campaigns. With further refinement, this could produce a method to substantially reduce the costs associated with physical sediment sampling campaigns and provide much greater resolution of suspended sediment transport.

4.9. Appendix

Appendix 4.1. Acoustic calibration and conversion from backscatter in counts to backscatter pressure

The acoustic calibration that is required to convert backscatter in counts (*EI*), as it is received from the ADCP, to decibels relies on two approaches. First, one must accurately define the noise level, *NL*, which is a function of ambient and instrument sources [*Chapter 2*]. Second, when the acoustic profile approaches *NL* a piecewise function is needed to extend the profiles usable data while preventing artificial profile features. I_{dB} used in this work is taken from *Chapter 2* following the results. To convert *EI* to I_{dB}, they used:

$$I_{dB} = \begin{cases} kc(EI - NL), & EI > 10 * NL \\ 10log_{10}(10^{\frac{k_c EI}{10}} - 10^{\frac{k_c NL}{10}}), & EI \leq 10 * NL \end{cases} \quad \text{(A4.1)}$$

where k_c=127.3/Te+273, which is given by the manufacturer [*Teledyne RDI Instruments*, 2008] and varies between 0.41-0.46. The conversion from decibels to root-mean squared pressure, P_{rms}, is given by:

$$\frac{P_{rms}^2}{P_{ref}^2} = 10^{\frac{I_{db}}{10}} \quad \text{(A4.2)}$$

where the reference pressure, P^2_{ref}, is 1 μPa and I_{db} is in decibels. The procedure used here is described in more detail in *Chapter 2*.

Appendix 4.2. Backscattering form function

To compute k_s I use:

$$k_s^2 = \frac{f^2}{\int an(a)da} \tag{A4.3}$$

where *a* is the particle radius, *f* is the ensemble form function, where "ensemble" means it is integrated over the grain size distribution by number, *n(a)*.

The ensemble averaged form function can be computed as:

$$f = \left[\frac{\int_0^\infty an(a)da \int_0^\infty \left(\frac{f_i}{\rho_s}\right)^2 a^2 n(a)da}{\int_0^\infty a^3 n(a)da} \right]^{1/2} \tag{A4.4}$$

where ρ_s is the sediment density and f_i is the intrinsic form function (where intrinsic represents an acoustic response to a mean grain radius), which can be computed from the empirical model [*Thorne and Hurther*, 2014]:

$$\frac{f_i(x)}{\rho_s} = \frac{x^2(1 - 0.25e^{-\left(\frac{x-1.5}{0.35}\right)^2})(1 + 0.6e^{-(\frac{x-2.9}{1.15})^2})}{42 + 25x^2} \tag{A4.5}$$

where $x=ka$. For this work ρ_s is assumed to be 2650 kg/m^3.

Appendix 4.3 Sediment attenuation coefficients

Total sediment attenuation is computed as:

$$\alpha_s = \alpha_{s,visc} + \alpha_{s,scatt} = M\langle\zeta_{visc}\rangle + M\langle\zeta_{scatt}\rangle \tag{A4.6}$$

where $\alpha_{s,visc}$ is the sediment attenuation from viscous losses, $\alpha_{s,scatt}$, is sediment attenuation from particle scattering. ζ_{visc} is the viscous attenuation coefficient and ζ_{scatt} is the scattering attenuation coefficient.

The scattering attenuation coefficient is computed as:

$$\langle \zeta_{scatt} \rangle = \frac{3 \int_0^\infty a^2 \chi n(a) da}{4\rho \int_0^\infty a^3 n(a) da} \quad \text{(A4.7)}$$

where χ is the intrinsic total scattering cross-section, which can be defined by [*Thorne and Meral*, 2008]:

$$\chi = \frac{0.29x^4}{0.95 + 1.28x^2 + 0.25x^4} \quad \text{(A4.8)}$$

The sediment attenuation coefficient from viscous losses can be computed as:

$$\langle \zeta_{visc} \rangle = \frac{\int_0^\infty \zeta_{visc}(a) a^3 n(a) da}{\int_0^\infty a^3 n(a) da} \quad \text{(A4.9)}$$

where,

$$\zeta_{visc} = \frac{k(G-1)^2}{2\rho_s} \left[\frac{s}{s^2 + (G+\delta)^2} \right] \quad \text{(A4.10)}$$

with:

$$s = \frac{9}{4ba} \left[1 + \frac{1}{ba} \right] \quad \text{(A4.11)}$$

and,

$$G = \frac{\rho}{\rho_w};\ \delta = \frac{1}{2} \left[1 + \frac{9}{2ba} \right]; b = \sqrt{\frac{\omega}{2v}} \quad \text{(A4.12)}$$

where ρ_w is fluid density, v is kinematic viscosity of water, and ω is the angular frequency.

Appendix 4.4 Instrument constant and source level

The instrument constant can be defined by:

$$k_t^2 = P_o^2 r_o^2 T_v^2 R^2 \frac{3\tau c}{16} \left(\frac{0.96}{k a_t} \right)^2 \quad \text{(A4.13)}$$

where P_o is the reference pressure at the reference range, r_o=1m, T_v is the voltage transfer function, R is the transducer receive sensitivity, c is the celerity of sound in water, k is the acoustic wavenumber, a_t is the transducer radius, and τ is the pulse duration. For commercially available ADCP systems, known quantities in Equation A4.13 are pulse length, traducer radius, acoustic wavenumber and r_o. For convenience, I define the two parameters T_v and R as $\beta=T_vR$. The reference pressure can be estimated from:

$$\frac{P_o^2}{P_{ref}^2} = 10^{\frac{SL}{10}} \tag{A4.14}$$

where P_{ref} is the reference pressure which is equal to 1 μPa and SL is the source level in decibels and can be defined by *Urick* [1975] as:

$$SL = 170 + 10\log(Wa) + 10\log((\frac{2\pi a_t}{\gamma})^2) \tag{A4.15}$$

where Wa is the transmission power in Watts (provided by the manufacturer Teledyne RDI) and γ is the acoustic wavelength. Transmission power is a function of the power source and can fluctuate. Our setup had land power, an AC/DC converter, and utilized a voltage regulator, thus we assumed it was close to the constant value recommended by the manufacturer (Teledyne RDI). The first two terms represent the source power while the second describes the directivity of the system. Using Equations A4.13 and A4.14 with the quantities retained by the ADCP, the only unknowns are T_v and R, which can be estimated by methods described in *Betteridge et. al.* [2008].

Chapter 5. Conclusion

5.1. Synthesis of the thesis

Suspended sediment fluxes in rivers has traditionally been determined by direct bottle sampling of water-sediment mixtures, filtration of the solid fraction and subsequent analysis of the sediment for grain size. Sediment sampling is labor intensive and expensive, but perhaps more importantly, it provides limited spatial and temporal resolution. Sediment rating curves for approximating suspended sediment flux from water discharge have been widely used by river managers and scientists. However, sediment rating curves experience drift and instability due to changes in sediment supply and grain-size within a drainage basin. The use of hydroacoustics as a surrogate measurement of suspended sediment has the potential to circumvent the problems associated with rating curves and provide data at unprecedented spatial and temporal scales because both suspended sediment concentration and grain size may be predicted from acoustic backscatter and attenuation properties.

The development of Acoustic Doppler Current Profilers (ADCP) for measuring water velocity has permitted the detection of suspended sediment with very high temporal resolution and, potentially, high spatial resolution. However, the theory that underlies the application of acoustic transducers to measure suspended sediment cannot be straightforwardly applied to 'off-the-shelf' ADCPs used in discharge monitoring because there are a host of instrument constants and response characteristics that are unknown for these instruments. The methods used to convert characteristics of ADCP signals to suspended sediment concentrations and grain size remains an active area of research.

In this dissertation, I have taken a systematic approach to testing methods for inverting acoustic backscatter to grain size specific suspended sediment fluxes in the Fraser River at Mission, British Columbia, Canada just upstream of where the river enters the Fraser Delta. The river is much wider than can be penetrated using off-the-shelf ADCPs. The river carries relatively low concentrations (<500 mg/L) of a mixture of fine sand, sourced from the bed material and silt/clay delivered annually during the annual freshet. The mean grain size of suspended sediment falls between the viscous and backscattering attenuation losses for most off-the-shelf ADCP frequencies. The

combination of low sediment concentrations, grain size and ADCP frequencies make application of hydroacoustic methods developed for custom-built transducers challenging.

Chapter Two is an evaluation of processing methods commonly used in acoustic inversions. I examined how two methods of converting echo intensity to acoustic backscatter influence estimates of sediment attenuation. One method takes into account the presence of the acoustic noise floor and the other does not. I undertook bottle sampling within the ensonified volume of the ADCPs, which allowed for estimates of sediment attenuation from the diminishing backscatter across the channel (in-situ attenuation) and theoretical attenuation calculated from the measured grain size distributions. The comparison between sediment attenuation estimation methods allowed for a critical test of the in-situ attenuation calculation method when compared to theoretical attenuation, leading to a better understanding of the conditions in which the in-situ method is applicable.

This is the first direct field comparison between in-situ and theoretical attenuation methods using samples obtained within the ensonified volume of the acoustic beams. Observations reveal that when converting acoustic intensity from counts to decibels, acoustic profiles that approach the noise floor need to be corrected for non-linearity before they are truncated in low concentration environments. The semi-autonomous method described in *Chapter Two* prevents the influence of the noise floor from affecting the acoustic profiles, leading to better estimates of in-situ attenuation. Nevertheless, during very low concentrations in the Fraser River, the in-situ sediment attenuation method is not reliable because gradients in suspended sediment develop across the ensonified volume, creating a non-uniform suspension that is reflected in the acoustic profile. At higher concentrations (>50 mg/L for 1200/600 kHz ADCP and >75 mg/L for the 300 kHz ADCP) the ensonified volume is relatively homogeneous and acoustic profiles do not exhibit cross-channel gradients, so in-situ and theoretical attenuation estimates agree better. The results highlight the need to explore cross-channel changes in suspended sediment concentration and grain size at a range of flows to ensure homogenous suspensions in the ensonified volume. Application of in-situ sediment attenuation methods in routine monitoring programs without doing so can result in order of magnitude errors in sediment attenuation. In-situ attenuation estimates are necessary

when using semi-empirical or empirical inversion approaches to estimate SSC and particle size, especially when utilizing theoretical relations.

Chapter Three examines the feasibility of semi-empirical acoustic inversions to estimate total and fractional channel average suspended sediment concentration (SSC) and flux. A two–stage acoustic inversion, developed by *Venditti et al.* [2016], is refined. In the first stage, ADCP backscatter and attenuation are calibrated to size specific SSC measured in the ensonified volume. In the second stage, ADCP-derived, size-fractionated concentrations are correlated with measured concentrations to obtain channel-average SSC. This index relation allows for calculation of channel-average sediment fluxes, even though the ADCPs have limited penetration (20 to 60 m) into the 550 m wide channel. Fluid-corrected backscatter (FCB) is calibrated to total suspended sediment (TSS) concentration. Sediment-corrected backscatter is calibrated to sand SSC. In-situ attenuation is calibrated to silt-clay SSC.

Strong calibrations exist between TSS, sand SSC and silt/clay SSC for the 600 kHz ADCP, while calibrations for TSS and sand SSC were good for the 1200 and 300 kHz ADCP. Correlations between ADCP-derived concentrations and channel averaged concentrations were good. Overall, the 600 kHz ADCP performed best for monitoring TSS, sand SSC and silt/clay SSC. However, at concentrations above a threshold of 150 mg/L, calibrations between TSS and *FCB* are not reliable because sediment attenuation is not accounted for in *FCB*. Total SSC is best calculated as sum of sand and silt/clay SSC or flux.

Intra- and inter-annual variability in the calibrations was explored. If monitoring programs are to be successful, and reduce the resources necessary to mount traditional bottle sampling monitoring programs, calibrations must be stable. *Chapter Three* shows that there is inter- and intra-annual variability in acoustic calibrations. The limited number of data points available in any one year prevent a definitive conclusion about the stability of the calibrations. However, the variability may suggest that calibrations are site-specific correlations, sensitive to variations in grain-size, concentration and sediment composition. Despite this variability, acoustically-derived annual sediment fluxes are on the same order of magnitude as historical observations of sediment flux at Mission, based on bottle sampling, suggesting that the index relation of the two-stage method cancels out any bias in the calibrations.

Chapter Four attempts to resolve the limitation of the empirical and semi-empirical approaches presented in *Chapter Three*. Multifrequency acoustic inversions applied using custom-built acoustic transducers are capable of estimating SSC, grain size, and with three or more frequencies, the standard deviation of the grain size distribution (GSD). Therefore, the multi-frequency inversions using off-the-shelf ADCP signals may be less sensitive to changes in sediment sources and GSD characteristics than single frequency inversions. Two common approaches that have been extensively evaluated with smaller scale, custom-built, acoustic sensors were evaluated: the implicit and explicit inversions. These methods have not been tested using ADCPs. *Chapter Four* presents a systematic analysis where first mass concentration is calculated, but the sediment size and standard deviation of the GSD is held constant. Then mass concentration and grain size is calculated while the standard deviation of the GSD is held constant. Then all three variables are calculated. The dual-variable method provided the most robust results relative to performance and computational time. Truncating the acoustic profiles based on where signals reach the noise floor *[Chapter Two*] provided slightly more robust results. The implicit method provides the best results when deriving SSC for all flows, while both the explicit and implicit methods perform reasonably well at freshet flows. Similarly, at freshet flows, both methods derived particle size well, but show incoherent noise at low flow periods. The multi-frequency methods captured hysteric relations known to exist between discharge, mass concentration, and grain size. The multifrequency inversions provide a method to increase spatial and temporal resolution of acoustically-derived sediment properties, relative to that of physical sampling.

5.2. Recommendations for a sediment monitoring program

Two different types of acoustic inversions are presented to estimate SSC and GSD characteristics; single frequency and multi-frequency inversions. If a sediment monitoring program is to be set forth for the Fraser River at Mission, determining which method is most appropriate is necessary. The 600 kHz frequency ADCP provides the most robust single frequency inversion results while the implicit multi-frequency inversion performs best. Comparison of how well single frequency inversions perform relative to multi-frequency inversions can only be done by examining comparable criteria, which has not yet been done. However, limitations of each method do emerge in the

dissertation. The single frequency inversions presented in *Chapter Three* were only useful for estimating SSC during freshet flow. The multifrequency implicit method predicted SSC well under all flow conditions. At low flow conditions, both single- and multi-frequency inversions performed relatively poorly when estimating of size-specific SSC or particle size, respectfully.

A substantial difference between the single- and multi-frequency inversions is computing time. The single frequency method requires substantially less processing time compared to the multifrequency methods. The spatial resolution of the SSC and GSD estimates is also an important difference between methods. The 600 kHz frequency has a greater range, yet the resolution of the data was spatially averaged using a single-frequency, though it does not have to be. With this said, any information of fractional grain size derived from in-situ attenuation using a semi-empirical relation will be a spatial average. The multifrequency inversion provides more spatial resolution of SSC and grain size characteristics.

For a sediment monitoring program, the multifrequency inversion has the most potential to provide high resolution estimates of concentration and grain size. However, further research is required to more explicitly compare the predicted concentration and grain size to observations and to implement a well-resolved index relation-- as is done in *Chapter Three*. The shortcomings that were described in *Chapter Four* using the multifrequency inversion may be partially ameliorated using more robust sediment attenuation and scattering models. For immediate implementation, the single-frequency, semi-empirical approach may be warranted, but calibrations and index correlations should be maintained to ensure the variability observed does not affect the total sediment fluxes. Additionally, the calibration and channel-extension relation need to be validated and should be the next step to establishing a monitoring program.

5.3. Future work

In *Chapter Two* I compared in-situ attenuation to theoretical attenuation. The theoretical attenuation used was computed from theoretical models based on sampled GSDs. Measured grain size distributions were limited to 2 to 356 microns. Analysis of two exceptionally large samples obtained at the site, using an instrument with a larger range (0.4 to 1000 microns) but requiring more sediment, suggested that the measured

GSDs may have been truncated. In order to better characterise theoretical attenuation, an instrument capable of measuring a wider grain size distribution using small samples is needed. Better resolved GSDs would also permit development of more refined sediment attenuation models. *Moate and Thorne* [2013] have developed scattering models that can account for mixed sediment compositions, like those that occur in the Fraser River at Mission. Utilizing these mixed sediment models for attenuation would further our ability to invert acoustic signals to SSC and GSD characteristics, particularly when using multifrequency inversions.

In *Chapter Four* I show that though the implicit method performs well at all flow conditions when estimating SSC, during the first flush event in late April 2014 where concentrations reached 350 mg/L, SSC was underestimated. This was likely due to changes in sediment composition relative to the sand models used in the inversion. Applying advanced attenuation and backscattering form function models that can account for mixed sedimentology may better account for changes that occur during the first flush. Additionally, applying models that account for changes in particle shape, which has been shown to be influential [*Moore et al.*, 2013; *Richards*, 2003], would also provide acoustic inversions that may better estimate SSC and GSD characteristics.

In *Chapter Four*, I used a sensitivity analysis to obtain an estimate of GSD standard deviation. An alternative would be to use a fourth frequency and solve for mass concentration, grain size and GSD standard deviation. While off-the-shelf, dual-frequency ADCPs are currently available, three and four frequency instruments have not been developed. Collocating four different frequency ADCPs seems impractical, but it may provide an initial proof of concept for further for instrument development. Developing an ADCP instrument with a signal range of 10’s to 100’s of meters and four frequencies may prove to be an ideal instrument for monitoring both water and sediment discharge in riverine environments.

References

Agrawal, Y. C., and H.C. Pottsmith (2000), Instruments for particle size and settling velocity observations in sediment transport. Mar. Geol. 168: 89–114.

Attard, M. E., J. G. Venditti, and M. Church, (2014), Suspended sediment transport in the Lower Fraser River, British Columbia, Can. Water Resour. J., 39, 356-371.

Betteridge, K.F.E., P.D., Thorne, and R.D., Cooke, (2008), Calibrating multi-frequency acoustic backscatter systems for studying near-bed suspended sediment transport processes. Cont. Shelf Res., 28, 227–235.

Crawford, A. M. and A. E. Hay, (1993), Determining suspended sand size and concentration from multifrequency acoustic backscatter, J. Acoust. Soc. Am. 94(6), 3312-3324.

Church, M. (2006), Bed material transport and the morphology of alluvial river channels, Annu. Rev. Earth Planet. Sci., 34, 325–354, doi:10.1146/annurev.earth.33.092203.122721.

Church, M. (2007), Review of the lower Fraser River sediment budget: final report. Report to Fraser River Estuary Management Program, 26 July, 2007: 24pp.

Church, M., J.G. Venditti. (2008), Recommendations for the reestablishment of sediment transport observations at Mission City (WSC Station 08MH024): Final Report. Report to Fraser River Estuary Management Program, 28 November, 2008: 8pp + Appendices.

Clay C.S., and J. Medwin, (1977), Acoustical Oceanography: Principles and Applications. John Wiley and Sons, Toronto, p. 82.

Dashtgard, S.E., J.G. Venditti, P.R. Hill, C.F. Sisulak, S.M. Johnson, and A.D. La Croix, (2012), Sedimentation across the tidal-fluvial transition in a tide-influenced, fluvially dominated delta, Fraser River Delta, Canada. The Sedimentary Record, v. 10, p. 3-9.

Deines, K.L., (1999), Backscatter estimation using broadband acoustic Doppler current profilers. In: Proceeding of the IEEE, 6th Working Conference on Current Measurement, San Diego, CA, USA. Topping et. al., 2015;

Flammer, G. H., (1962), Ultrasonic measurement of suspended sediment, U.S. Geol. Surv., Bull. 1141-A. Govt. Printing Office, Washington, DC, 48 pp.

Folk, R.L. and W.C., Ward, (1957), Brazos River bar: a study in the significance of grain size parameters. *Journal of Sedimentary Petrology*, 27, 3-26.

Francois R.E. and G.R. Garrison, (1982), Sound absorption based on ocean measurements: Part I: Pure water and magnesium sulfate contributions. J. Acoust. Soc. Am. 72, 896.

French, J.R., H. Burningham, and T. Benson, (2008), Tidal and meteorological forcing of suspended sediment flux in an muddy mesotidal estuary, *Estuaries and Coasts*, 31, 843-859.

Gartner, J. W., (2004), Estimating suspended solids concentrations from backscatter intensity measured by acoustic Doppler current profiler in San Francisco Bay, California, Marine Geol., 211, 169-187.

Gitto, A. B., J. G. Venditti, R. Kostaschuk, and M. Church, (2017), Representative point-integrated suspended sediment sampling in rivers, Water Resour. Res., 53, doi:10.1002/2016WR019187.

Gostiaux L. and H. van Haren, (2010), Extracting meaningful information from uncalibrated backscattered echo intensity data. Journal of Atmospheric and Oceanic Technology, 27: 943-949.

Gray J.R., and M.N. Landers, (2014), Measuring Suspended Sediment. In: Ahuja S. (ed.) Comprehensive Water Quality and Purification, vol. 1, pp. 157-204. United States of America: Elsevier.

Guerrero, M., Szupiany, R. N. and Latosinski, F. (2013), Multi-frequency acoustics for suspended sediment studies: an application in the Parana River, *J. Hydraul. Res., 51*, 696-707.

Hanes D.M., (2012a), On the possibility of single-frequency acoustic measurement of sand and clay concentrations in uniform suspensions. Cont. Shelf Res., 46, 64-66.

Hanes, D. M. (2012b), On the possibility of single-frequency acoustic measurement of sand and clay concentrations in uniform suspensions. *Cont. Shelf Res. 46*, 64-66. Erratum, v. *54* (2013), 117-118.

Hay, A.E., (1983). On the remote acoustic detection of suspended sediment at long wavelengths, *J. Geophys. Res.* 88, 7525-7542.

Hay, A. E. (1991), Sound scattering from a particle-laden, turbulent jet, J. Acoust. Soc. Am. 90, 2055-2074.

Hay, A. E. and J. Sheng, (1992), Vertical profiles of suspended sand concentration and size from multifrequency acoustic backscatter. J. Geophys. Res., 97, 15,661-15,677.

Haught, D. J. G. Venditti and M. Church, (2014), Acoustic sediment flux observations on the Fraser River, Canada, In: River Flow 2014 (Ed. A.J. Schleiss, G. de Cesare, M.J. Franca and M. Pfister), pp 1943-1950, CRC Press, London, UK.

Hoitink, A. J. F. and P. Hoekstra, (2005), Observations of suspended sediment from ADCP and OBS measurements in a mud-dominated environment, Coastal Eng., 52, 103-118.

Hurther, D., P.D., Thorne, M., Bricault, U., Lemmin, and J.M, Baroud, (2011), A multi-frequency acoustic concentration and velocity profiler (ACVP) for boundary layer measurements of fine-scale flow and sediment transport processes. *Coastal Eng.,* 58, 294–605. (doi:10.1016/j.coastaleng.2011.01.006).

Kleinhans, M.G., A.W.E, Wilbers, and W.B.M., ten Brinke, (2007), Opposite hysteresis of sand and gravel transport upstream and downstream of a bifurcation during a flood in the Rhine River, the Netherlands: *Netherlands Journal of Geosciences*, 86, 3, p. 273–285.

Landers, M. N., (2012), Fluvial suspended sediment characteristics by high resolution, surrogate metrics of turbidity, laser-diffraction, acoustic backscatter, and acoustic attenuation. Ph.D. Dissertation, Georgia Institute of Technology.

Landers, M. N., and T. W. Sturm (2013), Hysteresis in suspended sediment to turbidity relations due to changing particle size distributions, *Water Resour. Res.,* 49, 5487–5500, doi:10.1002/wrcr.20394.

Latosinski, F.G., R.N. Szupiany, C.M. Garcia, M. Guerrero, and M.L. Amsler, (2014), Estimation of concentration and load of suspended bed sediment in a large river by means of acoustic Doppler technology, *J. Hydraul. Eng.*, 140, 7.

Lee, T.H., and D.M. Hanes, (1995), Comparison of field observations of the vertical distribution of suspended sand and its prediction by models, J. Geophys. Res., 101, 3561-3572.

Levesque, V.A. and K.A. Oberg, (2012), Computing discharge using the index-velocity method. U.S. Geological Survey techniques and methods 3-A23.

Libicki, C., K.W. Bedford, and J.F. Lynch, (1989), The interpretation and evaluation of a 3-MHz acoustic backscatter device for measuring benthic boundary layer sediment dynamics. J. Acoust. Soc. Am. 85, 1501–1511.

Northwest Hydraulic Consultants (NHC). 2002. Review of lower Fraser River sediment budget: final report. Report prepared for the Dredge Management Advisory committee, Fraser River Estuary Management Program. 42pp + appendix.

MacDonald, I. T., C. E., Vincent, P. D. Thorne, and B. D., Moate, (2013), Acoustic scattering from a suspension of flocculated sediments, *J. Geophys. Res. Oceans*, 118, 2581-2594.

Mark, D.M., M. Church. 1977. On the Misuse of Regression in Earth Science. Mathematical Geology, 9 (1):63-75.

McLean, D.G., and M. Church, (1986), A Re-examination of sediment transport observations in the lower Fraser River. Environment Canada, Inland Waters Directorate, *Water Survey of Canada Report*: 52pp.

McLean, D. G., M. Church, and B. Tassone, (1999), Sediment transport along lower Fraser River. 1. Measurements and hydraulic computations. Water Resour. Res. 35, 2533-2548.

Moate, B. D., and P. D. Thorne, (2009), Measurements and inversion of acoustic scattering from suspensions having broad size distributions, J. Acoust. Soc. Am. 126, 2905–2917.

Moate, B.D., P.D., Thorne, (2011), Interpreting acoustic backscatter from suspended sediments of different and mixed mineralogical composition. *Cont. Shelf Res.*, 46, 67–82.

Moate, B. D., and P. D. Thorne, (2013), Scattering from suspended sediments having different and mixed mineralogical compositions: Comparison of laboratory measurements and theoretical predictions, J. Acoust. Soc. Am. 133, 1320-1334.

Moore, S.A., J. LeCoz, D. Hurther, and A. Paquier, (2012), On the application of horizontal ADCPs to suspended sediment transport surveys in rivers, Cont. Shelf Res., 46, 50-63.

Moore, S.A., J. LeCoz, D. Hurther, and A. Paquier, (2013), Using multi-frequency acoustic attenuation to monitor grain size and concentration of suspended sediment in rivers, J. Acoust. Soc. Am. 133, 1959-1970. Richards, S.D., T.G. Leighton, and N.R. Brown, (2003), Visco-inertial absorption in dilute suspensions of irregular particles. Proceedings of the Royal Society of London 459, 2153-2167.

Plaut G. and R. Vautard, (1993), Spells of low-frequency oscillations and weather regimes in the Northern Hemisphere. *Journal of Atmospheric Sciences*, 52, 2, 210-236.

Reichel, G. and Nachtnebel, H. P. (1994) Suspended sediment monitoring in a fluvial environment: advantages and limitations applying an acoustic Doppler current profiler. *Water Res., 28*, 751-761.

Richards, S.D., T.G., Leighton, and N.R., Brown, (2003), Visco-inertial absorption in dilute suspensions of irregular particles, *Proceedings of the Royal Society of London* 459, 2153-2167.

Ruhl, C.A. and M., Simpson, 2005, Computation of discharge using the index-velocity method in tidally affected areas. U.S. Geological Survey scientific investigations report 2005-5004.

Sassi, M. G., Hoitink, A. J. F. and Vermeulen, B. (2012) Impact of sound attenuation by suspended sediment on ADCP backscatter calibrations, *Water Resour. Res., 48*, W09520, doi:10.1029/2012WR012008.

Sassi, M. G., Hoitink, A. J. F., Vermeulen, B. and Hidayat, H. (2013), Sediment discharge division at two tidally influenced river bifurcations. *Water Resour. Res., 49*, 2119-2134.

Schaafsma, A.S., and A.E., Hay, (1997), Attenuation in suspensions of irregularly shaped sediment particles: a two-parameter equivalent spherical scatterer model. *J. Acoust. Soc .Am.,* 102, 3, 1485–1502.

Schoellhamer, D.H., (2001), Singular spectrum analysis for time series with missing data. *Geophysical Research Letters* 28: 3187–3190. doi:10.1029/2000GL012698.

Sheng, J., and A.E., Hay, (1988), An examination of the spherical scatterer approximation in aqueous suspensions of sand, *J. Acoust. Soc. Am.* 83, 2, 598-610.

Taylor, J.R., (1997), Introduction to error analysis: the study of uncertainties in physical measurements, 2nd ed., University Science Books, Sausalito, CA, USA.

Teledyne RDI, (2008), Win River II User's Guide, Teledyne RDI Instruments Inc., Poway, CA, USA.

Teledyne RDI, (2011), Acoustic Doppler Current Profiler, Principles of Operation: A Practical Primer, Teledyne RDI Instruments Inc., Poway, CA, USA.

Thevenot, M. M. and Kraus, N. C. (1993), Comparison of acoustical and optical measurements of suspended material in the Chesapeake Estuary. *J. Marine Env. Eng., 1*, 65– 79.

Thorne, P. D. and M. J. Buckingham, (2004), Measurements of scattering by suspensions of irregularly shaped sand particles and comparison with a single parameter modified sphere model, J. Acoust. Soc. Am. 116, 2876-2889.

Thorne, P. D., and S. C., Campbell, (1992), Backscattering by a suspension of spheres. *J. Acoust. Soc. Am.* 92, 978–986.

Thorne, P. D. and D. M. Hanes, (2002), A review of acoustic measurements of small-scale sediment processes, Cont. Shelf Res., 22, 603-632.

Thorne, P. D. and P. J. Hardcastle, (1997), Acoustic measurement of suspended sediments in turbulent currents and comparison with in-situ samples, J. Acoust. Soc. Am., 101, 2603-2614.

Thorne, P. D. and D. Hurther, (2014), An overview on the use of backscattered sound for measuring suspended particle size and concentration profiles in non-cohesive inorganic sediment transport studies. Cont. Shelf Res., 73, 97-118.

Thorne, P.D. and R. Meral, (2008), Formulations for the scattering properties of suspended sandy sediments for use in the application of acoustics to sediment transport processes. Cont. Shelf Res., 28, 309-317.

Thorne, P.D., C.E. Vincent, P.J. Harcastle, S. Rehman, N. Pearson, (1991), Measuring suspended sediment concentrations using acoustic backscatter devices. Marine Geology 98. Elsevier, Amsterdam, pp. 7 – 16.

Thorne, P. D., P. J. Hardcastle, and R. L. Soulsby, (1993), Analysis of acoustic measurements of suspended sediments. J. Geophys. Res., 98, 899-910.

Thorne, P.D., Hardcastle, P.J., Flatt, D., Humphery, J.D., (1994), On the use of acoustics for measuring shallow water suspended sediment processes. *IEEE J. Oceanic Eng.* 19, 1, 48–57.

Thorne, P. D., Y. C., Agrawal, D.A., Cacchione, (2007), A comparison of near-bed acoustic backscatter and laser diffraction measurements of suspended sediments*. IEEE J. Ocean Eng.* 32, 1, 225–235.

Thorne, P.D., D., Hurther, and B.D., Moate, (2011), Acoustic inversions for measuring boundary layer suspended sediment processes. *J. Acoust. Soc .Am.* 130, 3, 1188–1200, http://dx.doi.org/10.1121/1.3618728.

Thorne, P.D., K.R., Waters, and T.J., Brudner, (1995a), Acoustic measurements of scattering by objects of irregular shape. *J. Acoust. Soc. Am.,* 97, 1, 242–251.

Thosteson, E. D. and Hanes, D. M. (1998), A simplified method for determining sediment size and concentration from multiple frequency acoustic backscatter measurements, *J. Acoust. Soc. Am. 104*, 820-830.

Topping, D.J., and S.A. Wright, (2016), Long-term continuous acoustical suspended-sediment measurements in rivers—Theory, application, bias, and error: U.S. Geological Survey Professional Paper 1823, 98 p., http://dx.doi.org/10.3133/pp1823.

Topping, D.J., D.M., Rubin, J.M., Nelson, P.J., III, Kinzel, and I.C., Corson, (2000b), Colorado River sediment transport 2—Systematic bed-elevation and grain-size effects of sand supply limitation: *Water Resour. Res.*, 36, 2, p. 543–570, doi:10.1029/1999WR900286.

Topping, D.J., D.M., Rubin, and Jr., L.E., Vierra, (2000a), Colorado River sediment transport 1—Natural sediment supply limitation and the influence of Glen Canyon Dam: *Water Resour. Res.*, 36, 2, p. 515–542, doi:10.1029/1999WR900285.

Topping, D. J., S. A. Wright, T. S. Melis, and D. M. Rubin, (2007), High-resolution measurements of suspended-sediment concentration and grain size in the Colorado River in Grand Canyon using a multi-frequency acoustic system, in Proceedings of the 10th International Symposium on River Sedimentation. August 1–4, Moscow, Russia, vol. III, 330-339.

Topping, D.J., S.A. Wright, R.E. Griffiths, and D.J. Dean, (2015), Physically based method for measuring suspended-sediment concentration and grain size using multi-frequency arrays of single-frequency Acoustic-Doppler profilers, in Proceedings of the Third Joint Federal Interagency Conference on Sedimentation and Hydraulic Modeling. April 19-23, Reno, NV, p 834-846.

Urick, R.J., (1948), The absorption of sound in suspensions of irregular particles. J. Acoust. Soc. Am, 20(3), pp. 283-289, doi: 10.1121/1.1906373.

Urick, R.J., (1975), Principles of Underwater Sound for Engineers, New York: McGraw Hill, 384 pp.

Vautard, R. and M. Ghil, (1989), Singular spectrum analysis in nonlinear dynamics with applications to paleoclimatic time series, *Physica* D, 35, 395-424.

Vautard, R., P. Yiou, and M. Ghil, (1992), Singular-spectrum analysis: A toolkit for short, noisy, chaotic signals, *Physica* D, 58, 95-126.

Venditti, J. G., and M. Church (2014), Morphology and controls on the position of a gravel-sand transition: Fraser River, British Columbia, J. Geophys. Res. Earth Surf., 119,1959–1976, doi:10.1002/2014JF003147.

Venditti, J. G., N. Domarad, M. Church, and C. D. Rennie (2015), The gravel-sand transition: Sediment dynamics in a diffuse extension, *J. Geophys. Res. Earth Surf.*, 120, doi:10.1002/2014JF003328.

Venditti, J. G., M. Church, M. E. Attard, and D. Haught, (2016), Use of ADCPs for suspended sediment transport monitoring: An empirical approach, Water Resour. Res., 52, doi:10.1002/ 2015WR017348.

Wall, G. R., Nystrom, E. A. and Litten, S. (2006), Use of an ADCP to compute suspended sediment discharge in the tidal Hudson River, New York, *U. S. Geol. Surv., Sci. Inv. Rpt 2006-5055*, 16p.

Walling, D. E., (1977), Limitations of the rating curve technique for estimating suspended sediment loads with particular reference to British rivers, In Erosion and solid matter transport in inland waters: Proceedings of the Paris symposium, Int. Assoc. Hydrol. Sci., Publication 122, 34-48.

Warrick, J.A., M.A. Madej, M.A. Goni, and R.A. Wheatcroft, (2013), Trends in the suspended-sediment yields of coastal rivers of northern California, 1955–2010, *Journal of Hydrology*, 489, 108-123.

Waters, K. A., and J. C. Curran (2015), Linking bed morphology changes of two sediment mixtures to sediment transport predictions in unsteady flows, *Water Resour. Res.,* 51, 2724–2741, doi:10.1002/2014WR016083.

Wilson, G.W. and A.E. Hay, (2015), Acoustic backscatter inversion for suspended sediment concentration and size: A new approach using statistical inverse theory, *Cont. Shelf Res.,* 28, 130-139.

Wood, M. S., and G. N. Teasdale, (2013), Use of surrogate technologies to estimate suspended sediment in the Clearwater River, Idaho, and Snake River, Washington, 2008-10. U. S. Geol. Surv., Sci. Inv. Rpt 2013-5052, 30pp.

Wright, S. A., D. T. Topping, and C. A. Williams, (2010), Discriminating silt-and-clay from suspended-sand in rivers using side-looking acoustic profilers, in Proceedings of the 2nd Joint Federal Interagency Sedimentation Conference, June 2010, Las Vegas NV, http://acwi.gov/sos/pubs/2ndJFIC.